

CROSS-SHELF EXCHANGE FLOW OVER THE WEST FLORIDA INNER SHELF

By

SANGDON SO

A DISSERTATION PRESENTED TO THE GRADUATE SCHOOL
OF THE UNIVERSITY OF FLORIDA IN PARTIAL FULFILLMENT
OF THE REQUIREMENTS FOR THE DEGREE OF
DOCTOR OF PHILOSOPHY

UNIVERSITY OF FLORIDA

2013

© 2013 Sangdon So

To my parents

ACKNOWLEDGEMENTS

First and foremost I would like to thank my advisor, Dr. Arnaldo Valle-Levinson for his generosity, support and guidance. He has given me the freedom to independently explore problems and he has been a conscientious editor who substantially improved this thesis. Special thanks go to my PhD committee, Dr. Louis Motz, Dr. Kirk Hatfield, and Dr. Peter Adams, for their patient feedback and guidance. I deeply appreciate their involvement in this work. The data analyzed in this study we obtained from a series of instrument deployments carried out by Zy Biesinger, whose contribution is gratefully acknowledged.

I owe thanks to Dr. Ashish Mehta for his enthusiastic advice and support. My deepest thanks should go to Ms. Anderson Debra who encouraged me and offered me enthusiastic guidance. Lauren Ross, office-mate and friend, also really helped me improve my writing. She provided careful proofreading and gave valuable comments. I wish to acknowledge the assistance provided by the faculty, staff and students of Civil & Coastal Engineering Department at the University of Florida.

This journey would not have been possible without the emotional and financial support provided by my parents, Junyoung So and Sun An. I would like to thank my wife, Jin; my daughter, Kang; and son, Jungseob for their love and support.

TABLE OF CONTENTS

	<u>Page</u>
ACKNOWLEDGEMENTS	4
LIST OF TABLES.....	7
LIST OF FIGURES.....	8
LIST OF ABBREVIATIONS.....	11
ABSTRACT	12
CHAPTER	
1 INTRODUCTION	13
2 STUDY AREA.....	17
3 METHODOLOGIES	20
3.1 Field Instrumentation	20
3.2 Removing Tides.....	21
3.3 Empirical Orthogonal Functions (EOF)	21
3.3.1 EOF Analysis.....	22
3.3.2 Complex EOF Analysis.....	24
3.3.3 Hilbert EOF(HEOF) and Concatenated Hilbert EOF(CHEOF) Analysis	27
3.4 Depth-Averaged Momentum Balance.....	29
3.5 Estimation of Turbulent Kinetic Energy (TKE) Dissipation Rate.....	31
4 MEASUREMENTS AND DATA PROCESSING.....	35
4.1 Shelf Aligned Coordinate System	35
4.2 Wind and Current Velocities	37
5 SPECTRUM ANALYSIS AND LOWPASS-FILTERED DATA.....	44
5.1 Spectrum Analysis	44
5.2 Low-Pass Filtered Wind and Current Velocities.....	48
6 COMPARISON BETWEEN EOF ANALYSES	65
6.1 Deployment 7-1	65
6.2 Deployment 8-1	71
6.3 Deployment 9-1	74
7 DYNAMICS OF WIND-DRIVEN SHELF CIRCULATION.....	93

7.1 Cross-Shelf Momentum Balance	93
7.2 Along-Shelf Momentum Balance	95
7.3 The Dissipation of Turbulent Kinetic Energy	96
8 SUMMARY	104
LIST OF REFERENCES	107
BIOGRAPHICAL SKETCH	113

LIST OF TABLES

<u>Table</u>		<u>Page</u>
3-1	ADCP Mooring information	34
6-1	Total energy or variance of each mode in the cross- and along-shelf current field	78
7-1	Statistics of terms in the cross-shelf momentum budgets during Deployment 7-1, 8-1 and 9-1. Units are 10^{-6} m/s^2	99
7-2	Statistics of terms in the along-shelf momentum budgets during Deployment 7-1, 8-1 and 9-1. Units are 10^{-6} m/s^2	99

LIST OF FIGURES

<u>Figure</u>	<u>Page</u>
2-1 Map of the northeastern Gulf of Mexico showing the shelf topography, the locations of the weather stations and ADCP mooring.....	19
4-1 During Deployment 7-1 wind plot with the direction of cross- and along-shelf direction. The vertical structure of the cross-shelf currents	41
4-2 During Deployment 8-1 wind plot with the direction of cross- and along-shelf direction. The vertical structure of the cross-shelf currents	42
4-3 During Deployment 9-1 wind plot with the direction of cross- and along-shelf direction. The vertical structure of the cross-shelf currents	43
5-1 Vertical spectrum density ((cm/s) ² /cpd) distribution of East-West and North-South currents and cross- and along-shelf currents during Deployment 7-1	54
5-2 Spectrum density ((m/s) ² /cpd) of East-West and North-South winds and cross- and along-shelf winds during Deployment 7-1	54
5-3 Vertical spectrum density ((cm/s) ² /cpd) distribution of East-West and North-South currents and cross- and along-shelf currents during Deployment 8-1	55
5-4 Spectrum density ((m/s) ² /cpd) of East-West and North-South winds and cross- and along-shelf winds during Deployment 8-1	55
5-5 Vertical spectrum density ((cm/s) ² /cpd) distribution of East-West and North-South currents and cross- and along-shelf currents during Deployment 9-1	56
5-6 Spectrum density ((m/s) ² /cpd) of East-West and North-South winds and cross- and along-shelf winds during Deployment 9-1	56
5-7 The vertical distribution of RSD ((cm/s) ² /cpd) for counter-clockwise rotation and clockwise rotation during Deployment 7-1	57
5-8 The vertical distribution of RSD ((cm/s) ² /cpd) for counter-clockwise rotation and clockwise rotation during Deployment 8-1	57
5-9 The vertical distribution of RSD ((cm/s) ² /cpd) for counter-clockwise rotation and clockwise rotation during Deployment 9-1	58
5-10 During Deployment 7-1 low-pass filtered wind plot. The vertical structures of low-pass filtered cross- and along-shelf velocities.....	59
5-11 Time series of lowpass-filtered wind velocity (m/s), and horizontal current velocity (cm/s) at the heights during Deployment 7-1.....	60

5-12	During Deployment 8-1 low-pass filtered wind plot. The vertical structures of low-pass filtered cross- and along-shelf velocities.....	61
5-13	Time series of lowpass-filtered wind velocity (m/s), and horizontal current velocity (cm/s) at the heights during Deployment 8-1	62
5-14	During Deployment 9-1 low-pass filtered wind plot. The vertical structures of low-pass filtered cross- and along-shelf velocities.....	63
5-15	Time series of lowpass-filtered wind velocity (m/s), and horizontal current velocity (cm/s) at the heights during Deployment 9-1.	64
6-1	Comparison of EOF and HEOF analysis in the cross-shelf current during Deployment 7-1	79
6-2	Comparison of CEOF and CHEOF analysis in the cross-shelf current during Deployment 7-1	80
6-3	The first and second mode (eigenvectors) of cross-shelf currents using EOF, HEOF, CEOF and CHEOF methods during Deployment 7-1.	81
6-4	The first and second mode (eigenvectors) of along-shelf currents using EOF, HEOF, CEOF and CHEOF methods during Deployment 7-1	82
6-5	Comparison of EOF, HEOF, CEOF and CHEOF analysis in the along-shelf current during Deployment 7-1	83
6-6	Comparison of correlation coefficient between EOF modes: EOF, HEOF, CEOF and CHEOF, and shelf aligned winds during Deployment 7-1	84
6-7	Comparison of CEOF and CHEOF analysis in the cross-shelf current during Deployment 8-1	85
6-8	The first and second mode (eigenvectors) of cross-shelf currents using CEOF and CHEOF methods during Deployment 8-1	86
6-9	The first and second mode (eigenvectors) of along-shelf currents using CEOF and CHEOF methods during Deployment 8-1	86
6-10	Comparison of CEOF and CHEOF analysis in the along-shelf current during Deployment 8-1	87
6-11	Comparison of correlation coefficient between EOF modes CEOF and CHEOF, and shelf aligned winds during Deployment 8-1	88
6-12	Comparison of CEOF and CHEOF analysis in the cross-shelf current during Deployment 9-1	89

6-13	The first and second mode (eigenvectors) of cross-shelf currents using CEOF and CHEOF method during Deployment 9-1	90
6-14	The first and second mode (eigenvectors) of along-shelf currents using CEOF and CHEOF method during Deployment 9-1	90
6-15	Comparison of CEOF and CHEOF analysis in the along-shelf current during Deployment 9-1.	91
6-16	Comparison of correlation coefficient between EOF modes: CEOF and CHEOF, and shelf aligned winds during Deployment 9-1	92
7-1	Time series of cross-shelf momentum terms: wind stress, Coriolis acceleration, bottom stress and local acceleration during Deployment 7-1	100
7-2	Time series of cross-shelf momentum terms: wind stress, Coriolis acceleration, bottom stress and local acceleration during Deployment 8-1	100
7-3	Time series of cross-shelf momentum terms: wind stress, Coriolis acceleration, bottom stress and local acceleration during Deployment 9-1	101
7-4	Time series of along-shelf momentum terms: wind stress, Coriolis acceleration, bottom stress and local acceleration during Deployment 7-1	101
7-5	Time series of along-shelf momentum terms: wind stress, Coriolis acceleration, bottom stress and local acceleration during Deployment 8-1	102
7-6	Time series of along-shelf momentum terms: wind stress, Coriolis acceleration, bottom stress and local acceleration during Deployment 9-1	102
7-7	Spectrum density of water surface height (m) dealing without a band-stop filter with a band-stop filter.....	103
7-8	Time series of wind vector plots with the along- and cross-shelf direction and Turbulent Kinetic Energy Dissipation rate.....	103

LIST OF ABBREVIATIONS

ADCP	ACOSTIC DOPPLER CURRENT PROFILER
CEOF	COMPLEX EMPIRICAL ORTHOGONAL FUNCITON
CHEOF	CONCATINATED HILBERT EMPIRICAL ORTHOGONAL FUNCITON
EOF	Empirical Orthogonal Function
HEOF	HILBERT EMPIRICAL ORTHOGONAL FUNCTION
NDBC	NATIONAL DATA BUOY CENTER
PCA	PRINCIPAL COMPONENT ANALYSIS
PCs	PRINCIPAL COMPONENTS
TKE	TURBULENT KINETIC ENERGY

Abstract of Dissertation Presented to the Graduate School
of the University of Florida in Partial Fulfillment of the
Requirements for the Degree of Doctor of Philosophy

CROSS-SHELF EXCHANGE FLOW OVER THE WEST FLORIDA INNER SHELF

By

Sangdon So

August 2013

Chair: Arnaldo Valle-Levinson

Cochair: Louis H. Motz

Major: Civil Engineering

Moored currents and wind observations over the West Florida Inner Shelf indicate that the inner shelf ocean circulation is mainly driven by a combination of wind stress, pressure gradient and Coriolis force. Empirical Orthogonal Function (EOF) analyses are used to gain insight in understanding the shelf circulation dynamics associated with wind stress. The thickness of the surface and bottom boundary layers is strongly dependent on the strength of the wind. Cross-shelf wind also plays a substantial role to generate cross-shelf exchange flow. In the cross-shelf budget the dominant terms are wind stress and Coriolis acceleration that are balanced by the cross-shelf pressure gradient term. The along-shelf momentum is primarily dominated by the along-shelf wind stress, followed by bottom stress, Coriolis acceleration and local advection. The dissipation rate (ϵ) of Turbulent Kinetic Energy (TKE) is estimated to understand the vertical exchange of horizontal momentum. The vertical shear is enhanced by exchange flows in the interface between the bottom and surface boundary layer when wind stress is less than approximately 7 m/s. This causes the strong turbulent fluxes in the middle of water column.

CHAPTER 1 INTRODUCTION

This study investigates the dominant processes that drive inner shelf circulation over the West Florida Shelf. The motion of the shallow (<15m) nearshore region over the continental shelf, where surface and bottom boundary effects interact (Lentz, 1995), is influenced by many different factors. These factors include: Earth's rotation, wind, freshwater input, the baroclinic pressure gradient, the offshore current regime, the bottom bathymetry, and variations of coastline. The intricate variations of the coastline as well as the sloping bottom of the continental shelf accentuate the differences between the continental shelf and the deep ocean. The continental shelf circulation influences coastal ecosystem where most of the biological primary productivity of the world's oceans takes place (Allen, 1980).

The transport of sediments, nutrients, larvae, and pollutants is strongly affected by the exchange of water mass across the shelf (Nittrouer and Wright 1994, Falkowski et al. 1998, Epifanio and Garvine 2001, Garland et al. 2002, Grantham et al. 2004, Dudas et al. 2009). The exchange flow across the inner shelf as well as vertical transport play key roles in a wide range of interdisciplinary problems that motivate research on inner shelf circulation (Lentz and Fewings, 2012). In recent years, observational and numerical studies have focused on the inner shelf region to understand the import forcing mechanism in this region. Despite its importance and profound interest in this topic, the primary forcing mechanisms over the inner shelf have not been clearly defined.

The inner shelf is the transition region between the surf zone and the middle of the continental shelf, typically spanning water depths from a few meters to a few tens of

meters (Lentz and Fewings, 2012). The inner shelf has been defined as the near shore region where the surface and bottom boundary layers overlap (Lentz, 1995), where the surface and bottom Ekman layers interact (Liu and Weisberg, 2005), and where the surface and bottom boundary layers are dynamically important (Weisberg et al., 2001). All of these definitions are consistent. In the surfzone, breaking waves dominates the momentum balance. In contrast, a geostrophic balance between Coriolis forces and pressure gradient is expected at the mid and outer shelf. In these regions, the frictional surface and bottom boundary layers are well separated and thin relative to the water depth (Fewings and lentz, 2010). The thicknesses of the surface and bottom boundary layers are dependent on the strength of the wind and wave forcing and vertical density stratification; hence the location of inner shelf varies in time (Lentz and Fewings, 2012). Also In this zone, the wind driven currents have more effect on the dynamics of currents than in other shelf zones.

The wind-driven coastal setup and setdown over a sloping coastal region was first discussed by Ekman (1905). The study of wind-driven coastal circulation is complicated because it involves water depths comparable to the scale of the surface and bottom Ekman layers. In deep water, the wind-driven volume transport within the surface Ekman layer is perpendicular (in the northern hemisphere) to the wind stress. As water depth decreases, Earth's rotation is less important so the bottom stress modifies water to flow more downwind. In very shallow water, i.e., depths much smaller than the Ekman layer thickness, the effects of Earth's rotation can be neglected; while in deep water the bottom stress can be neglected (Poon, 1991). The wind-driven cross-shelf circulation is a key component of shelf dynamics and an important mechanism for

cross-shelf exchange on most shelves. However, the mechanisms that drive cross-shelf circulation and how it varies with stratification, bathymetry, and forcing mechanisms are not well understood because of, in part, a lack of observations (Lentz, 2001).

The depth-averaged momentum balance gives insight into the dynamics of subtidal currents over the inner shelf. All continental shelves have their own forcing mechanisms due to their geometries and boundary conditions. It is generally accepted that the depth-averaged cross-shelf momentum balance at mid-shelf is predominantly geostrophic; that is, the Coriolis force balances the motion produced by the cross-shelf pressure gradient (Thompson and Pugh, 1986; Brown et al., 1985, 1987; Lee et al., 1984, 1989; Lentz, 1994; Liu and Weisberg, 2005). The along-shelf momentum balance at mid-shelf is more complex. In particular, it is dominated by along-shelf wind stress and along-shelf pressure gradients that are balanced by both bottom friction and acceleration (Pettigrew 1981; Lentz and Winant 1986; Lee et al., 1989; Lentz et al., 1999; Liu and Weisberg, 2005).

Over the inner shelf, the cross- and along-shelf moment balance are more site-specific and depth dependent. The Coriolis term decreases as the pressure gradient term increases. In the near shore the balance is between the stresses (wind and bottom stress) and the pressure gradient terms, with the Coriolis term playing a secondary role. In the along-shelf direction, the bottom stress term becomes increasingly important with decreasing depth over the inner shelf (Liu and Weisberg, 2005). Previous observational references on the momentum balances and cross-shelf circulation over West Florida Inner Shelf are limited. Biological phenomena, sediment transport and water property distributions can be strongly affected by the cross-shelf circulation (Allen, 1980; Dever,

1997; Lentz and Fewings, 2012). This study, therefore, considers a force mechanism for driving cross-shelf exchange flow and the momentum balance for cross- and along-shelf flow over various time scales.

CHAPTER 2 STUDY AREA

The West Florida Shelf is broad and gently sloping. The Gulf of Mexico Loop Current can at times impinge on the shelf slope (Molinari et al., 1977; Huh et al., 1981; He and Weisberg, 2003; Liu and Weisberg, 2005). The fresh water of the Mississippi River influences the mid-shelf in spring and summer (Gilbes et al., 1996; He and Weisberg, 2002). Observations analyzed in this study were obtained from in close proximity to an artificial reef during seven deployments spanning summer, fall and winter in 2007, 2008 and 2009. An Acoustic Doppler Current Profiler (ADCP) was moored around 30 km off shore of Steinhatchee, Florida at 29°27.91'N, 83°37.66'W in the Florida Big Bend region (Figure 2-1). The average depth at the mooring location is approximately 10 m and the depth increases with distance from the coast. The bathymetry along the 50m isobath is approximately parallel to the coastline. The cross-shelf slope is gentle (approximately 3.3×10^{-4}) and the shelf break is about 300 km off the coast. The coastline is relatively straight between Apalachee Bay and Cedar Key so the flow is expected to follow its orientation.

The seasonal variation of the winds over the West Florida Shelf is studied by Liu and Weisberg (2012). The winds in the Florida Big Bend region from September through April tend to be southward or southwestward (upwelling favorable). During June and July, the winds tend to be northward or northeastward (downwelling favorable). The winds during May and August mainly blow northeastward and northwestward, respectively. In summer season the magnitude of the monthly mean winds is relatively small over the West Florida Shelf. Fresh water is discharged to West Florida Shelf from river discharges, estuaries, springs and rainfall. In North Florida, tropical storms often

produce heavy rain in spring. Considering the occurrence of tropical storms, riverine fresh water discharges primarily from Mississippi River peak in spring (Weisberg et al, 2005). Fresh water input from the other sources is heavily concentrated in summer because the highest rainfall amounts occur in summer except for North Florida (Florida Climate Center).

Ocean tides are major contributors to shelf currents. The tidal velocities at this study area are dominated by the M_2 tide, the lunar semidiurnal tide with a period of 12.42 h. The inertial motion with period 24.3 h is also an important element of variability in the flow motion. The semidiurnal constituent decreases in the offshore direction whereas the diurnal constituents are spatially uniform. As a result, the semidiurnal tide is the dominant frequency near the coast and the diurnal tide is strong in deep water (He and Weisberg, 2002). The circulation of the Gulf of Mexico is dominated by the energetic Loop Current and large anticyclonic rings, called Loop Current Eddies. These features stay away from the continental shelf because they have the vertical scales from several hundred to 1000 m (Morey et al, 2003). Although the Loop Currents and the associated eddies govern the circulation of deep water, the mechanisms driven by wind dominate the inner shelf circulations.

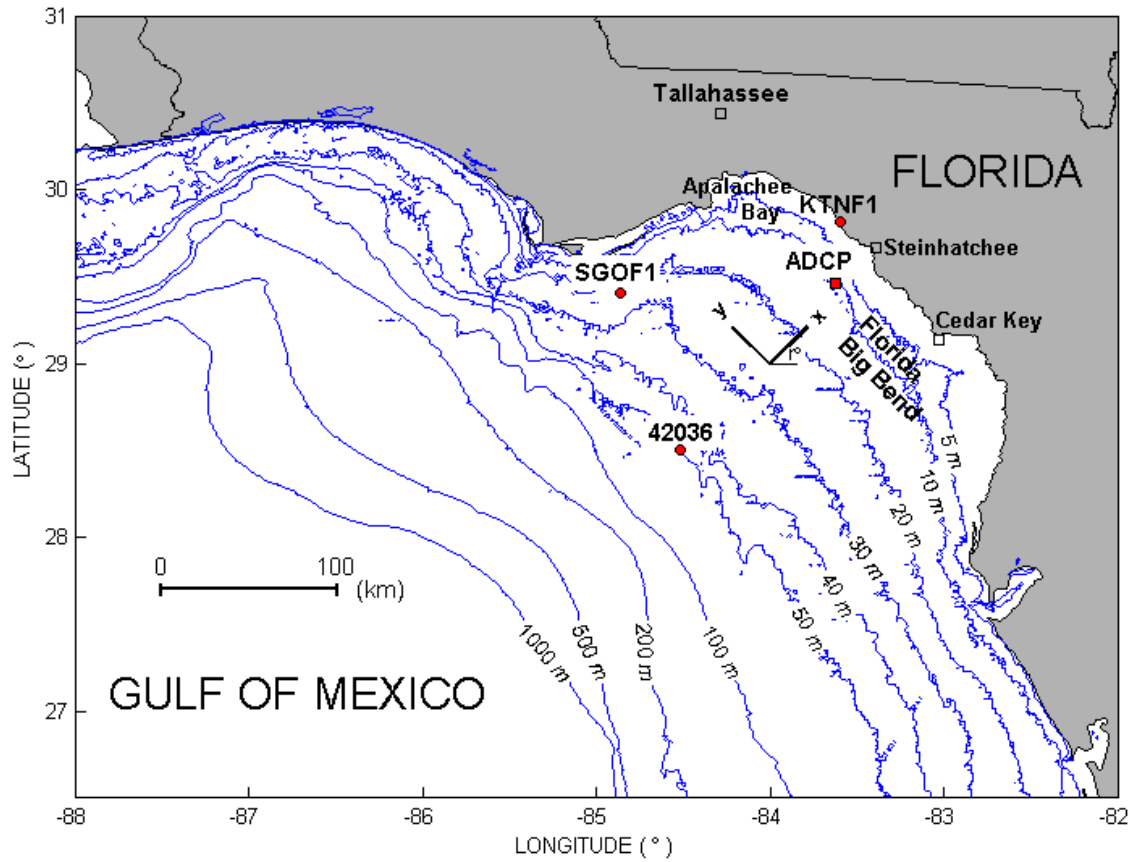


Figure 2-1. Map of the northeastern Gulf of Mexico showing the shelf topography, the locations of the weather stations and ADCP mooring and describing the rotated coordinate system

CHAPTER 3 METHODOLOGIES

3.1 Field Instrumentation

Wind data are obtained from National Data Buoy Center (NDBC) to qualitatively analyze the relation between current and wind velocities which are a significant driving force of currents in the continental shelf. Two of the meteorological stations are shown in Figure 2-1 and named as SGOF1 and 42036. In addition, time series of water velocity profiles are used to study the hydrodynamics in the inner-continental shelf. The upward looking ADCP was bottom mounted to collect water velocity profiles. ADCPs had sampling bins every meter. The sampling intervals are 10 minutes and 1 second as shown in Table 3-1. There are four periods in which a bottom-mounted ADCP was deployed in upward-looking configuration: December 2007 through January 2008, October through December 2008, June through October 2009 and November 2009. Table 3-1 provides supporting information of these deployments. Velocity data were discarded for periods when the signal correlation from the ADCP was low: 24 August to 9 September 2009.

For describing the shelf flow field, a Cartesian coordinate system(x, y, z) is used with the y -axis along-shore, the x -axis cross-shore and the z -axis vertical. The major principal axis direction is oriented r° counter-clockwise from the east to adjust the system across and along the continental shelf. The degree of r is determined with the tidal current direction that is roughly perpendicular to the local coastline (Figure 2-1). The mean direction in which the tidal currents propagate was estimated using Principal Component Analysis (PCA) of the bivariate data and spectral analysis. Both of these analyses are described in section 4.1 and their produced r -values are given in Table 3-1.

The origin is at the location where the ADCP was moored with x positive onshore, y positive along-shelf northward and z positive upward. The corresponding velocity components are u , v , w .

3.2 Removing Tides

As this study is primarily focused on the forcing mechanisms of sub tidal flows over the West Florida Inner Shelf, the wind and current velocities were low-pass filtered to remove tidal and other high-frequency variations. We refer to the filtered velocity as the subtidal flow. The filter used was a cosine Lanczos type with a cut-off at 25 h.

3.3 Empirical Orthogonal Functions (EOF)

Empirical Orthogonal Functions (EOF) may be used to understand the relationship between hydrodynamic and meteorological variables, for instance temperature, wind, pressure and currents in various places. In meteorology EOF analysis has been used to achieve a decomposition of a continuous space-time field (e.g. Obukhov 1947; Fukuoka 1951; Lorenz 1956; and Kutzbach 1967). This analysis has been used to identify or extract individual modes of variability that can describe the dominant physical phenomena and spatial/temporal scales behind the variability of sea surface temperature (Kutzbach 1967), winds (Hardy and Walton, 1978; Legler 1983), currents (Kundu and Allen 1976; Denbo and Allen 1984; Klinck 1985; Prandle and Matthews 1990; Ng 1993), and beach profile evolution (Winant et al. 1975).

Several studies (e.g. Wallace 1972; Horel 1981; Richman 1986) addressed difficulties in interpreting the obtained modes because physical phenomena are not necessarily orthogonal. The difficulties encourage researchers to develop other related methods such as Rotated EOF, Complex EOF, Concatenated Hilbert EOF, Real-vector

EOF, Extended EOF, Rotary EOF etc. The detailed information about the other methods can be found in Hannachi et al, (2007).

3.3.1 EOF Analysis

Geophysical data encompass a set of highly complex interactions of times series on a grid of spatial points. Given any space-time variability, EOF analysis identifies a set of physically or dynamically independent spatial patterns associated with a set of uncorrelated time series or Principal Components(PCs) (Hannachi et al, 2007). EOFs find the principal axis to maximize the variation of data (Preisendorfer, 1988).

Conventional EOF analysis can be applied to a single scalar variable and seeks “stationary” patterns that can be described by a spatial mode and PCs multiplied by an amplitude time series. This conventional time domain EOF analysis is useful for detecting standing wave patterns in the sense that they are not evolving. However, the method can be extended to the Complex EOFs or Hilbert EOFs to study propagating wave phenomena as described in 3.2.2 and 3.2.3.

Let us suppose that there is a data matrix composed of a space-time field $\psi(x_i, t_j)$ at each location $x_i, i = 1, 2, \dots, p$, and time $t, j = 1, 2, \dots, n$ that can be expressed by the inner product of spatial and temporal modes. In this study the data matrix represent a time series of along- and cross-shelf current speeds at each bin. There will be M spatial modes $E(x_p), k = 1, 2, \dots, M$, each having a time series $a_k(t_n)$ with n ensembles, which can fully describe data matrix ψ . The total number of modes (M) contained in the field is equivalent to the number of stations (p).

$$\begin{pmatrix} \psi(x_1, t_1) & \cdots & \psi(x_1, t_n) \\ \vdots & \ddots & \vdots \\ \psi(x_p, t_1) & \cdots & \psi(x_p, t_n) \end{pmatrix} = \begin{pmatrix} E_1(x_1) & \cdots & E_M(x_1) \\ \vdots & \ddots & \vdots \\ E_1(x_p) & \cdots & E_M(x_p) \end{pmatrix} \begin{pmatrix} a_1(t_1) & \cdots & a_1(t_n) \\ \vdots & \ddots & \vdots \\ a_M(t_1) & \cdots & a_M(t_n) \end{pmatrix} \quad (3-1)$$

Alternatively, we can represent the data matrix as the sum of a set of spatial modes and amplitude time series.

$$\psi(\mathbf{x}_i, t_j) = \sum_{k=1}^M E_k(\mathbf{x}_i) a_k(t_j) \quad (3-2)$$

where $a_k(t)$ is the amplitude time series of the k^{th} mode and $E(x)$ is the spatial pattern of the k^{th} mode. The modes are orthogonal, which allows the simple decomposition into the product $E_k a_k$.

$$\sum_{k=1}^M E_i(\mathbf{x}_k) E_j(\mathbf{x}_k) = \delta_{ij} \quad \text{or} \quad \mathbf{E}_i^T \mathbf{E}_j = \delta_{ij} \begin{cases} 1, & i = j \\ 0, & i \neq j \end{cases} \quad (3-3)$$

There is an infinite set of possible choices for E that would compose a set of linearly independent functions that could describe data matrix ψ . To find the uncorrelated linear combinations ($E_k a_k$) the EOFs that maximize λ are uniquely determined among the many possible choices. These are restricted to the time series of amplitudes $a_k(t)$ that is also uncorrelated in each mode as denoted by

$$\overline{a_i(t) a_j(t)} = \lambda_i \delta_{ij} \quad (3-4)$$

where the over bar represents ensemble average. The variance is given by

$$\overline{a_i^2(t)} = \lambda_i \quad \text{or} \quad \lambda_i = \frac{1}{n} \mathbf{a}_i^T \mathbf{a}_i \quad (3-5)$$

From Equations (3-3), (3-4) and (3-5) we intuitively see that the EOFs are obtained with the covariance of the data matrix. The covariance matrix S of ψ is a matrix whose element in the k, m position has the covariance between the k^{th} and m^{th} random vectors as defined by

$$S = \frac{1}{n} \boldsymbol{\psi} \boldsymbol{\psi}^T \quad (3-6)$$

S contains the elements of covariances s_{km} at any pair of grid points (s_k, s_m) that describes the association between time series of the field for k , and $m = 1, 2, \dots, p$, i.e.

$$s_{km} = \frac{1}{n} \sum_{j=1}^n \psi_k(t_j) \psi_m(t_j) \quad (3-7)$$

Matrix S is a symmetric matrix (i.e. $S = S^T$) and possesses a set of M real eigenvalues λ_k , and eigenvectors E_k . Using Equation (3-2) and (3-6) the eigenvalue problem is derived as follows.

$$\frac{1}{n} \boldsymbol{\psi} \boldsymbol{\psi}^T = \frac{1}{n} \mathbf{E} \mathbf{a} \mathbf{a}^T \mathbf{E}^T \quad (3-8)$$

From Equation (3-5) Equation (3-8) is given as

$$\frac{1}{n} \boldsymbol{\psi} \boldsymbol{\psi}^T = \mathbf{E} \boldsymbol{\lambda} \mathbf{I} \mathbf{E}^T \quad (3-9)$$

where I denotes the $M \times M$ identity matrix. Multiplying E on the both side of Equation (3-9) becomes

$$S \mathbf{E}_k = \lambda_k \mathbf{E}_k \quad (3-10)$$

The classic eigenvalue problem can be defined by Equation (3-10). The EOFs are therefore sought from the solution to the eigenvalue problem. The set of eigenvectors represent the unit vectors of the sample data that are orthogonal to each other. The associated eigenvalues address the amplitude along the unit vectors of the sample data. Therefore, the variations in those new directions are uncorrelated with each other. To quantify the contribution of each mode to the total field the variance or energy spectrum λ_k associated with each mode is expressed as

$$\frac{100\lambda_k}{\sum_{k=1}^M \lambda_k} (\%) \quad (3-11)$$

3.3.2 Complex EOF Analysis

Kundu and Allen (1976) used the complex EOF analysis, which is applied to the complex field obtained from a pair of associated variables such as the u , v components of the velocity vector field. This method has been widely used in oceanography and

meteorology (Klinck 1985; Brink and Muench 1986; Prandle and Matthews 1990; Kaihatu et al. 1998; von Storch and Zwiers, 2003). Complex EOF analysis was also employed to separate barotropic and baroclinic velocity structures in shallow water and proposed as a better alternative to depth-averaging methods to estimate barotropic tidal currents (Edwards and Seim, 2008).

Conventional EOF analysis as mentioned in 3.2.1 can be applied to a single space-time field or a combination of fields and finds “stationary” patterns in the sense that they are not evolving. It yields a varying time series for any obtained orthogonal pattern, which means that the time series will only decrease or increase in magnitude whereas the spatial structure remains the same (Hannachi et al, 2007). In particular, the use of the covariance matrix at zero lag restricts the analysis to detect the stationary patterns that are in phase or π out of phase over the array (Merrifield and Guza, 1990). There are, in principle, two ways to perform complex EOFs, namely ‘conventional’ complex EOFs (CEOF) and ‘Hilbert’ EOFs (HEOF) to identify propagating patterns.

In the conventional complex analysis, the current field $U(x_l, t)$, defined at each location x_l , $l = 1, 2, \dots p$, and time $t = 1, 2, \dots n$, can be formed into a complex number as:

$$U(x_l, t) = u(x_l, t) + iv(x_l, t) \quad (3-12)$$

where $i = \sqrt{-1}$. The complex autocorrelation (covariance) matrix of U is defined as

$$S = \frac{1}{n} \mathbf{U} \mathbf{U}^{*T} \quad (3-13)$$

where the asterisk denotes complex conjugate. The matrix S is Hermitian, i.e. $S^{*T} = S$, which always has a set of M linearly independent, and mutually orthonormal, eigenvectors, regardless of the eigenvalue multiplicity (Navarra and Simoncini, 2010).

Once the spatial eigenvectors are calculated by the eigenvalue problem, their corresponding time evolution of the k^{th} mode of the EOF is given by projecting the complex data series U onto the proper eigenvector E_k that produces a map of current speeds $E(x_l)$ and angles $\theta(x)$, namely.

$$E(x_l) = |E(x_l)|e^{-i\theta(x_l)} \quad (3-14)$$

$$a_k(t) = \sum_{l=1}^M U(x_l, t)E_k(x_l) \quad (3-15)$$

By definition, the k^{th} complex EOF mode consists of a spatial structure E_k and temporal amplitude $a_k(t)$. The product of $a_k(t)E_k(x)$ represents a linearly independent combination of reconstructed data. Therefore the original complex data $U(x_l, t)$ can be reconstructed by summing the product of all modes as follows:

$$U(x, t) = \sum_{k=1}^M a_k(t)E_k(x) \quad (3-16)$$

The obtained CEOFs provide the spatial amplitude $A_k(x)$ and phase $\phi_k(x)$ function. The spatial amplitude functions show the spatial distribution of variability associated with each eigenmode. The spatial phase functions describe the relative phase fluctuation among the various spatial locations. The spatial amplitude and phase functions are as follows:

$$A_k(x) = \sqrt{E_k^*(x)E_k(x)} \quad (3-17)$$

$$\phi_k(x) = \tan^{-1} \left(\frac{\text{Im}\{E_k(x)\}}{\text{Re}\{E_k(x)\}} \right) \quad (3-18)$$

The temporal amplitude function $B_k(t)$ measures the temporal variability in the magnitude of the modal structure of the field. The temporal phase function $\theta_k(t)$ gives information on the temporal variation of phase. The temporal amplitude and phase functions are given by

$$B_k(t) = \sqrt{a_k^*(t)a_k(t)} \quad (3-19)$$

$$\theta_k(t) = \tan^{-1} \left(\frac{\text{Im}\{a_k(t)\}}{\text{Re}\{a_k(t)\}} \right) \quad (3-20)$$

Equations (3-17) through (3-20) give information on the propagating features and periodicity in the original data field.

3.3.3 Hilbert EOF(HEOF) and Concatenated Hilbert EOF(CHEOF) Analysis

As mentioned in 3.2.2, the CEOF analysis is commonly used in oceanography and meteorology in particular for wind and current vectors. Preisendorfer (1988) and Kaihatu et al. (1998) noticed ambiguity in the direction of the resulting eigenstructures with the conventional CEOFs because of the reduction of the vector nature of the data to that of a complex scalar. There is another method associated with complex EOFs, namely HEOFs. The straightforward way to work with HEOFs is to complexify a random vector by adding its Hilbert transform as an artificial imaginary component (von Storch and Zwiers, 2003).

HEOF analysis is useful for detecting propagating patterns in the time domain by introducing the imaginary component that is shifted 90° from the real variable. HEOFs can be applied to a single variable or scalar in the same fashion as the EOF analysis described in section 3.2.1. HEOFs can also be extended to vector fields, i.e. two or more fields, through concatenation of the respective complexified field (Barnett, 1983), which is referred as CHEOFs in this study. With the HEOF method the individual components (u , v) of ocean current fields can be analyzed separately and the results are considered as decoupled scalars. The CHEOFs can be applied to the vector field. Unlike the CEOF method there is no ambiguity in the direction of the eigenstructures with the HEOF and CHEOF method.

The HEOF and CHEOF methods are based on the Hilbert transform that shifts the phase of the frequency components of a time series by $\pm 90^\circ$. Let $x_t = (x_{t1}, x_{t2}, \dots, x_{tp})^T$, $t = 1, 2, \dots, n$, be a scalar field, with Fourier representation

$$x_t = \sum_{\omega} a(\omega) \cos(\omega t) + b(\omega) \sin(\omega t) \quad (3-21)$$

where $a(\omega)$ and $b(\omega)$ are vector Fourier coefficients and ω is frequency. Since propagating disturbances require complex representation, Equation (3-21) can be transformed to yield the general complex Fourier decomposition. The new complex field $y_t = (y_{t1}, y_{t2}, \dots, y_{tp})^T$ can therefore be written as

$$y_t = x_t \mp iH \quad \text{where} \quad \begin{cases} -iH & \text{for } \omega > 0 \\ +iH & \text{for } \omega \leq 0 \end{cases} \quad (3-22)$$

The imaginary part of y_t , which is the Hilbert transform of x_t , is given by

$$H(x_t) = \sum_{\omega} b(\omega) \cos(\omega t) - a(\omega) \sin(\omega t) \quad (3-23)$$

The Hilbert transform $H(x_t)$ is identical to original time series x_t except for a simple phase shift by $\pi/2$. The HEOFs are then sought from the eigenvectors of the Hermitian covariance matrix

$$S_{yy} = \frac{1}{n} y_t y_t^{*T} = 2(S_{xx} + iS_{H(x)x}) \quad (3-24)$$

where $S_{H(x)x}$ is the cross-covariance matrix between $H(x_t)$ and x_t . From the set of eigenvectors the temporal amplitude and the reconstructed spatial modes are found as mentioned in section 3.2.2. Also explained in section 3.2.2, the spatial/temporal amplitude and phase are obtained by Equations (3-17) through (3-20).

As mentioned above, CHEOF analysis is also based on the Hilbert transform. CHEOF analysis is even used with the data matrix, which has different data types. The process of CHEOF analysis is the same as HEOF except for the concatenation. The

data matrix can be constructed in order to combine different data types. In this study CHEOF analysis is employed to a time series of ocean currents (u, v) . The solution of CHEOF yields the $2M$ independent spatial modes, since S_{yy} is a Hermitian matrix having size $2M \times 2M$ due to the concatenation. However, the other analyses provide the M independent modes. The number of modes M is equivalent to the number of stations where data are measured.

3.4 Depth-Averaged Momentum Balance

The depth-average momentum balance provides insights into the dominant forces that drive the inner shelf flow. An analysis of the depth-averaged along-shelf and cross-shelf momentum equations was performed using observations. The depth-averaged momentum balance equations (Lentz et al. 1999), assuming hydrostatic flow and small sea level variations compared with the water depth ($h \gg \eta$), are

$$\frac{\partial \tilde{u}}{\partial t} + \frac{1}{h} \frac{\partial}{\partial x} \int_{-h}^0 u^2 dz + \frac{1}{h} \frac{\partial}{\partial y} \int_{-h}^0 uv dz - f \tilde{v} = -\frac{1}{\rho_0} \frac{\partial P}{\partial x} + \frac{\tau_{sx}}{\rho_0 h} - \frac{\tau_{bx}}{\rho_0 h} \quad (3-25)$$

$$\frac{\partial \tilde{v}}{\partial t} + \frac{1}{h} \frac{\partial}{\partial y} \int_{-h}^0 v^2 dz + \frac{1}{h} \frac{\partial}{\partial x} \int_{-h}^0 uv dz + f \tilde{u} = -\frac{1}{\rho_0} \frac{\partial P}{\partial y} + \frac{\tau_{sy}}{\rho_0 h} - \frac{\tau_{by}}{\rho_0 h} \quad (3-26)$$

where (u, v) are the cross-shelf and along-shelf subtidal components of velocity, and (\tilde{u}, \tilde{v}) are their corresponding depth-averaged values. The reference coordinates are x, y, z denoting the cross-shelf, along-shelf and vertical direction ($z = 0$ is located at mean water level over each deployment) and h is the water depth. The Coriolis parameter, f , is calculated by $2\Omega \sin \phi$ where Ω is the earth's rotational vector and ϕ is latitude. The reference density, ρ_0 , is taken to be 1025 kg/m^3 and g is gravitational acceleration. $\partial P / \partial x$ and $\partial P / \partial y$ are the depth-averaged horizontal pressure gradient. τ_{sx} and τ_{sy} are the wind stress, and τ_{bx} and τ_{by} are the bottom stress. Nonlinear

advection terms which are the second and third term on the left hand side of Equation (3-25) and (3-26) can be neglected and the equations above become:

$$\frac{\partial \tilde{u}}{\partial t} - f \tilde{v} = -\frac{1}{\rho_0} \frac{\partial P}{\partial x} + \frac{\tau_{sx}}{\rho_0 h} - \frac{\tau_{bx}}{\rho_0 h} \quad (3-27)$$

$$\frac{\partial \tilde{v}}{\partial t} + f \tilde{u} = -\frac{1}{\rho_0} \frac{\partial P}{\partial y} + \frac{\tau_{sy}}{\rho_0 h} - \frac{\tau_{by}}{\rho_0 h} \quad (3-28)$$

The acceleration term is estimated as a centered difference of the current observations with 10 minute intervals. The pressure near the bottom P_b , assuming hydrostatic flow, can be computed as the sum of the surface pressure P_s (including contributions from the sea surface slope and the atmospheric pressure) and density (ρ) contributions (Lentz et al., 1999), namely

$$P_b = P_s + g \int_{-h}^0 \rho dz \quad (3-29)$$

It should be noted that ρ is the sum of a reference density, ρ_0 , and a small density anomaly, $\rho'(x, y, z, t)$, due to spatial and temporal variability. By differentiating Equation (3-29) along x , the cross-shelf pressure gradient $\partial P / \partial x$ is given by

$$\frac{\partial p}{\partial x} = \frac{\partial P_s}{\partial x} + \int_{-h}^0 g \frac{\partial \rho}{\partial x} \left(1 + \frac{z}{h}\right) dz, \quad (3-30)$$

with a corresponding equation for $\partial P / \partial y$. On the right-hand side of Equation (3-30) the first and second term will be referred to as the barotropic pressure gradient and the baroclinic pressure gradient, respectively. Direct pressure gradient estimates are not possible with the data available, but the stress, Coriolis and local acceleration terms were calculated and given in sections 6.1 and 6.2.

To estimate bottom stress a quadratic drag law was used as follows:

$$\tau_b = \rho_0 C_D |\mathbf{u}_b| \mathbf{u}_b, \quad (3-31)$$

where \mathbf{u}_b is the horizontal velocity vector measured at the first bin of each deployment and C_D is the dimensionless drag coefficient. The bottom drag coefficient C_D is estimated for the West Florida Shelf from numerical models (Li and Weisberg, 1999a and 1999b; He and Weisberg, 2002; He et al., 2004) as

$$C_D = \max \left\{ 2.5 \times 10^{-3}, \left[\frac{1}{\kappa} \ln \left(\frac{H+z_b}{z_0} \right) \right]^{-2} \right\}, \quad (3-32)$$

where κ is the von Karman constant, z_0 is the bottom roughness length, z_b is the grid point nearest the bottom, and H is the water depth. Except near shore, the C_D is generally 2.5×10^{-3} in those WFS model calculations using the Princeton Ocean Model of Blumberg and Mellor (1987).

3.5 Estimation of Turbulent Kinetic Energy (TKE) Dissipation Rate

Measurements of TKE dissipation rate (ϵ) in the ocean aid in understanding vertical exchange processes and parameterization (Simpson et al., 1996; Burchard et al., 1998; Gargett, 1999; Sharples et al., 2001; MacKinnon and Gregg, 2003; Wiles et al., 2006). Vertical exchange driven by turbulent mixing plays a key role in transporting momentum, heat fluxes, sediment and nutrients in the marine environment (Wiles et al., 2006). Experimental studies using microstructure profilers is labor intensive and requires a dedicated ship; thus, data sets tend to be sparse, intermittent and rarely exceed one or two days duration.

Wiles et al. (2006) presented a new technique for the estimation of TKE dissipation rate using a 1200 kHz RDI workhorse ADCP. The estimation was based on a structure function method developed by radar meteorologists for atmospheric studies (Lhermitte, 1968; Sauvageot, 1992). The structure function method was validated with simultaneous measurements from a Fast-Light-Yoyo (FLY) microstructure profiler. In

this study we adapted the new method based on the structure function to estimate the TKE dissipation rate.

Data from Deployment 9-5 were used to evaluate the rate of dissipation. The water column is divided into 20 bins (Table 3-1) with 0.5 m between bins. The time series for each bin was averaged over 10 minutes, which is long enough to give statistical reliability, but short enough for the time series to be assumed stationary (Willes et al., 2006). To extract the velocity fluctuation part of currents, v' , the temporal mean was subtracted from the observed current data for each bin. The second order structure function $D(z, r)$ can be defined at a location z as the covariance of the difference in the velocity fluctuation, v' , between two points z and $z+r$, as

$$D(z, r) = \overline{(v'(z) - v'(z+r))^2}. \quad (3-33)$$

The technique to measure the dissipation rate (ϵ) of TKE in a turbulent flow is based on the simple scaling analysis of the TKE equation (Tennekes and Lumley, 1972; Pope, 2000). Length, velocity, and time scales cannot be formed from ϵ alone. According to the Kolmogorov's second similarity hypothesis (Pope, 2000) $D(z, r)$ is independent of the kinematic viscosity ν in the inertial subrange. In this case the velocity difference between two points separated by r is largely derived by the eddies with a length scale comparable to r and an associated velocity scale of s' , that is,

$$D(z, r) \sim s'^2. \quad (3-34)$$

Given an eddy size r in the inertial subrange, the characteristic velocity scale s' for the isotropic turbulent eddies is related with r and ϵ in the conception of the energy cascade,

$$\epsilon \sim \frac{s'^3}{r}. \quad (3-35)$$

Hence, Equation (3-34) can be written as

$$D(z, r) = C_v^2 (\epsilon r)^{2/3}, \quad (3-36)$$

where C_v^2 is a constant which has been found to be between 2.0 and 2.2 (Sauvageot, 1992). The Kolmogorov hypotheses are sufficient to evaluate the second order structure function in terms of r , ϵ , and C_v in the inertial sub range, i.e. $l_K \ll r \ll l_K$, where l_K is Kolmogorov microscale. Therefore, the value of r is between the scale of dissipation and the vertical scale of the largest energy containing eddies (Ozmidov scale in stratified flow, l_K). From Equation (3-36) the TKE dissipation rate ϵ is readily obtained. The detailed description to estimate the dissipation is given in Wiles et al. (2006).

Table 3-1. ADCP Mooring information

Deployment number	Good bins	Interval (seconds)	Axis rotation(r°)	Observation period
7-1	1-20	600	45	12/19/2007-01/16/2008
8-1	1-20	600	45	10/10/2008-12/18/2008
9-1	1-20	600	45	06/02/2009-08/21/2009
9-2	-	600	-	08/24/2009-09/09/2009
9-3	1-20	600	34	09/09/2009-10/01/2009
9-4	1-20	600	45	10/13/2009-10/26/2009
9-5	1-20	1	34	11/18/2009-11/27/2009

CHAPTER 4 MEASUREMENTS AND DATA PROCESSING

Current velocity measurements over the continental shelf have shown varying characteristics in different shelf regions (Mitchum and Sturge 1982, Dever 1997, Lentz 2001, Tilburg 2003, Weisberg et al. 2005, Kirincich and Lentz 2009). These observations have also shown that shelf circulation is influenced by winds, shelf geometry, buoyancy from the atmosphere, freshwater input and offshore currents. It appears that the most common mechanism of shelf circulation is wind forcing (Allen, 1980). In order to characterize the inner shelf hydrodynamics over the West Florida Shelf, data were collected in seven different measurement periods as shown in Table 2-1. Wind velocities, water surface heights and current velocities are described in this chapter for the first three measurement periods: Deployment 7-1, 8-1 and 9-1. The analysis of these data is focused on the first three deployments when cross-shelf exchange flow was most active.

4.1 Shelf Aligned Coordinate System

A coordinate system is adopted with along-shelf direction approximately aligned with the shelf isobaths. The cross-shelf direction is oriented by the tidal currents which propagate roughly in a direction perpendicular to the coastline. To estimate the tidal direction, principal component analysis (Preisendorfer, 1988) of the bivariate data set was applied to the east-west and north-south current velocities. Suppose that $x(t)$ and $y(t)$ are respectively the east-west and north-south current velocities. The averaged current velocities over n number of observations are

$$\bar{x} = \frac{1}{n} \sum_t^n x \quad \text{and} \quad \bar{y} = \frac{1}{n} \sum_t^n y. \quad (4-1)$$

The fluctuating part of $x'(t)$ and $y'(t)$ can be expressed by the anomalies as follows

$$x'(t) = x(t) - \bar{x} \quad \text{and} \quad y'(t) = y(t) - \bar{y} \quad (4-2)$$

Thus we can rotate the frame of the given data set to a new orientation that is rotated by θ radians counterclockwise. The current velocities in the rotated frame can be expressed as

$$a_1(t) = x'(t)\cos\theta + y'(t)\sin\theta \quad (4-3)$$

$$a_2(t) = -x'(t)\sin\theta + y'(t)\cos\theta \quad (4-4)$$

In this rotated frame, we can calculate the variance, σ^2 , along the direction of the vector $e(\theta) = (\cos\theta, \sin\theta)^T$ (here “ T ” denotes matrix transpose), namely

$$\sigma^2(\theta) = (n-1)^{-1} \sum_t^n (x'(t)\cos\theta + y'(t)\sin\theta)^2 \quad (4-5)$$

$$\sigma^2(\theta) = \sigma_{xx}\cos^2\theta + 2\sigma_{xy}\sin\theta\cos\theta + \sigma_{yy}\sin^2\theta \quad (4-6)$$

where

$$\sigma_{xx} = (n-1)^{-1} \sum_t^n x'^2(t) \quad (4-7)$$

$$\sigma_{yy} = (n-1)^{-1} \sum_t^n y'^2(t) \quad (4-8)$$

$$\sigma_{xy} = (n-1)^{-1} \sum_t^n x'(t)y'(t) \quad (4-9)$$

The principal angles of the bivariate data set $x(t)$ and $y(t)$ occur at the axis where the variance, $\sigma^2(\theta)$, is maximized. These angles may be found by setting

$$\frac{d\sigma^2(\theta)}{d\theta} = (\sigma_{yy} - \sigma_{xx})\sin 2\theta + 2\sigma_{xy}\cos 2\theta = 0. \quad (4-10)$$

Therefore, an explicit expression for the rotation angles θ' from the original frame is given as

$$\tan 2\theta' = 2\theta_{xy}/(\sigma_{xx} - \sigma_{yy}) \quad (4-11)$$

Based on the principal angles of the current data, currents are oriented to along- and cross-shelf direction. The estimated principal angles of each deployment are given

in Table 2-1. Spectrum densities, $(\text{cm/s})^2/\text{cpd}$ (cycle per day), in section 5.1 show how well the tidal energies of currents transfer to cross-shelf direction.

4.2 Wind and Current Velocities

Wind and current measurements were obtained to understand the motion of the shallow nearshore region over the West Florida Shelf. The winds during Deployment 7-1 in Figure 4-1 A were collected from SGOF1. Wind directions are predominantly either northward (down-welling favorable) or southward (up-welling favorable). The wind vectors designate the exact geographic direction that is displayed with the direction compass on the left top side of Figure 4-1 A. The mean wind speed was 6.9 m/s during Deployment 7-1. Winds faster than ~ 10 m/s influenced the period from Jan. 1 to 3 of 2008, with the strongest wind (18.5 m/s) in that period occurring at 9:30 AM on Jan. 2. The red and blue dotted lines give the directions of the cross- and along-shelf currents. The positive values on the cross-shelf direction indicate onshore currents and positive along-shelf currents flow is toward northwest.

Water surface height is shown in Figure 4-1 B, which indicates that this study area is dominated by the semidiurnal harmonic constituents (M2). The semidiurnal tides in the Florida Big Bend region have been analyzed by previous investigations. Marmorino (1983) found that the semidiurnal tidal constituents decrease in the offshore direction but the diurnal components (K1 and S1) are more uniform across the shelf. As a result, the diurnal currents dominate in deep water and the semidiurnal currents are predominant near the coast (He and Weisberg, 2002). The mean water surface height was 13.4 m and the maximum value, 14.1 m occurred at 16:00 on Jan. 8. Semidiurnal tidal currents from Jan. 1 to 3 during strong winds almost vanished as diurnal currents from winds which had a large effect on the water motion over the Inner shelf. The sea

level drop can be clearly seen with the low-pass filtered time series given in Figure 5-10 B. The water setdown near the coast suggests that upwelling likely occurred over the inner shelf.

Figure 4-1 B shows a time series of cross-shelf current profiles with the depth that show semidiurnal dominance throughout the water column. The red contour indicates onshore currents which flow in the cross-shelf direction (depicted as red dotted line in the Figure 4-1 A). The currents range from $\sim\pm 30$ cm/s and generally decrease with depth due to bottom friction. From Jan. 1 to 3, when semidiurnal variations were diminished by winds, the cross-shelf currents generally flowed offshore. Offshore flows caused water surface heights to decrease. This time period is overlapped with neap tides; the third quarter moon occurred on Dec. 31 in 2007. Due to the weak tidal currents during the neap tide, the currents were more strongly influenced by winds. When the winds blow northward from Dec. 27 to 31 of 2007, the cross-shelf currents through the water column seem to be modulated by the winds. The flood and ebb currents were weakened and strengthened at the bottom respectively so downwelling was expected. Figure 4-1 C shows the along-shelf currents that rarely have tidal currents due to the axis rotation. From Jan. 1 to 3, when the winds over 10 m/s blew southeastward, the along-shelf currents were nearly negative 30 cm/s through the water column. In this period the water seems to be influenced by the tangential pressure exerted by the wind. The along-shelf currents seem to be closely related with the winds.

Time-series of winds, water surface heights and currents in Fall 2008 are given in Figure 4-2. In Figure 4-2 A) the mean wind speed was estimated at 7.7 m/s and the maximum speed occurred at 11:00 on Dec. 11. In this deployment the full moon

occurred on Oct. 14, Nov. 13 and Dec. 12. Figure 4-2 B) shows the fortnightly variation with 4 neap and 5 spring tides. Also the relationship between water surface heights and winds can be recognized. As shown in Deployment 7-1, the water surface height decreased with northerly winds. On Oct. 28 the wind speed exceeded 15 m/s and the water surface height tended to descend. The same phenomenon was observed around Dec. 13. The drop of water surface height can be seen in Figure 5-12 with the low-pass filtered time series.

The contour plot in Figure 4-2 B provides the cross-shelf currents during Deployment 8-1. The cross-shelf currents varied from $\sim\pm 30$ cm/s and also show dominance of semidiurnal currents. Fortnightly variability can be seen from the contour plot. For instance, the current fluctuation around Nov. 13 ranged from around positive 30 to negative 30. The oscillation range of currents during the neap tide, around Nov. 6, was relative small as compared to the spring tide. Figure 4-2 C shows the along-shelf currents which rarely have tidal component due to the axis rotation. It is recognized that the along shelf currents are strongly associated with the wind. The southerly and northerly wind drives the positive and negative along-shelf currents, respectively. The along-shelf currents oscillated at the lower frequency than the cross-shelf currents, which means the along-shelf currents are generally related with the synoptic weather.

Measurements during the summer of 2009 are shown in Figure 4-3. Among the deployments, the Deployment 9-1 is the longest deployment in this study and the cross-shelf exchange flow was also detected in this deployment. The wind data from station SGOF1 were unavailable. Therefore, data from the nearby station 42036 were used to demonstrate the hydrodynamics during the period. The wind directions during

Deployment 9-1 were relatively irregular and the speeds were weak as compared to Deployment 7-1 and 8-1. The strongest wind occurred at 6:20 PM on Aug. 16 of 2009 and the average wind speed during this deployment was approximately 4 m/s.

From Figure 4-3 B, it is recognized that water surface heights were dominated by semidiurnal tidal components. Fortnightly variations were observed in the sea level data changing from 11.1 to 13 m. In this period the fortnightly variability is clearer than Deployment 8-1 because the wind speed was relatively small. The cross- and along-shelf currents varied from around positive 30 to negative 36 cm/s during Deployment 9-1. The cross-shelf currents generally oscillate with semidiurnal frequency but the tidal currents were distorted around the middle of Jun. when the winds blow toward the negative along-shelf direction. However the wind effect on the currents seems to be confined over the surface layer because the bottom layer clearly shows semidiurnal currents during the middle of Jun. At the same time the along-shelf currents also went toward the negative direction as seen in Figure 4-3 C.

This section described the variation of unfiltered winds, water surface heights and currents. The purpose of this study is to understand the processes that govern cross-shelf circulation on wind-driven shelf. However, the wind effects on the currents cannot be clearly recognized because unfiltered current velocities have tidal effects that are major contributors to shelf currents. Therefore, spectral density analysis is described in section 5.1 to estimate the dominant tidal effects on shelf currents. According to the results of spectral density, the measurements are filtered to remove the tidal effects and high frequency effects.

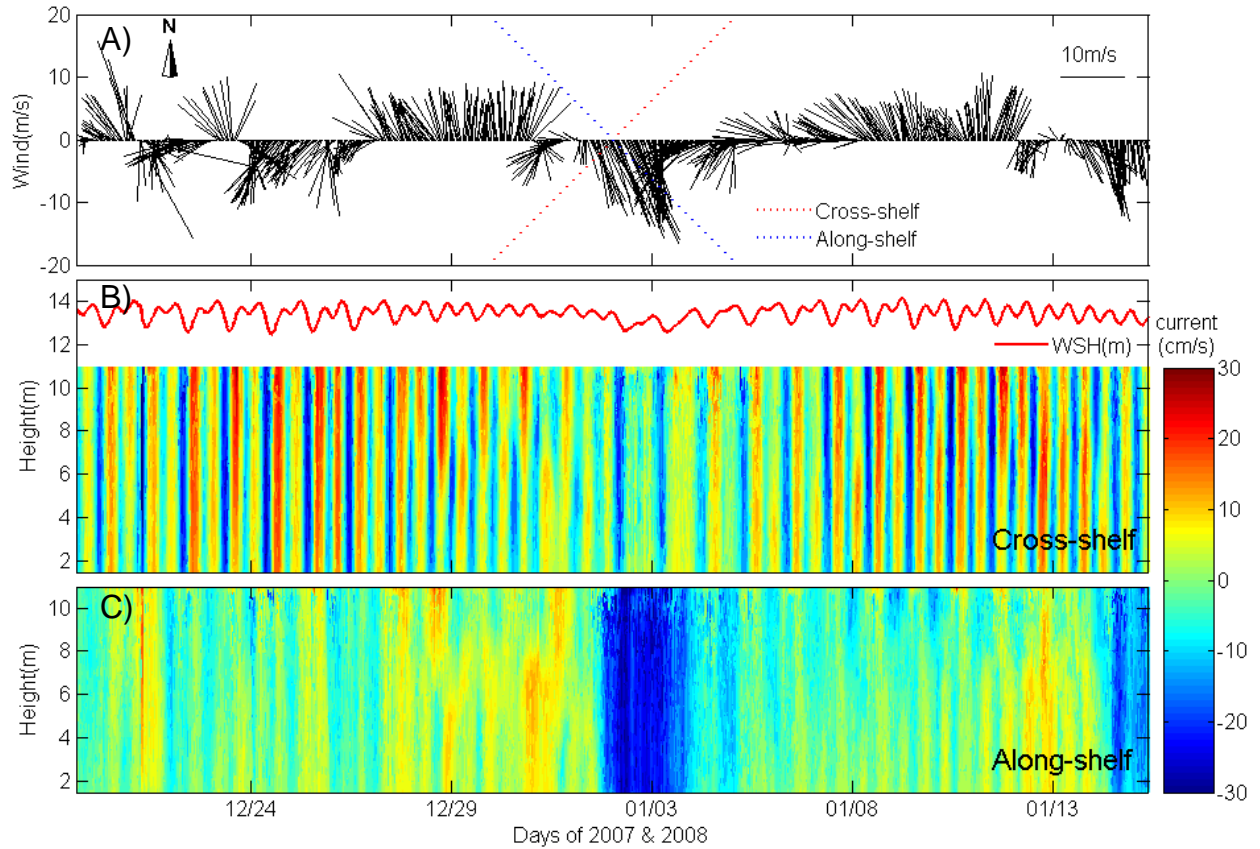


Figure 4-1. During Deployment 7-1 A) wind plot with the direction of cross- and along-shelf direction described by red and blue dotted lines respectively. B) The vertical structure of the cross-shelf currents with water surface heights. C) The vertical structure of the along-shelf currents.

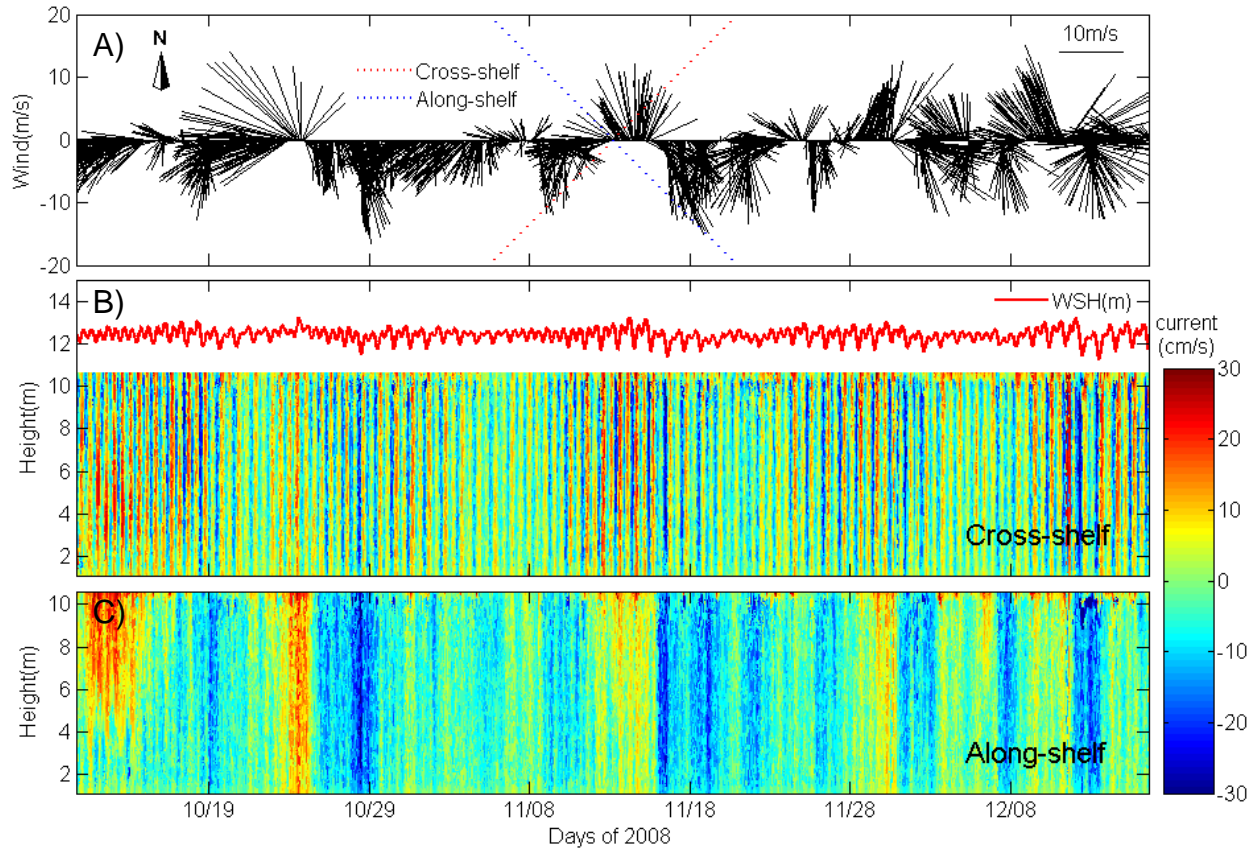


Figure 4-2. During Deployment 8-1 A) wind plot with the direction of cross- and along-shelf direction described by red and blue dotted lines respectively. B) The vertical structure of the cross-shelf currents with water surface heights. C) The vertical structure of the along-shelf currents.

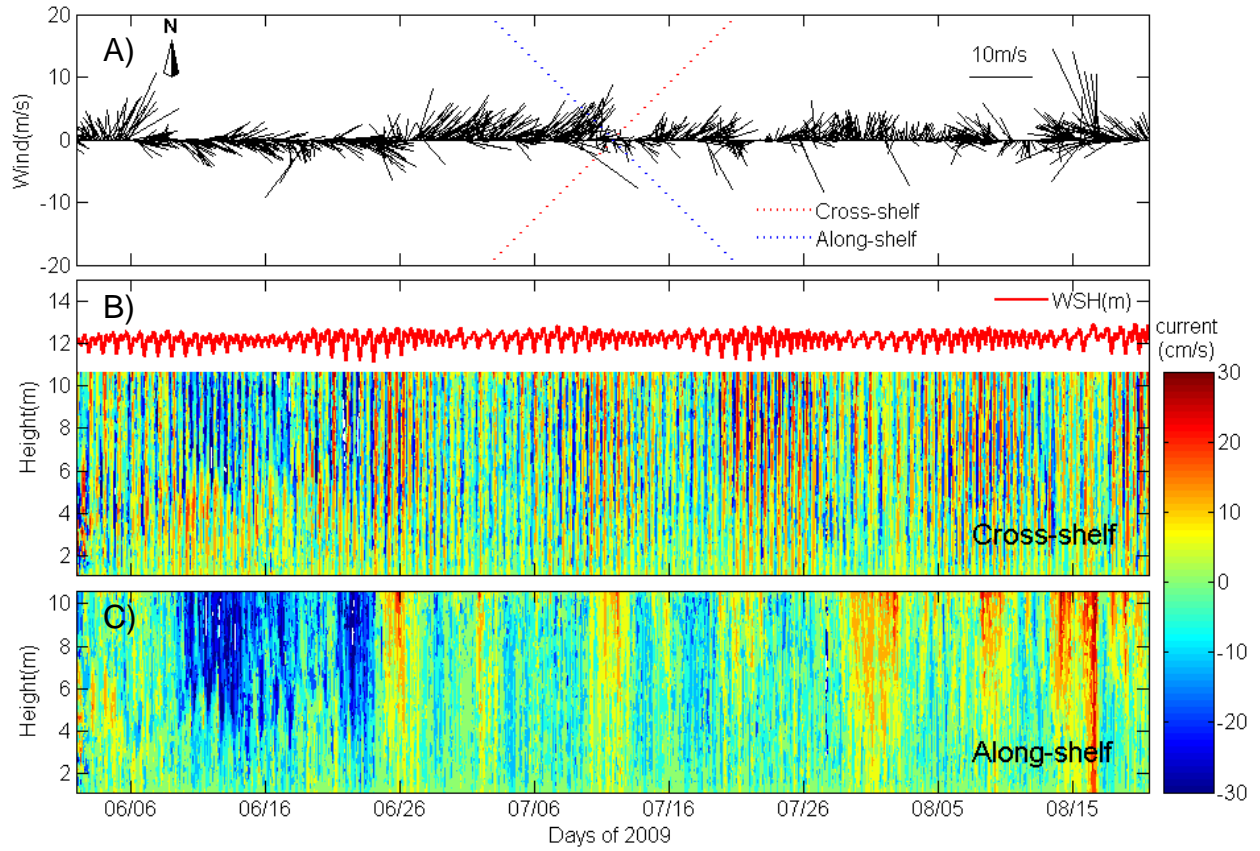


Figure 4-3. During Deployment 9-1 A) wind plot with the direction of cross- and along-shelf direction described by red and blue dotted lines respectively. B) The vertical structure of the cross-shelf currents with water surface heights. C) The vertical structure of the along-shelf currents.

CHAPTER 5 SPECTRUM ANALYSIS AND LOWPASS-FILTERED DATA

5.1 Spectrum Analysis

Spectral density analysis is performed to estimate the dominant frequencies on current and wind velocities. Spectrum density plots for the time-series data described in Chapter 4 are provided in Figure 5-1 through 5-6. East-West and North-South velocity components have diurnal and semi-diurnal contributions that lose energy with depth due to bottom friction as shown in Figure. 5-1 A. The diurnal components also include the inertial motion of which the period can be calculated by

$$T_i = 2\pi/f \quad (5-1)$$

where f is the Coriolis parameter. Therefore the period of inertial motion at the latitude $29^{\circ}27.91'N$ where the ADCP was deployed (Figure 2.1) is 24.33 hours which is close to the O1 and K1 periods of 25.82 and 23.93 hr, respectively. He and Weisberg (2002) mentioned that semidiurnal tides indeed appear to be barotropic tide the amplitude and orientation would be independent on depth. In contrast, the inertial motion most likely influences diurnal tides. As a result, the vertical structure of diurnal tides was observed especially in deeper water as baroclinic modes with the orientation reversals seen in the deeper layer.

With the 45° axis rotation to align with the principal axis (Figure 5-1 B) the semidiurnal and diurnal tidal variability is transferred to the cross-shelf velocities. On the other hand, the low frequency variability is transmitted to the along-shelf direction. This means that along-shelf currents are associated with synoptic or longer scale variability related to meteorological forcing. In general, the spectral densities lost energy with

depth and the diurnal energy of along-shelf currents rarely reached the bottom. The increased diurnal variability at the water surface was likely triggered by a sea breeze.

The spectral density of winds collected from SGOF1 is shown in Figure 5-2. Like the currents, the wind spectral density is given for non-rotated records in Figure 5-2 A and for shelf-aligned coordinates in Figure 5-2 B, respectively. Without the axis rotation the spectral density of the North-South wind component shows highest energies at low frequencies, which means that synoptic scale winds blow dominantly toward the North or South. Figure 5-2 B shows the wind spectral density for the shelf-aligned coordinate system. With the rotation, the spectral density of the North-South direction slightly moves to the cross-shelf direction. In Figure 5-1 B the along-shelf currents dominate the cross-shelf currents at low frequencies. This trend is also shown in Figure 5-2 B, that is, the along-shelf winds are dominant at low frequencies. The along-shelf currents mostly corresponds to the synoptic scale wind during Deployment 7-1.

The spectral density of currents that were measured in fall through winter is shown in Figure 5-3. In the comparison between Figure 5-3 A and B, it is also shown that the diurnal and semidiurnal energies were indeed transferred to the cross-shelf direction with the 45° axis rotation. The diurnal energies on the cross-shelf flow component in Figure 5-3 B are weak compared to Figure 5-1 B, which means the diurnal currents during Deployment 8-1 were weaker than during Deployment 7-1. The low frequency energies in the along-shelf component are also smaller during Deployment 8-1 than 7-1. Relatively weaker currents in Deployment 8-1 are caused by the relatively weaker synoptic- scale wind stresses. Like in Deployment 7-1 the synoptic scale wind stresses play an important role in along-shelf currents.

As shown in Figure 5-1 and 5-3, the tidal energies are transferred to the cross-shelf direction and the low frequency energies are transmitted to the along-shelf direction with 45° axis rotation. Figure 5-5 shows the spectral density of currents measured in summer. The diurnal and low frequency energies decrease with depth more evidently than in Deployment 7-1 in winter and 8-1 in fall. This is especially apparent in the spectral density of diurnal motions in the cross- and along-shelf direction, as the signal does not reach the bottom (Figure 5-5 B). The energies are mainly concentrated on the semidiurnal constituents in the cross-shelf direction.

The semidiurnal tides (M2) in the WFS are barotropic according to previous investigations, as Koblinsky (1981) and He and Weisberg (2002). Therefore the semidiurnal oscillations change barely with depth, as shown in Figure 5-1 B, 5-3 B and 5-5 B, regardless of the seasons: winter, fall and summer. However, the diurnal vertical structure is evidently influenced by the seasonally varying stratification. The stratification in summer (Deployment 9-1) can induce internal tides and decouple inertial motions at the surface from the frictional effects at the bottom, which makes the diurnal ellipses random and nearly circular (Weisberg et al., 1996). Therefore the vertical structure of currents tends to reduce the diurnal energy at the bottom as shown in Figure 5-5 B. Unlike the winds of Deployment 7-1 and 8-1, the spectral density of cross-shelf winds at low frequencies is larger than that of along-shelf winds. The spectral density of along-shelf currents is still larger than that of cross-shelf currents at low frequencies. This implies that the cross-shelf winds play an important role in the along-shelf currents during Deployment 9-1.

To evaluate the propagation of the tidal (and other period) current signal in the water column, Rotary Spectral Density (RSD, $(\text{cm/s})^2/\text{cpd}$ (cycle per day)) is estimated as shown in Figure 5-7, 5-8 and 5-9. The RSD at positive and negative frequencies depicts the strength of horizontal currents rotating in counter-clockwise and clockwise direction, respectively. The inertial period generated by the Earth's rotation is nearly aligned with the diurnal cycle because the currents are measured at a latitude of $\sim 30^\circ$. Therefore, the RSD at negative diurnal frequency likely depicts inertial motion.

In three deployments the semidiurnal signal of the RSD is stronger for the positive frequency than for the negative frequency. This implies that the semidiurnal currents primarily propagate counter-clockwise. The counter-clockwise rotation of the M2 and S2 constituents on the WFS was discussed by both Reid and Whitaker (1981) and He and Weisberg (2002). Reid and Whitaker (1981) considered the counter-clockwise motion to be induced by a gravest mode edge wave (Kajiura, 1958). Using in situ measurements and three-dimensional numerical simulations He and Weisberg (2002) described the principal semidiurnal (M2 and S2) and diurnal (K1 and O1) components over the WFS. They found that the phase of the M2 tide proceeds toward the northwest and the similarity between the isobaths and the co-amplitude plots for semidiurnal tides exists in the Florida Big Bend. The larger seasonal modulation is also observed in the diurnal components as mentioned in the spectral density analysis shown in Figure 5-1 and 5-3. At both positive and negative frequencies the diurnal energies seen in the winter (Figure 5-7) are relatively large compared to the diurnal energies seen in the summer (Figure 5-9). The inertial oscillations under stratified

conditions tend to cancel out when performing vertical averages (He and Weisberg, 2002) because the orientation of baroclinic modes are reversed in the deeper layer.

5.2 Low-Pass Filtered Wind and Current Velocities

Continental shelf circulation provides a pathway for mass property and nutrient exchange which can have an important effect on the ocean system. Observations in winter, fall and summer are presented for the analysis of the transport processes over the West Florida Shelf. Wind and current time-series are low-pass filtered to obtain only periods longer than 25 hours as shown in Figure 5-10, 5-11 and 5-12. The low-pass filtered data provide an interpretation of the associated dynamics characterizing the vertical structure of currents and evaluate the important physical processes affecting the circulation.

Figure 5-10 A shows the low-pass filtered wind velocity variables, that is, high frequency winds such as sea breezes are removed from the original data. The low-pass filtered winds primarily blow northerly or southerly. The strongest wind speed of low frequency is 13.6 m/s on Jan. 2, 2008 and the mean wind speed is 5.8 m/s. In Figure 5-10 B water surface height was almost stable except the period when the strong northerly winds occurred from Jan. 1 to 3. In this period the sea level fell at the mooring location, which means upwelling likely occurred. The mean WSH of low frequency is 13.4 m and the lowest WSH was recorded as 12.9 m around Jan. 3.

The cross- and along-shelf currents in Figure 5-10 B and C ranged from +6 to -6 cm/s and from +10 to -30 cm/s respectively. The solid black line represents the zero interfaces of currents in each contour plot. The subtidal flows tend to be strongly polarized in the along-shelf direction due to the constraint on cross-shelf flows imposed by the coastal boundary and the reduction in water depth. The vertical structure of the

along-shelf currents is more uniformly distributed. The cross-shelf exchange flows appeared when the winds blew northward as shown in Figure 5-10 B. The southerly winds tend to cause downwelling over WFS. When the winds blew northward from Dec. 27 to 31 and from Jan. 11 to 13, the near surface flow was directed onshore and near bottom flow was directed offshore. The temporal variation of along-shelf velocities was relatively large and the velocity profiles are primarily uniform with depth, which means that the frictional influence from the bottom were weak.

In Figure 5-11 the wind velocity is plotted along with current velocity at: 1.5, 2.5, 3.5, 4.5, 5.5, 7, 8, 9, 10 and 11 m from the bottom. To see the relation between winds and currents, all vector plots were drawn with respect to the true north, which is denoted on the top-left side of the wind plot. As shown in Figure 5-10, the cross-shelf exchange flow is observed in the period when winds blow from around true north (i.e., Dec. 27 to 31). In this period the currents flows to the right of the wind direction in the surface layers: 9, 10, and 11 m. At 8 m height the current direction nearly corresponds with the wind direction. The currents are directed to the left of the wind direction at the other layers (below 8 m height). This demonstrates that downwelling occurred when the wind blew toward the north. However, the strong winds that occurred around Jan. 3 and 15 drive the currents to nearly flow downwind throughout the water column.

Figure 5-12 shows data from another deployment when cross-shelf exchange flows were detected. Although two-layer flows cannot be seen with the low-pass filtered data, they can be observed with EOF methods described in section 3.2. The mean low frequency during Deployment 8-1 was recorded as 6.7 m/s. The strongest wind around 13.7 m/s occurred on Oct. 23 in 2008. Unlike Deployment 7-1 the wind direction varied

in every direction. The low-pass filtered WSH gently varied from 12.7 m to 12.1 m. The mean value of the low-pass filtered WSH is around 12.4 m. A downwelling favorable along-shelf wind (southerly wind) drives onshore flow near the surface. Due to the constraint on the onshore imposed by the coastal boundary and the reduction in water depth, the onshore transport converged near coast. This causes sea level to rise toward the coast and the compensating return flow in the bottom boundary layer. Therefore, the water surface height near coast tends to increase with southerly wind but to decrease with the northerly wind as shown in Figure 5-12 B.

The low-pass filtered cross- and along-shelf currents during Deployment 8-1 are provided in Figure 5-12 B and C, respectively. The cross-shelf currents of low frequency range from +6 to -6 cm/s. Like Deployment 7-1 the subtidal flow is polarized along-isobath, that is, the variability of the subtidal along-shelf current is from +10 to -24 cm/s. From the contour in Figure 5-12 B the wind from the south generated downwelling around Nov. 29, Dec. 6 and 9. At the beginning of the measurements the winds were directed toward the negative cross-shelf direction and as a result, upwelling was observed. In this period vertically sheared flow was also detected in the along-shelf flow as shown in Figure 5-12 C. The vector plots in Figure 5-13 give the wind velocity along with current velocities at 10 bins: 1.1, 2.1, 3.1, 4.1, 5.1, 6.6, 7.6, 8.6, 9.6 and 10.6. The surface layer flow is interestingly directed to the left of the wind direction. The direction and magnitude of the currents throughout the water depth barely changed in this measurement period. This is because the currents are mostly directed along-isobath where the bottom friction has little effect on the currents.

Figure 5-14 gives the time series of winds and currents collected during Deployment 9-1. The low-pass filtered winds in this deployment were weaker than the winds of the other two deployments given in this section, as shown in Figure 5-14 A. The mean wind velocity was 3.3 m/s and was small compared with 5.8 m/s winds measured in winter and 6.7 m/s collected in the fall. The fastest wind, 7.5 m/s, occurred on Aug. 16 and was directed to the northwest. During Deployment 9-1 the wind generally blew toward the north, which corresponds with the result from Weisberg et al. (2005). They addressed that drifters released in summer returned from points farther north, while those released in winter generally returned from points farther south. The mean of low-pass filtered WSH was 12.1 m. Due to the weak wind stress in this deployment the low-pass filtered water surface height was relatively stable compared to the other deployments.

The low-pass filtered cross-shelf flow in Figure 5-14 B varied from +4 cm/s to -15 cm/s. Compared with Deployment 7-1 and 8-1, the strong negative cross-shelf flow occurred on the surface layer from Jun 6 through 24. In this period the cross-shelf two-layer flow is clearly detected and upwelling occurred. The currents are also arranged along-isobath. The low-pass filtered along shelf currents range from +10 to -20 cm/s. Unlike Deployment 7-1, the along-shelf currents are not uniformly distributed with depth. The vertical along-shelf distribution with depth largely shows a logarithmic variation. This was caused by effects of bottom friction.

The vector plots in Figure 5-15 show wind velocities along with current velocities at the following heights above the bottom: 1.1, 2.1, 3.1, 4.1, 5.1, 6.6, 7.6, 8.6, 9.6 and 10.6 m, respectively. The currents on the surface veered around 30° to the right of the

wind direction, when cross-shelf exchange flow is observed. This implies the Coriolis force mainly affected currents on the surface of the water column. The boundary layer of thickness δ_E is equal to $\sqrt{2A/f}$ for a constant eddy viscosity A (Ekman 1905), or proportional to u_* / f where u_* is the stress velocity ($u_* = \sqrt{\tau/\rho_0}$) for a turbulent, unstratified flow (Csanady 1967; Gill 1968). The thickness of the surface and bottom boundary layer can vary in time depending on the strength of the wind and wave forcing and vertical density stratification (Lentz and Fewings, 2012). Hence, the 30° change of current direction with respect to the wind shows the surface and bottom boundary in the inner shelf minimally interacts with the weak wind velocities. The surface boundary layer during Deployment 9-1 is relatively thin due to the weak wind stresses. Although the wind variability is smaller than Deployment 7-1 and 8-1, the variation of currents is almost identical. This implies that the inner shelf boundary moved to the shore in this deployment.

The purpose of this study is to understand velocities on a wind-driven shelf. Lentz (2001) mentioned that the depth-averaged cross-shelf currents are uncorrelated both with the wind stress and between mooring sites. Dever (1997) discussed how the interior and bottom mixed layer transport are uncorrelated with local wind forcing. To focus on the depth- dependent cross-shelf circulation they subtracted the depth-averaged cross-shelf current from the cross-shelf current at each depth. The removal of the depth-averaged cross-shelf velocity results in an increased correlation of interior and bottom boundary layer transport with the wind stress (Dever, 1997; Lentz, 2001). However, the correlation coefficient between the depth-averaged cross-shelf velocity and along-shelf wind stress τ_y is 0.61, 0.83 and 0.73 during Deployment 7-1, 8-1 and 9-

1 respectively. There rarely exists an interior region between surface and bottom boundary layers around 13 m depth. Hence, the depth-averaged cross-shelf current were not subtracted from the cross-shelf currents in this study. EOF methods separate the unidirectional cross-shelf currents which indeed correspond to the depth-averaged cross-shelf currents from low-pass filtered cross-shelf currents. The relationship between winds and the unidirectional cross-shelf current is shown in the next chapter.

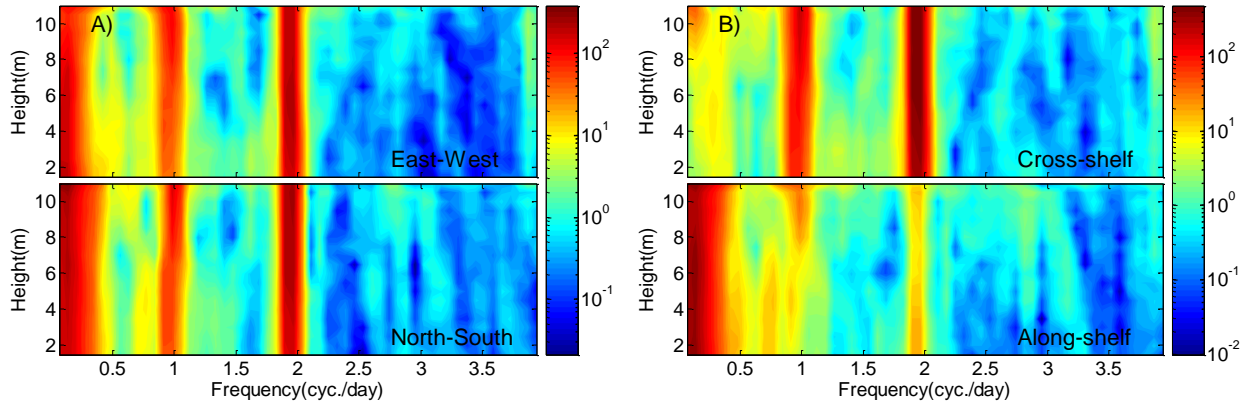


Figure 5-1 Vertical spectrum density $((\text{cm/s})^2/\text{cpd})$ distribution of A) East-West and North-South currents without axis rotation and B) cross- and along-shelf currents with 45° axis rotation during Deployment 7-1.

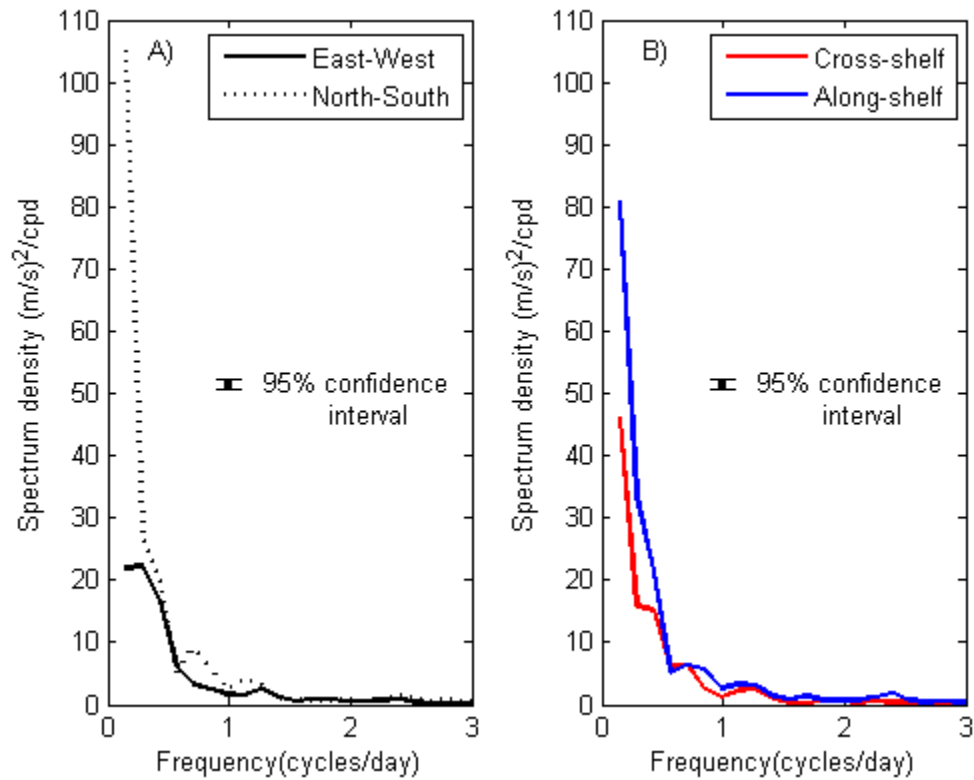


Figure 5-2. Spectrum density $((\text{m/s})^2/\text{cpd})$ of A) East-West and North-South winds without axis rotation and B) cross- and along-shelf winds with 45° axis rotation during Deployment 7-1.

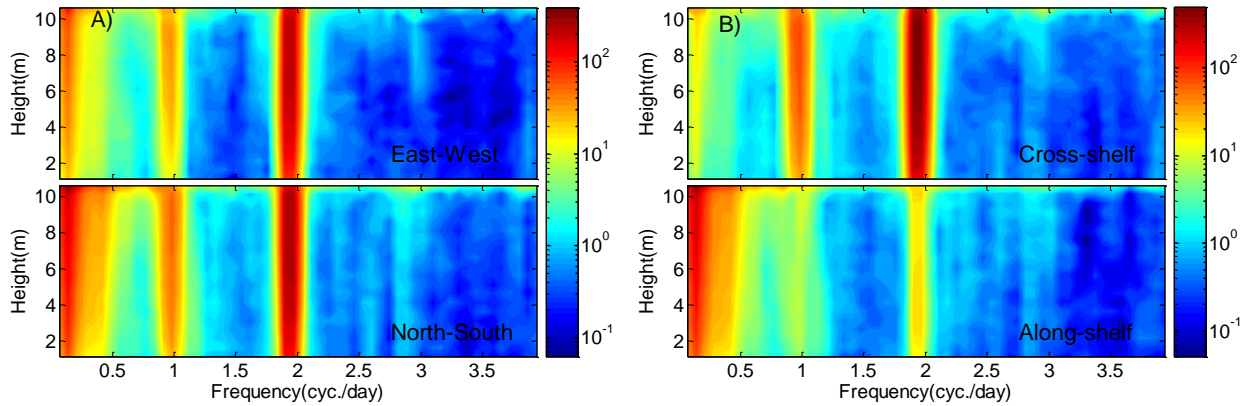


Figure 5-3. Vertical spectrum density $((\text{cm/s})^2/\text{cpd})$ distribution of A) East-West and North-South currents without axis rotation and B) cross- and along-shelf currents with 45° axis rotation during Deployment 8-1.

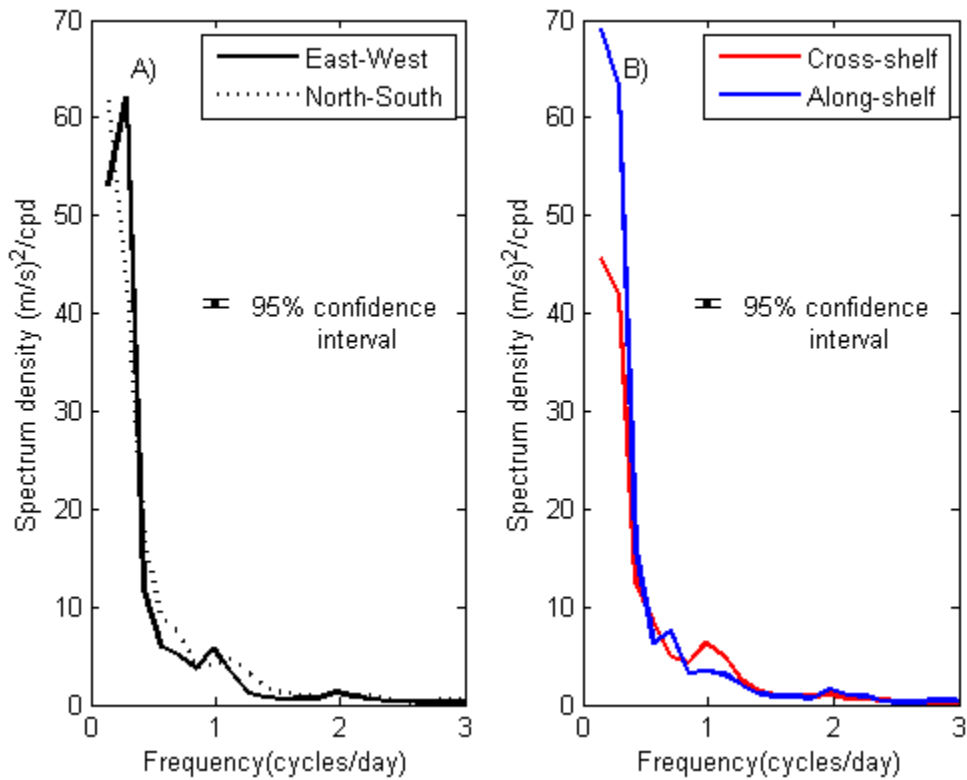


Figure 5-4. Spectrum density $((\text{m/s})^2/\text{cpd})$ of A) East-West and North-South winds without axis rotation and B) cross- and along-shelf winds with 45° axis rotation during Deployment 8-1.

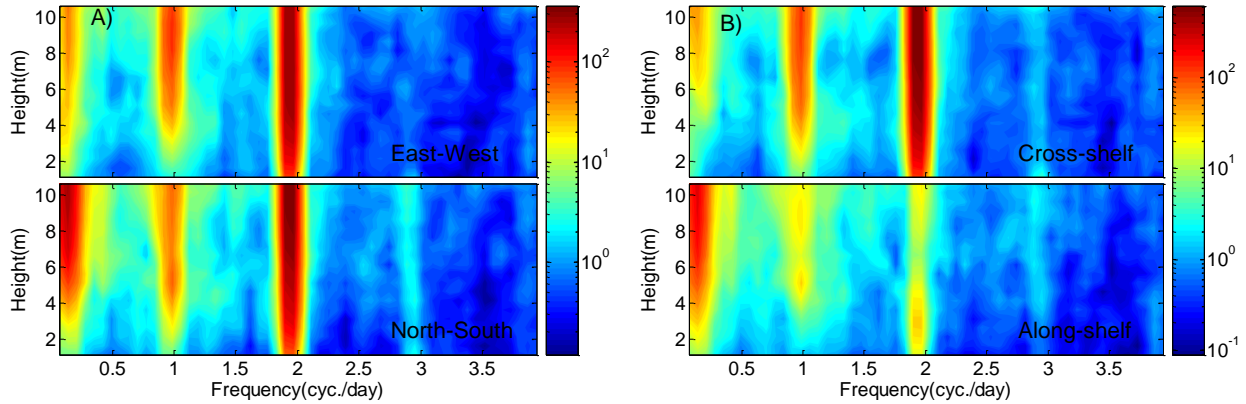


Figure 5-5. Vertical spectrum density $((\text{cm/s})^2/\text{cpd})$ distribution of A) East-West and North-South currents without axis rotation and B) cross- and along-shelf currents with 45° axis rotation during Deployment 9-1.

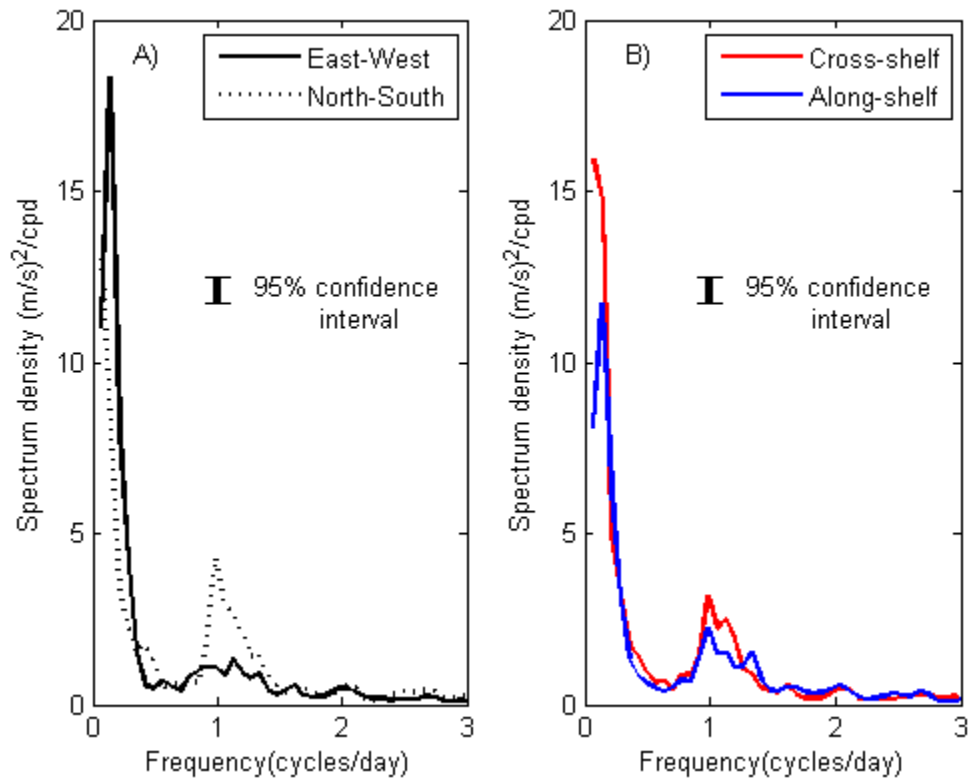


Figure 5-6. Spectrum density $((\text{m/s})^2/\text{cpd})$ of A) East-West and North-South winds without axis rotation and B) cross- and along-shelf winds with 45° axis rotation during Deployment 9-1.

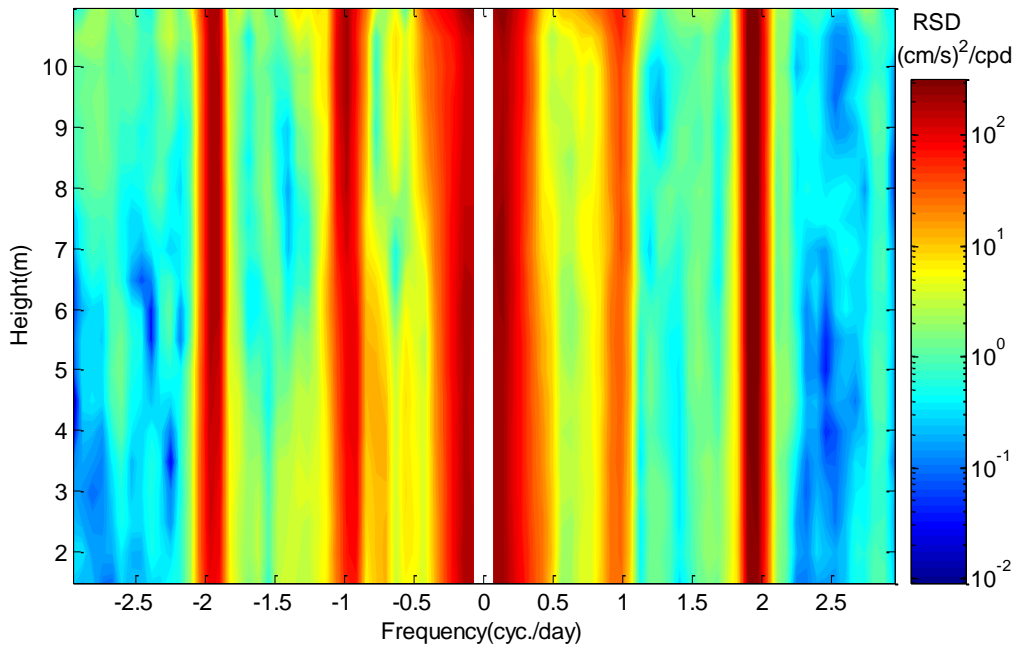


Figure 5-7. The vertical distribution of RSD ((cm/s)²/cpd) for counter-clockwise rotation at (+) frequencies and clockwise rotation at (-) frequencies during Deployment 7-1.

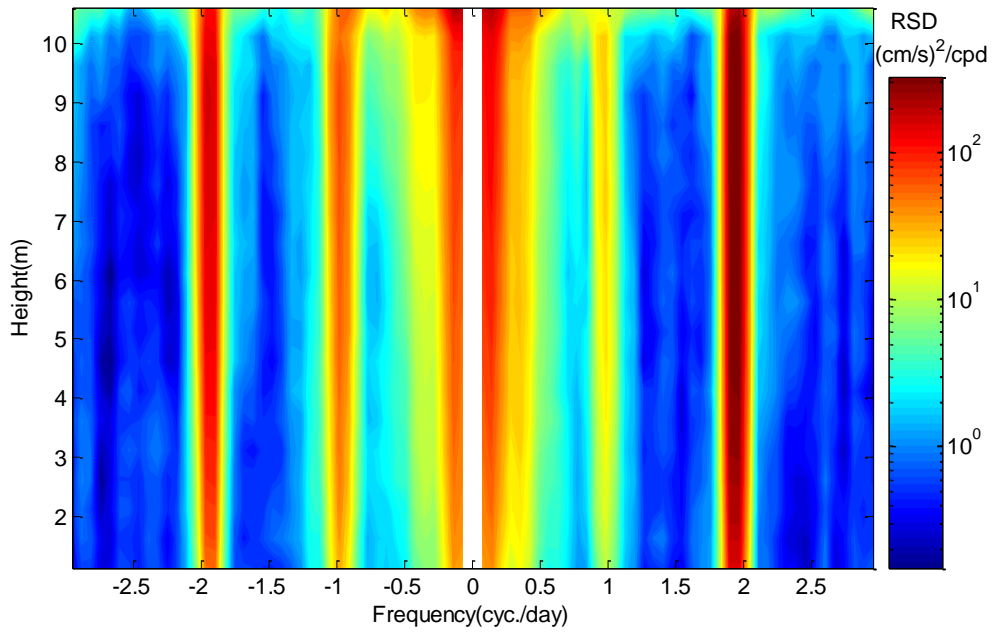


Figure 5-8. The vertical distribution of RSD ((cm/s)²/cpd) for counter-clockwise rotation at (+) frequencies and clockwise rotation at (-) frequencies during Deployment 8-1.

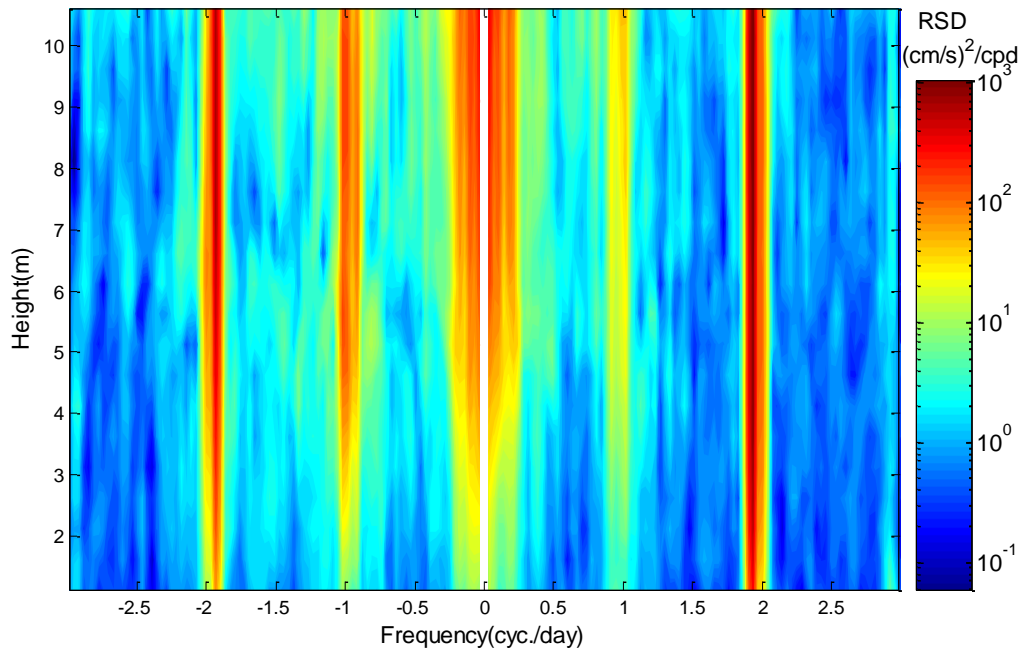


Figure 5-9. The vertical distribution of RSD ((cm/s)²/cpd) for counter-clockwise rotation at (+) frequencies and clockwise rotation at (-) frequencies during Deployment 9-1.

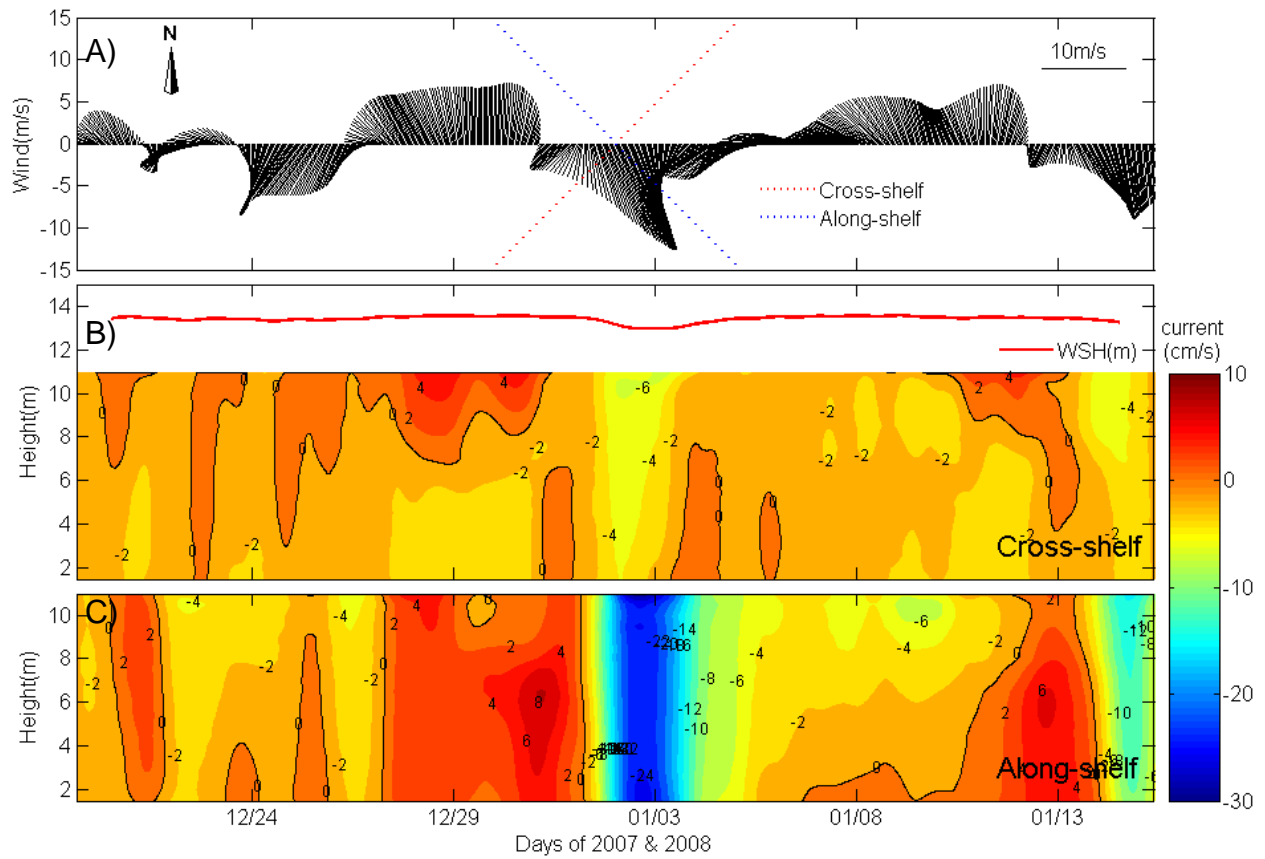


Figure 5-10. During Deployment 7-1 A) low-pass filtered wind plot. B) The vertical structures of low-pass filtered cross-shelf velocities with low-pass filtered water surface heights. C) The vertical structures of low-pass filtered along-shelf velocities.

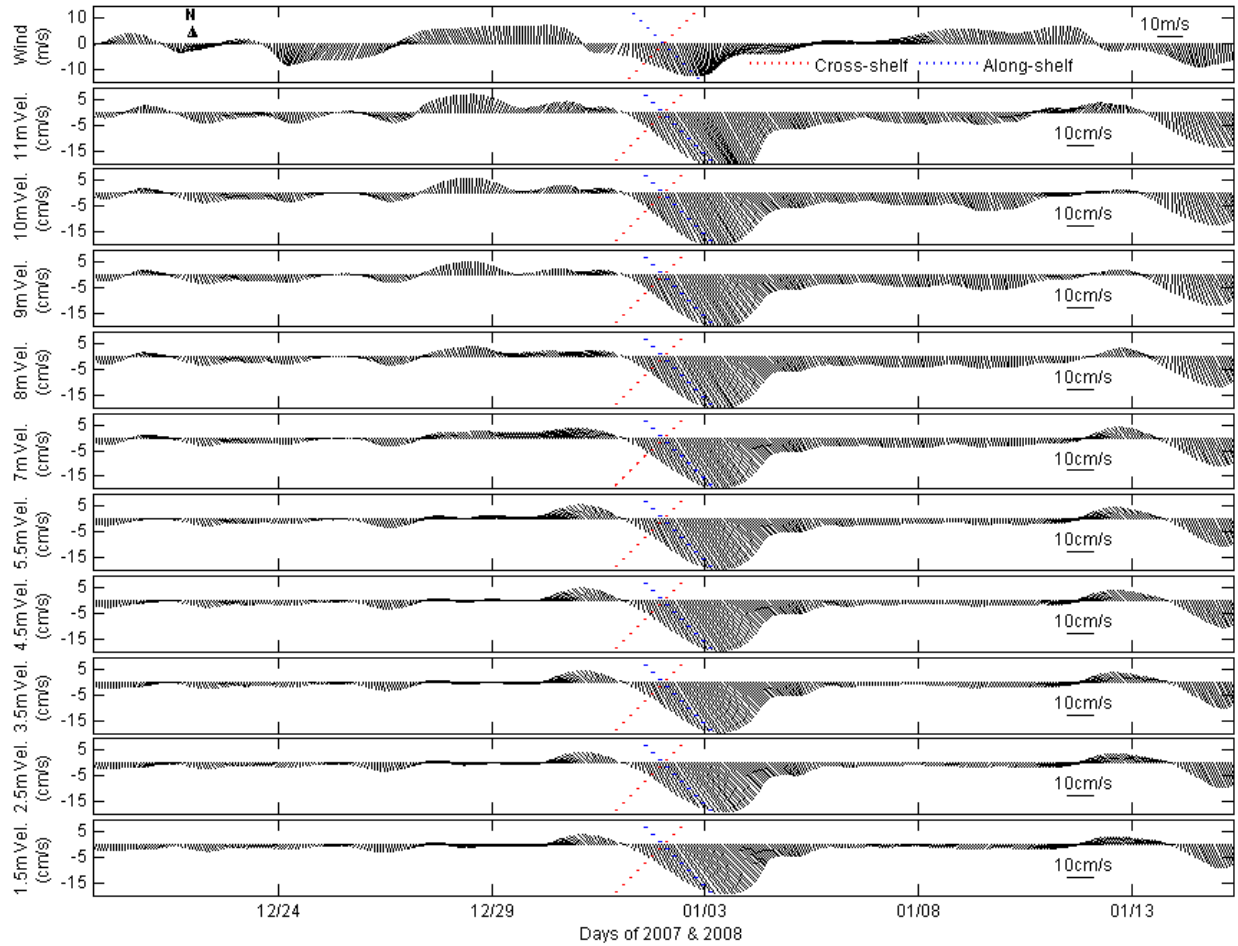


Figure 5-11. Time series of lowpass-filtered wind velocity (m/s), and horizontal current velocity (cm/s) at the heights: 1.5, 2.5, 3.5, 4.5, 5.5, 7, 8, 9, 10 and 11 m above the bottom, during Deployment 7-1.

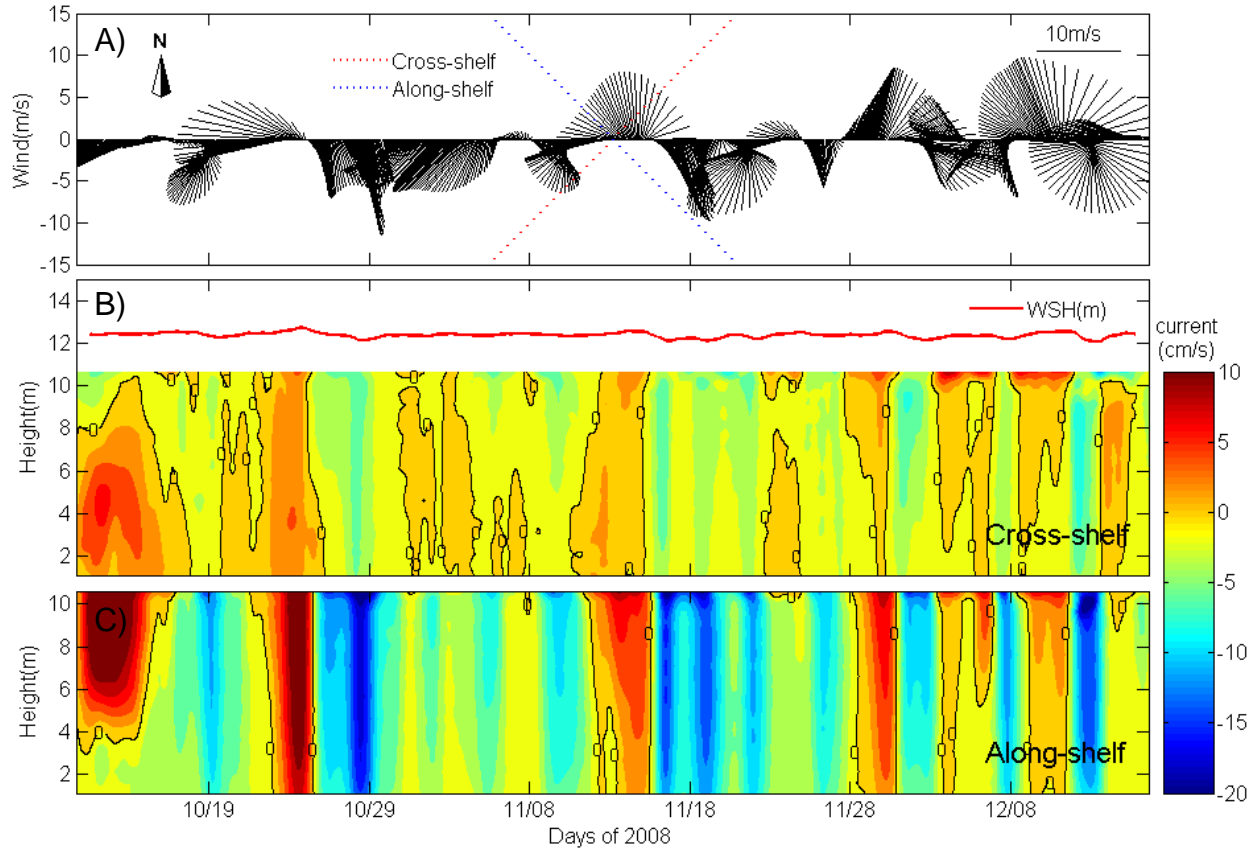


Figure 5-12. During Deployment 8-1 A) low-pass filtered wind plot. B) The vertical structures of low-pass filtered cross-shelf velocities with low-pass filtered water surface heights. C) The vertical structures of low-pass filtered along-shelf velocities.

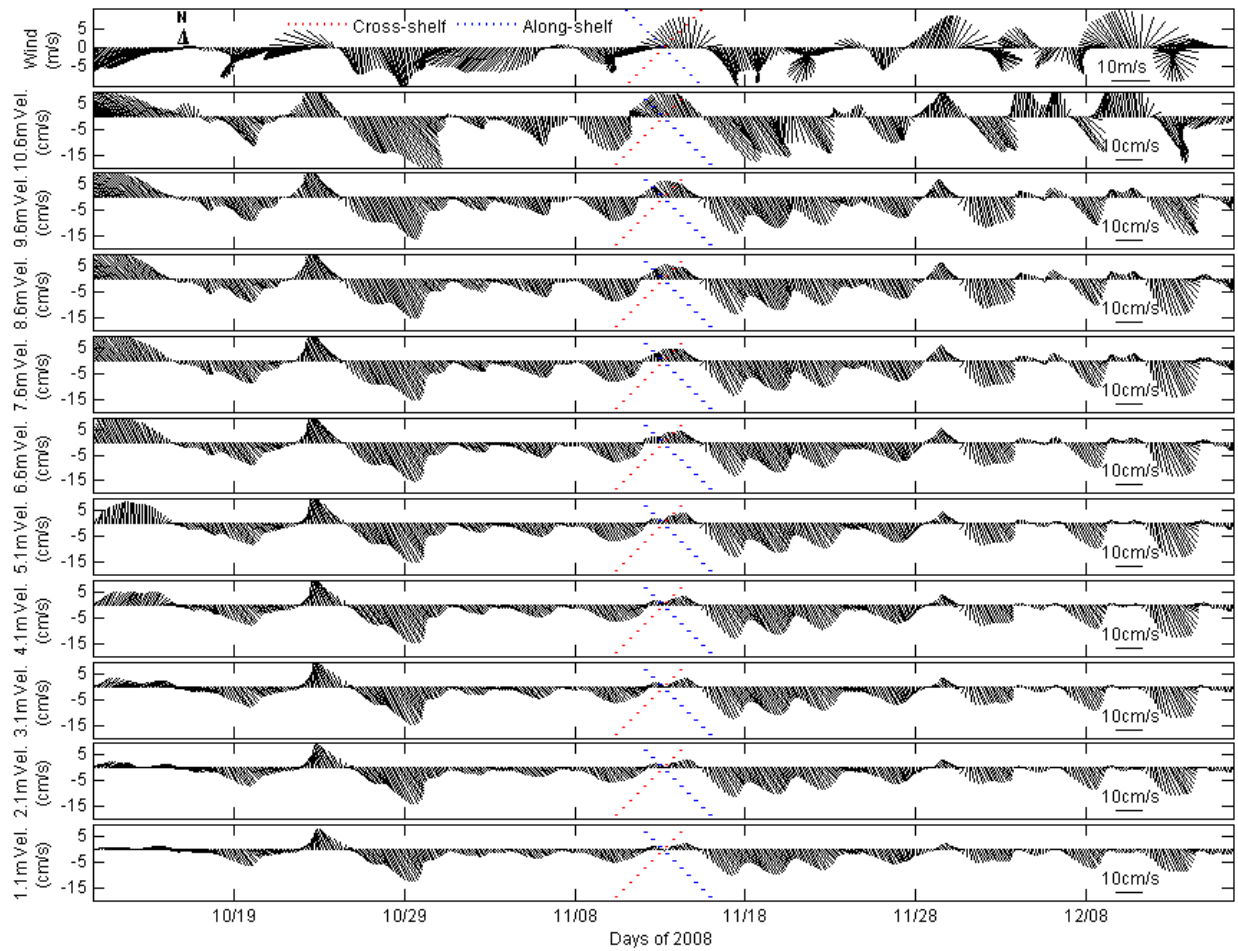


Figure 5-13. Time series of lowpass-filtered wind velocity (m/s), and horizontal current velocity (cm/s) at the heights: 1.1, 2.1, 3.1, 4.1, 5.1, 6.6, 7.6, 8.6, 9.6, 10.6 m above the bottom, during Deployment 8-1.

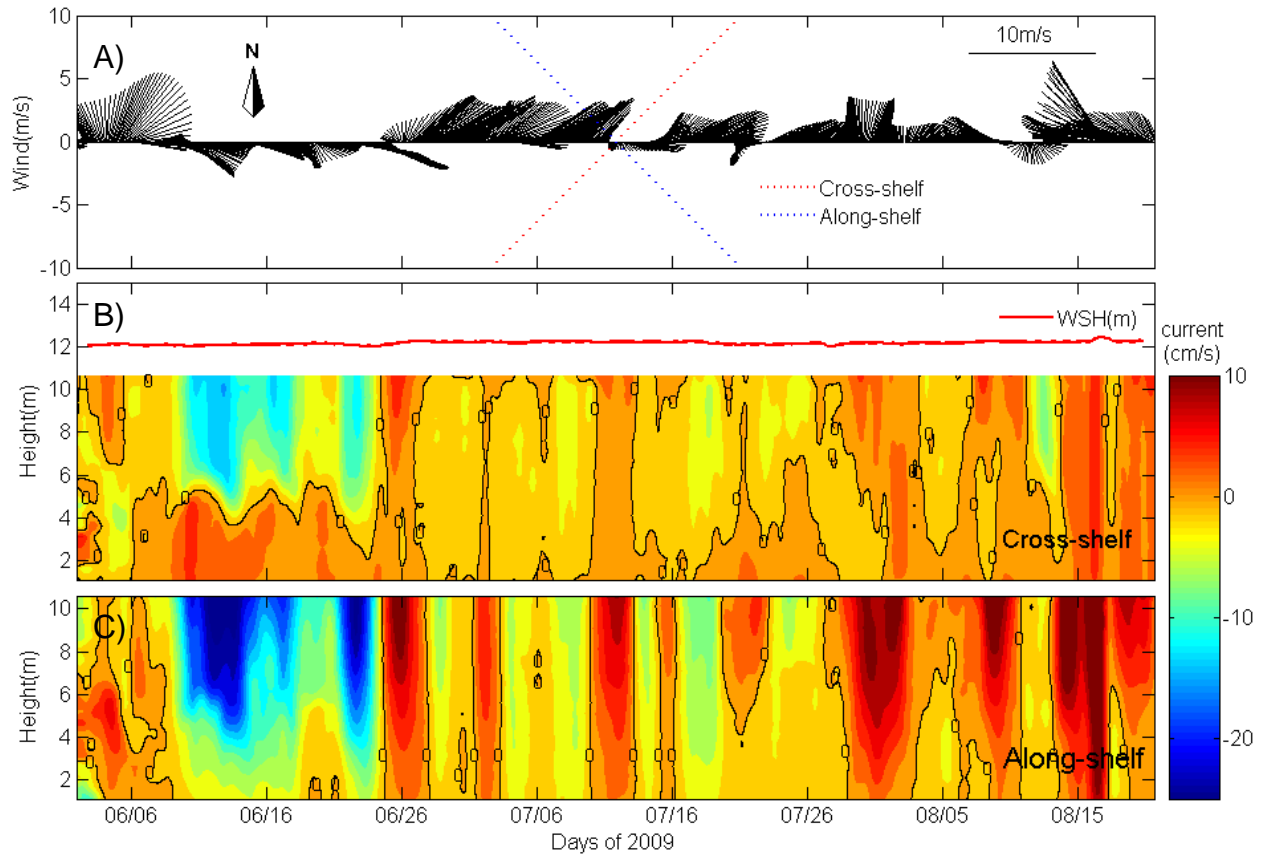


Figure 5-14. During Deployment 9-1 A) low-pass filtered wind plot. B) The vertical structures of low-pass filtered cross-shelf velocities with low-pass filtered water surface heights. C) The vertical structures of low-pass filtered along-shelf velocities

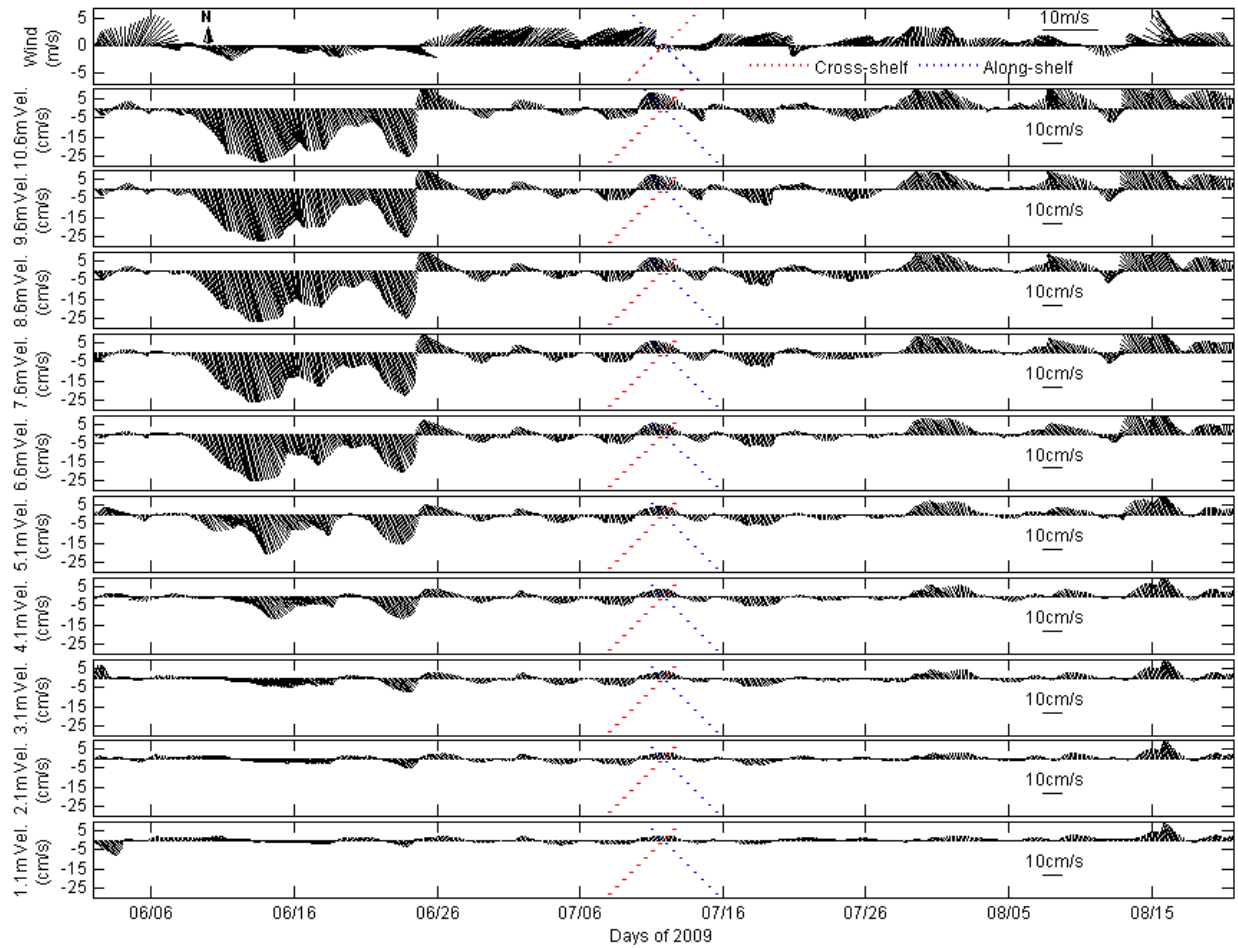


Figure 5-15. Time series of lowpass-filtered wind velocity (m/s), and horizontal current velocity (cm/s) at the heights: 1.1, 2.1, 3.1, 4.1, 5.1, 6.6, 7.6, 8.6, 9.6, 10.5 m above the bottom, during Deployment 9-1.

CHAPTER 6 COMPARISON BETWEEN EOF ANALYSES

Given any space-time data set, the EOF analysis finds a group of statistically orthogonal spatial patterns along with a set of associated uncorrelated time series (Hannachi et al., 2007). To achieve a decomposition of a continuous space-time field, four different EOF methods are applied: straight EOF, Hilbert Transform EOF (HEOF), Complex EOF (CEOF), Concatenated Hilbert EOF (CHEOF). These EOF methods are applied to the cross- and along-shelf currents during Deployment 7-1.

6.1 Deployment 7-1

The comparison of those 4 analyses is shown in Figure 6-1, 6-2 and 6-3, using the time series of along- and cross-shelf currents collected in Deployment 7-1. The first two leading modes of cross-shelf currents are given in Figure 6-1 and 6-2 for the four EOF methods. The shelf-aligned wind magnitude is given in Figure 6-1 A to compare with the first and second mode of cross-shelf currents that is decomposed by both the EOF and HEOF method. The first EOF mode currents in Figure 6-1 B exhibit essentially unidirectional vertical structure. The mode steeply increases near the surface, especially when wind forcing increases. As shown in Figure 6-1 C, the interface between positive and negative velocity for mode 2 is flat and abrupt because the conventional EOF analysis can only detect “stationary” patterns (Hannachi et al., 2007). As explained in section 3.2.2, EOF can detect the stationary patterns that are in phase or π (or 180°) out of phase over the array. Hence, the time series of currents in the top and bottom area split by the zero horizontal contour have no phase lag. The top and bottom current in Figure 6-1 C is clearly 180° phase shifted, that is, the currents (according to EOF analysis) flow instantaneously in opposite direction above and below

the zero contour line. In reality there should be a phase progression in time, i.e., the interface (zero contour) should have a slope instead of being flat. Table 6-3 provides the variance of the first three leading modes that represent the energy of each Principal Component (PC). The first two EOFs capture ~ 95% of the variability of cross-shelf currents during Deployment 7-1 and the energy of the first mode is two times as much as that of the second mode.

Figure 6-1 D and E show the results of HEOF analysis that can capture a propagating structure in a time series. Compared with the EOF analysis, the zero interface of currents is sloped and varies in time, consistent with the time series of currents throughout the water column. The currents in HEOF1 mode generally flow in the same direction above ~2.5 m height from the bottom. As seen in Figure 6-1 B), the vertical distribution of the current shows abrupt variability at the surface layer especially while strong wind occurs, which means the wind is more effective in the top layer. The second mode of HEOF shows the exchange currents that represent upwelling or downwelling (just like in the plain EOF). The variance of the first and second mode is 63.7% and 31.9%, respectively. These first two leading modes together explain ~ 96% of the variation of cross-shelf currents, which is almost the same as the results from the standard EOF analysis.

EOF and HEOFs were applied separately to the components (u, v) of the current field, i.e. the individual components of the ocean current fields were analyzed separately. In contrast, CEOF analysis uses a vector field and forms complex scalars from the u, v components (Kundu and Allen, 1976). This method is widely used in oceanography and meteorology in particular for wind and current vectors. Also, HEOFs can be extended to

vector fields i.e. two or more fields, through concatenation of the respective complex field (Barnett, 1983), which is referred to as CHEOF in this study.

The results of CEOF and CHEOF analysis are given in Figure 6-2. Mode 1 of the CEOF analysis shown in Figure 6-2 B primarily flow in the same direction as in the EOF and HEOF analysis, but does not show the drastic variation at the top layer. The variance explained by the first mode is 62.4%, which is almost identical to that explained by EOF and HEOF. The second mode displays a two-layer structure, as seen in Figure 6-2 C, but the zero velocity contour is found deeper in the water column when compared to the second mode of the EOF and HEOF. The first two leading modes account for 96% of the variability of cross-shelf currents.

The vertical distribution of the CHEOF1 and 2 modes is given in Figure 6-2 D and E. The CHEOF1 mode of cross-shelf currents changed less with time than with the other EOF applications. The variance explained by CHEOF1 is 43.3% which is relatively small. The concatenation of data generates double spatial modes so that the energy can be widely distributed into those spatial structures. The second mode of cross-shelf currents in Figure 6-2 E displays exchange flow. The horizontal velocity generally is in the opposite direction at the 7m height relative to the sea bottom, in a similar fashion to the CEOF2 case. The variance of the second mode is around 31% for the four EOF methods. However, the explained variance of approximately 74% for the combination of the first two modes using the CHEOF method is smaller than the other methods given in Table 6-3. The mode 3 of the CHEOF contributes 19.5% to the variance, which describes cross-shelf currents. This mode 3 clearly displays a vertically linear

distribution, which may be related with other forces. However, there is not enough data available to link this mode 3 to a physical phenomenon.

The vertical profile of cross-shelf currents is shown in Figure 6-3 for the first two modes of each of the four EOF methods. The spatial behaviors of EOF1 and HEOF1 mode are almost identical and both show the variability increasing over 6 m height. The variation of EOF2 and HEOF2 with depth indicates that the boundary between surface and bottom layer is generally at ~9m height from the bottom. The first two modes of the CEOF analysis are shown in Figure 6-3 C. CEOF1 mode denotes that the vertical variation of currents is mostly uniform with depth. The characteristics of the two-layer flow are evidenced in CEOF2 mode. The boundary between surface and bottom layer is formed at 7m. The vertical profiles for the CHEOF analysis are shown in Figure 6-3 D. The spatial variation of CHEOF1 is smaller than that of the other analyses as noted in Table 6-3 and is approximately 0 at the first bin. As seen in the other second modes, CHEOF2 physically indicates cross-shelf exchange flow. The boundary between onshore and offshore flow appears around 7m height.

Figure 6-4 gives the vertical profiles for the first 2 modes of the along-shelf currents for each of the four methods. Profiles from EOF1, HEOF1 and CHEOF1 display similar vertical structure, but CEOF1 generates a different spatial mode that can be caused by directional ambiguity, as mentioned in Kaihatu et al. (1998). Figure 6-5 shows the shelf aligned wind speed and the first modes of along-shelf currents for the four EOF methods: A) EOF1, B) HEOF1, C) CEOF1 and D) CHEOF1. The first modes of along-shelf currents varied from -24 to 8 cm/s. The first mode for all methods

displayed the same spatial and time distribution. The variance explained by the first mode in Table 6-3 is around 98% for all analyses.

A correlation coefficient was estimated between shelf-aligned winds and cross-shelf currents as shown in Figure 6-6. The solid symbols denote the correlation between mode 1 and shelf aligned winds and the empty symbols describe the correlation between mode1 and shelf aligned winds. As noted in section 3.2, the conventional EOF analysis can detect a stationary pattern that is in phase or π out of phase over the array. Therefore, if x_t and y_t , $t = 1, \dots, n$, are two univariate time series, any permutation of x_t and y_t will yield the same magnitude of correlation coefficient because the way time is arranged is irrelevant (Hannachi et al., 2007) as follows:

$$r^2(x_t, y_t) = r^2(x_{\pi(t)}, y_{\pi(t)}) \quad (6-1)$$

Where r and π are a correlation coefficient and any permutation of the set of time indices (1, 2, 3, ...,n). The magnitude of correlation coefficients is identical throughout the column as seen in Figure 6-6 A. The coefficients in Figure 6-6 B, C, and are different at every depth because the complex variable methods can capture a propagating signal that gradually decreases with depth.

The solid circles show EOF1 mode of cross-shelf currents correlated significantly with the along-shelf wind. The correlation coefficient between EOF1 and the along-shelf wind, which is denoted as ASW in the figure, reached 0.69 except at the first bin. This suggests the first mode is primarily correlated with Ekman transport at the surface layer. The negative correlation value indicates that as the wind force acts in the positive direction, the cross-shelf currents flow to the negative direction, and vice versa. The correlation coefficient between EOF1 and the cross-shelf wind, which is abbreviated to

CSW in the figure, reached 0.41 except at the first bin. This suggests the currents over the inner-shelf can also flow downwind. The empty symbols indicate that while EOF2 is rarely correlated with the along-shelf wind, it is more correlated with the cross-shelf wind. The correlation coefficient between EOF2 and the cross-shelf wind reached 0.59 at the upper layer and -0.59 at the lower layer.

The correlation coefficients between HEOF modes and shelf aligned wind are given in Figure 6-6 B. This figure shows that HEOF1 correlated best with along-shelf wind, where $r \approx 0.7$ at the upper layer. Like EOF2, HEOF2 is more correlated with cross-shelf wind than along-shelf wind and show positive correlation at the upper layer of the water column and negative correlation at the lower layer. The positive value of EOF2 and HEOF2 indicates that a vertically sheared downwind flow develops in the upper layer as well as a compensating upwind flow. The upwind flow is represented by negative values in the lower layer.

The conventional EOF and HEOF are analyzed as decoupled scalars (u , v) so that the results are independent. However, the along- and cross-shelf currents are dependent upon each other. The EOF modes of the along- and cross-shelf currents are dependently sought by complex scalars in the CEOF analysis and a concatenation treatment of CHEOF analyses from the u , v components of the vector field (Kaihatu et al., 1998). Thus, the results of CEOF and CHEOF actually represent the dependence of each velocity component on each other. CEOF1 in Figure 6-6 C correlated highly with along-shelf wind. The correlation coefficient between CEOF1 and cross-shelf wind exhibits a vertically sheared downwind flow generated by cross-shelf wind and a compensating upwind flow which is observed between Dec. 29 and 31 in Figure 6-2 B.

Cross-shelf wind tends to have more of an effect on the exchange flow than along-shelf wind because the coefficient between CEOF2 and cross-shelf wind is around twice as large as the coefficient between CEOF2 and along-shelf wind.

The results of CHEOF analysis are shown in Figure 6-6 D. The correlation coefficient between CHEOF1 and along-shelf wind reaches approximately 0.78 in the upper layer. cross-shelf wind also had a significant effect on the cross-shelf flow described by CHEOF1 mode. CHEOF2 is more relevant to cross-shelf wind like the other analyses but the correlation coefficient value is relatively small. In the results of EOF analyses applied to Deployment 7-1, all of the first and second modes are mostly correlated with along-shelf wind and CWS, respectively. While the first modes are highly correlated with along-shelf wind, the correlation coefficient between second modes and cross-shelf wind are relatively small. The estimation of correlation between the second modes and cross-shelf pressure gradient is needed. The interface between the downwind layer and the upwind layer in the second modes appears at higher location for the conventional EOF and HEOF than for CEOF and CHEOF. The primary purpose here is to compare the differences in the results and what the differences could physically indicate. As noted above, the conventional EOF and HEOF modes of along- and cross-shelf current are calculated as u , v scalars independently. Thus, only results of CEOF and CHEOF are given in the next sections.

6.2 Deployment 8-1

The results of CEOF and CHEOF analyses are shown in Figure 6-7, using the current velocity data from Deployment 8-1. In Figure 6-7 A), the along- and cross-shelf wind speed is described by blue and red solid line, respectively. The first two modes of cross-shelf currents for the CEOF analysis are given in Figure 6-7 B and C. CEOF1

shows unidirectional currents throughout the water column. A difference of magnitude between the surface and bottom layer is rarely observed. This indicates that bottom frictional influences on the cross-shelf flow are small. The variance associated with CEOF1 is 69.5% as given in Table 6-1. CEOF2 shows the cross-shelf exchange flow as observed in Deployment 7-1. The interface layer where the surface and bottom boundary overlap is generally formed at approximately 7m height from the bottom. The energy of CEOF2 represents 20.2% of cross-shelf currents which is smaller than the variance of CEOF2 in Deployment 7-1. The first two CEOF modes combined thus represent approximately 90% of the subtidal cross-shelf currents.

The reconstructed cross-shelf currents for CHEOF analysis are provided in Figure 6-7 D and E. The trend of CHEOF1 is mostly the same as that of CEOF1 except that the variance of CHEOF1 is approximately 10% below that of CEOF1 in Table 6-1. From the along-shelf wind and the first modes: CEOF1 and CHEOF1, it can be determined that the positive along-shelf wind drives onshore currents and negative along-shelf wind enforces offshore currents. CHEOF2 shows the two-layer flows over the cross-shelf direction and describes approximately 16.3% of the subtidal flow. The sum of CHEOF1 and CHEOF2 explained variance is approximately 13.4% smaller than that of CEOF1 and CEOF2 explained variance.

Figure 6-8 and 6-9 shows the spatial variability of the first two modes for the cross- and along-shelf currents, respectively. CEOF1 and CHEOF1 show that the cross-shelf currents are uniformly directed over the depth. While CEOF1 decreases almost linearly, CHEOF1 is nearly the same at the surface and bottom. In the case of the second mode, the CEOF analysis exhibits the cross-shelf exchange flow more clearly

than the CHEOF method. In reality, the discrepancy of the vertical structure between CEOF2 and CHEOF2 is reflected in the reconstructed currents and the variance of the second modes. The spatial patterns of along-shelf currents are shown in Figure 6-9 A and B for CEOF and CHEOF methods, respectively. As noted in section 6.3.1, CEOF1 and CEOF2 include the directional ambiguity. However the spatial variability of CHEOF1 and 2 describes well the reconstructed along-shelf currents of the first CHEOF mode. Figure 6-10 shows the CEOF1 and CHEOF1 mode of the along-shelf currents with the shelf aligned wind speed. There is no much difference between the reconstructed along-shelf currents of CEOF1 and CHEOF1. The variance of CEOF1 and CHEOF1 describes approximately 84% and 78.3% of the subtidal along-shelf currents, respectively. The vertical distribution of along-shelf currents decreases almost linearly with depth as seen in Figure 6-10 B and C. The direction of along-shelf currents throughout the water column corresponded to the direction of along-shelf winds.

The results of calculating a correlation coefficient between reconstructed currents and winds are obtained for CEOF and CHEOF analyses in Figure 6-11. The first modes of CEOF and CHEOF are primarily correlated with along-shelf wind. The correlation coefficient between CEOF1 and along-shelf wind is approximately 0.85 throughout the water column. The coefficient between CHEOF and along-shelf wind reached approximately 0.81 which only slightly decreases below 4m depth. The second modes for CEOF and CHEOF are more correlated with cross-shelf wind than with along-shelf wind. In this case the correlation coefficient between CEOF2 and cross-shelf wind are larger than that between CHEOF2 and cross-shelf wind at the upper layer. Hence CEOF2 better describes a vertically sheared downwind flow generated by cross-shelf

wind than CHEOF2. The interface between the downwind and upwind flow interestingly exists at around 7m and 7.5m height, which indicates bottom boundary layer is thicker than surface boundary layer. This is also observed in Deployment 7-1.

6.3 Deployment 9-1

To understand the dynamics of the inner shelf in the summer season, CEOF and CHEOF analyses are applied to Deployment 9-1 collected in 2009. As shown in Figure 6-12 the shelf aligned wind speed is weaker in comparison to the other two deployments given in section 6.3.1 and 6.3.2. The surface and bottom Ekman layer thicknesses are highly variable due to the dependence of the strength of the wind and wave forcing on stratification (Lentz and Fewings, 2012). In the previous two deployments the correlation coefficients between the first modes and the along-shelf wind indicates that the first modes describe transport perpendicular to the along-shelf wind (the right of the along-shelf wind direction in northern hemisphere). A compensating return flow caused by the pressure gradient is not observed in the first modes of Deployment 7-1 and 8-1 data. However, the compensating return flow is shown in the bottom layer in Deployment 9-1, because as the wind decreases, the surface boundary layer thickness decreases.

The cross-shelf currents reconstructed by the CEOF and CHEOF methods are provided in Figure 6-12. The CEOF1 in Figure 6-12 B tends to correspond with the along-shelf wind at the upper layer, that is, the along-shelf wind causes a net water transport to the right of the along-shelf wind direction. There is a return flow at the lower layer which is likely caused by the cross-shelf pressure gradient. The first mode of CEOF contributes 84% of the variance of the cross-shelf currents in Table 6-1. CEOF2 of the cross-shelf currents also shows two-layer currents and the interface is formed at

around 6m height above the bottom. The variance of CEOF2 reaches around 12%.

Figure 6-12 D and E provide results of CHEOF analysis. The first two leading modes of cross-shelf currents for CHEOF method are almost the same as those of the CEOF method. The variance of CHEOF1 and 2 was around 78% and 10.5% of the cross-shelf currents.

The spatial variability of cross- and along-shelf currents is given in Figure 6-13 and 20, respectively. The CEOF1 of cross-shelf currents in Figure 6-13 A shows large values in the upper layer, which decrease with depth. Mode CEOF2 denotes exchange flow because the variability above and below approximately 7m is in the opposite sign. In addition, CHEOF1 of cross-shelf currents in Figure 6-14 B) indicated positive and negative values above and below 4 m height, respectively. However, CHEOF2 does not show a two-layer flow structure. For along-shelf currents, the CHEOF analysis expresses the actual spatial variability rather than the CEOF method, as shown in Figure 6-14. The eigenvector in the last bin has only real values and the eigenvector of the v component is described as an imaginary number. As a result, the spatial variability of CEOF modes in the last bin always goes to zero. From these eigenvectors as shown in Figure 6-14 the first modes of reconstructed along-shelf currents are given in Figure 6-15 A for CEOF and B for CHEOF method. In this deployment the discrepancy of along-shelf currents between the upper layer and the lower layer is larger than in the other two deployments. This indicates the along-shelf bottom friction is relatively large and can cause a bottom Ekman layer with a transport driven to the left of the along-shelf currents.

The vertical variation of the correlation coefficients between the first two modes and shelf-aligned wind is provided in Figure 6-16 A for CEOF and B for CHEOF analyses. The correlation coefficient between CEOF1 and along-shelf wind is approximately 0.75 in the upper layer. Negative correlation coefficients (approximately -0.6) are observed in the lower layer, which describes the transport driven to the left of along-shelf wind. The coefficient between CHEOF1 and along-shelf wind reaches around 0.77 in the upper layer and -0.47 in the bottom layer. The positive and negative correlation coefficients are consistent with surface and bottom Ekman transports, respectively. The second modes of cross-shelf currents are more correlated with cross-shelf wind than in the other two deployments. The correlation coefficients between CEOF2 and cross-shelf wind reach around 0.56; then, the coefficient gradually decreases and reach approximately -0.6 at the bottom. The correlation coefficients between CHEOF2 and cross-shelf wind are around 0.53 in the upper layer and around -0.5 in the bottom. Therefore, the second modes of cross-shelf currents have an element of downwind flow in the upper layer and upwind flow in the lower layer generated by cross-shelf wind.

These studies generally found that the low-pass filtered unidirectional cross-shelf currents are mainly driven by along-shelf wind. According to the strength of wind stress, the thickness of surface and bottom layer can be changed in time. Surface and bottom boundary layers generated by surface and bottom Ekman transport could be observed, when the mean low-pass filtered wind speed was 3.3 m/s during Deployment 9-1. The bottom Ekman transport were rarely seen during Deployment 7-1 and 8-1 when the mean low-pass filtered wind speed was stronger than 5.8 m/s. Two layer flow generated

by cross-shelf wind was obtained three deployments. This shows that cross-shelf wind is also an important element that drives the cross-shelf circulation.

Table 6-1. Total energy or variance of each mode in the cross- and along-shelf current field. The acronyms stand for EOF for regular empirical orthogonal function, HEOF for Hibert EOF, CEOF for Complex EOF and CHEOF for Concatenated HEOF. Unites are percentage (%).

Methods	Mode #	Cross-shelf current			Along-shelf current		
		Depl. 7-1	Depl. 8-1	Depl. 9-1	Depl. 7-1	Depl. 8-1	Depl. 9-1
EOF	1	63.2	-	-	98.1	-	-
	2	31.7	-	-	1.3	-	-
	3	2.6	-	-	0.4	-	-
HEOF	1	63.7	-	-	98.1	-	-
	2	31.9	-	-	1.3	-	-
	3	2.4	-	-	0.3	-	-
CEOF	1	62.4	69.5	84.0	98.0	95.7	96.7
	2	32.7	20.2	11.9	1.5	3.1	2.1
	3	2.6	8.2	1.9	0.4	1.0	0.6
CHEOF	1	43.3	60.0	78.3	98.2	95.2	96.8
	2	30.4	16.3	10.5	0.6	3.1	0.6
	3	19.5	11.7	3.2	0.7	0.7	1.3

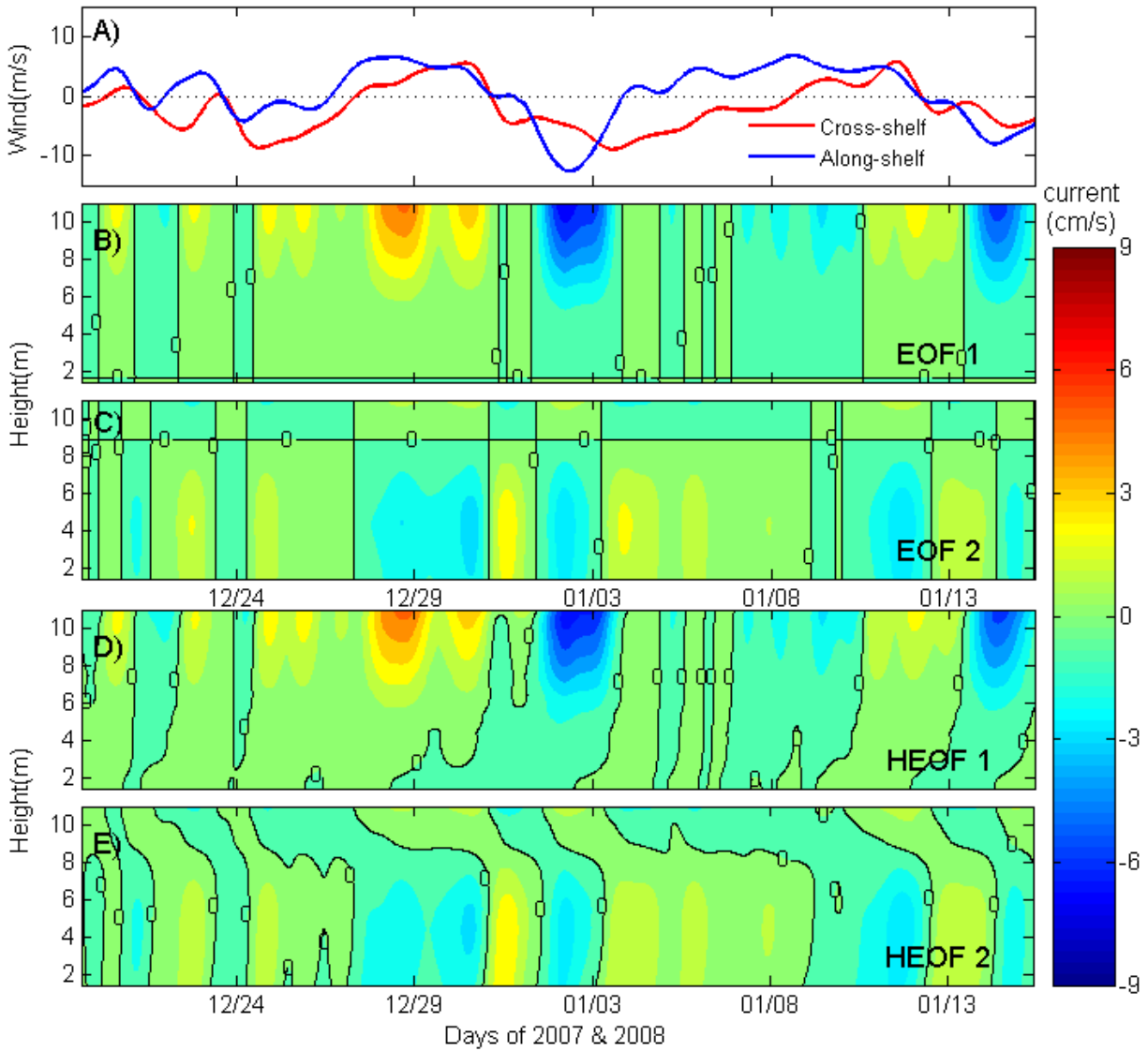


Figure 6-1. Comparison of EOF and HEOF analysis in the cross-shelf current during Deployment 7-1. The time series of A) the magnitude of cross- (red solid line) and along-shelf (blue solid line) wind speed. The reconstructed cross-shelf currents of B) the first and C) the second EOF mode, and D) the first and E) the second HEOF mode.

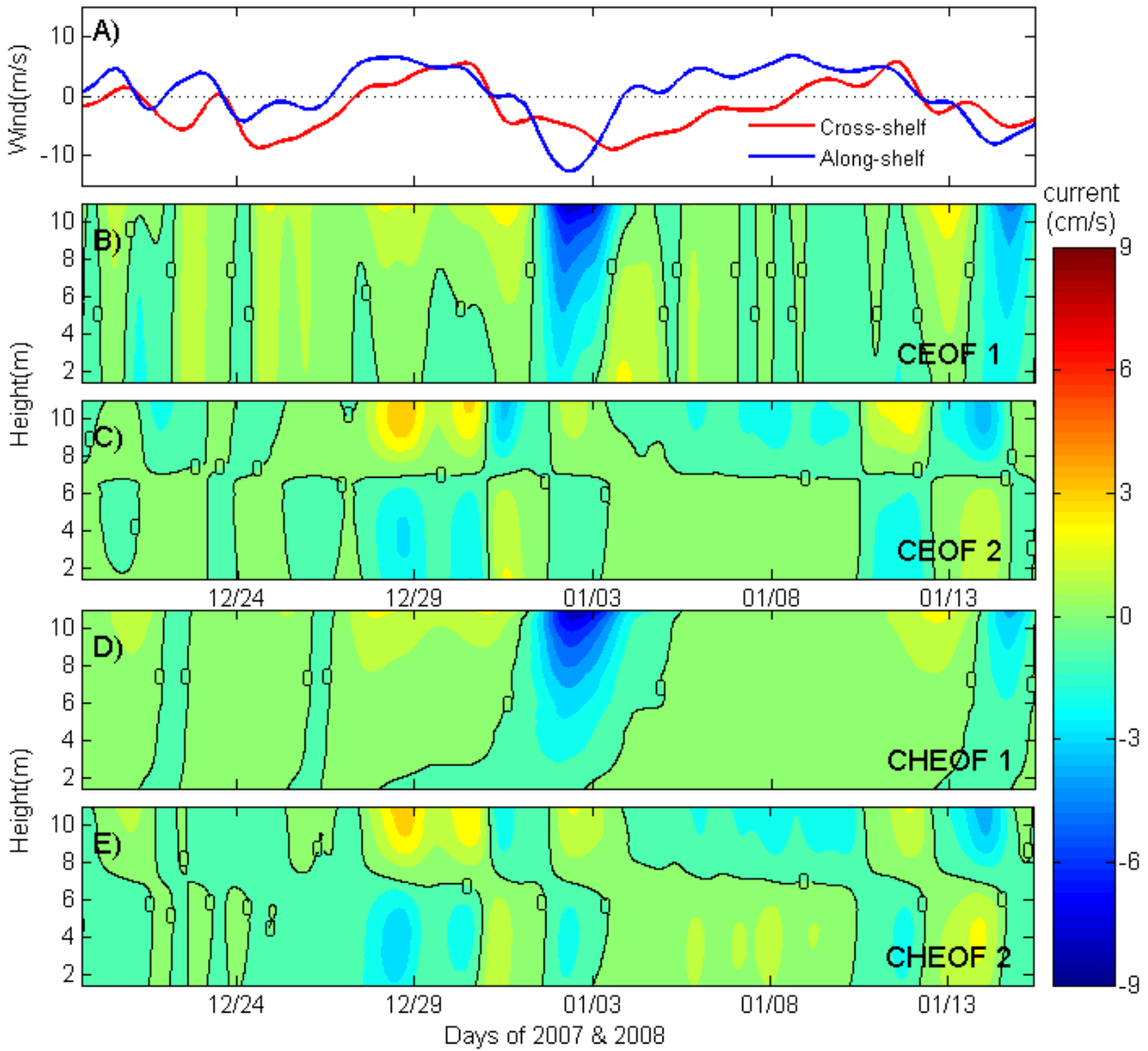


Figure 6-2. Comparison of CEOF and CHEOF analysis in the cross-shelf current during Deployment 7-1. The time series of A) the magnitude of cross- (red solid line) and along-shelf (blue solid line) wind speed. The reconstructed cross-shelf currents of B) the first and C) the second CEOF mode, and D) the first and E) the second CHEOF mode.

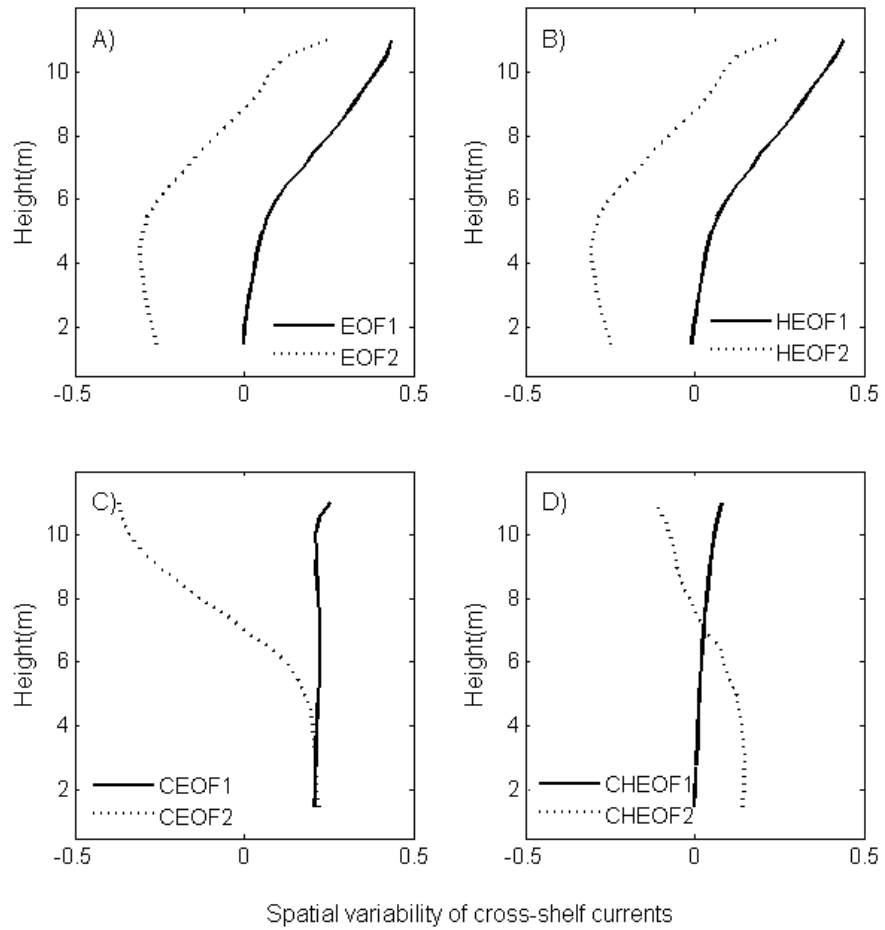


Figure 6-3. The first and second mode (eigenvectors) of cross-shelf currents using EOF, HEOF, CEOF and CHEOF methods during Deployment 7-1.

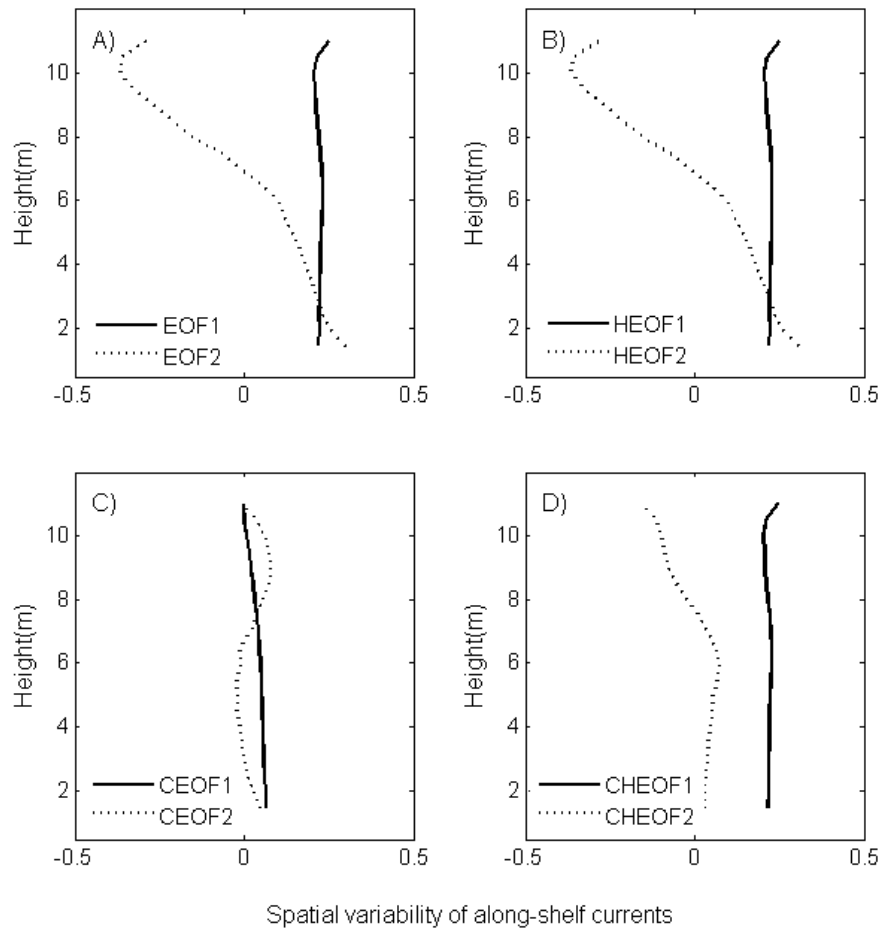


Figure 6-4. The first and second mode (eigenvectors) of along-shelf currents using EOF, HEOF, CEOF and CHEOF methods during Deployment 7-1.

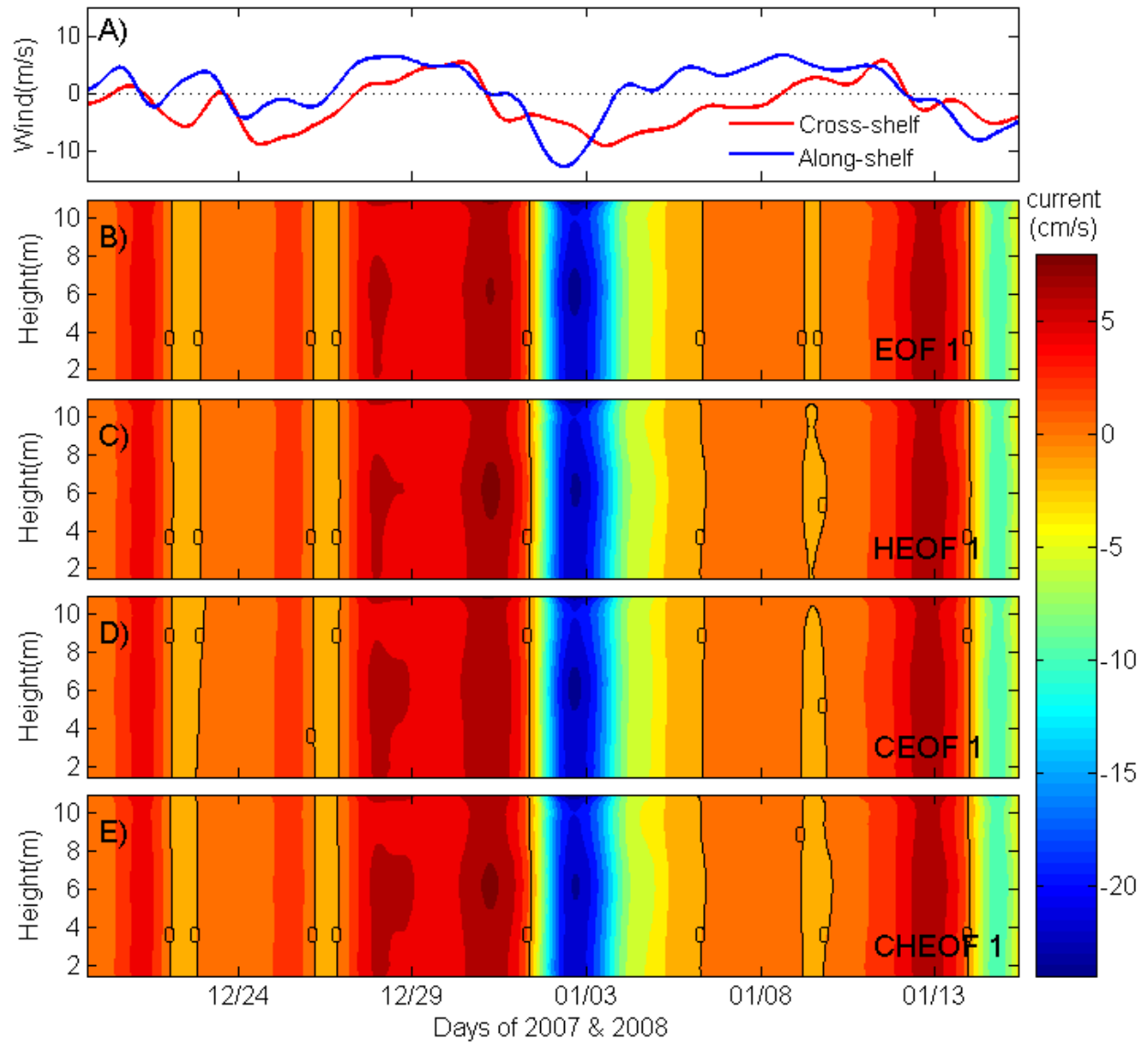


Figure 6-5. Comparison of EOF, HEOF, CEOF and CHEOF analysis in the along-shelf current during Deployment 7-1. The time series of A) the magnitude of cross- (red solid line) and along-shelf (blue solid line) wind speed. The reconstructed along-shelf currents of the first mode of each method: B) EOF, C) HEOF, D) CEOF and E) CHEOF.

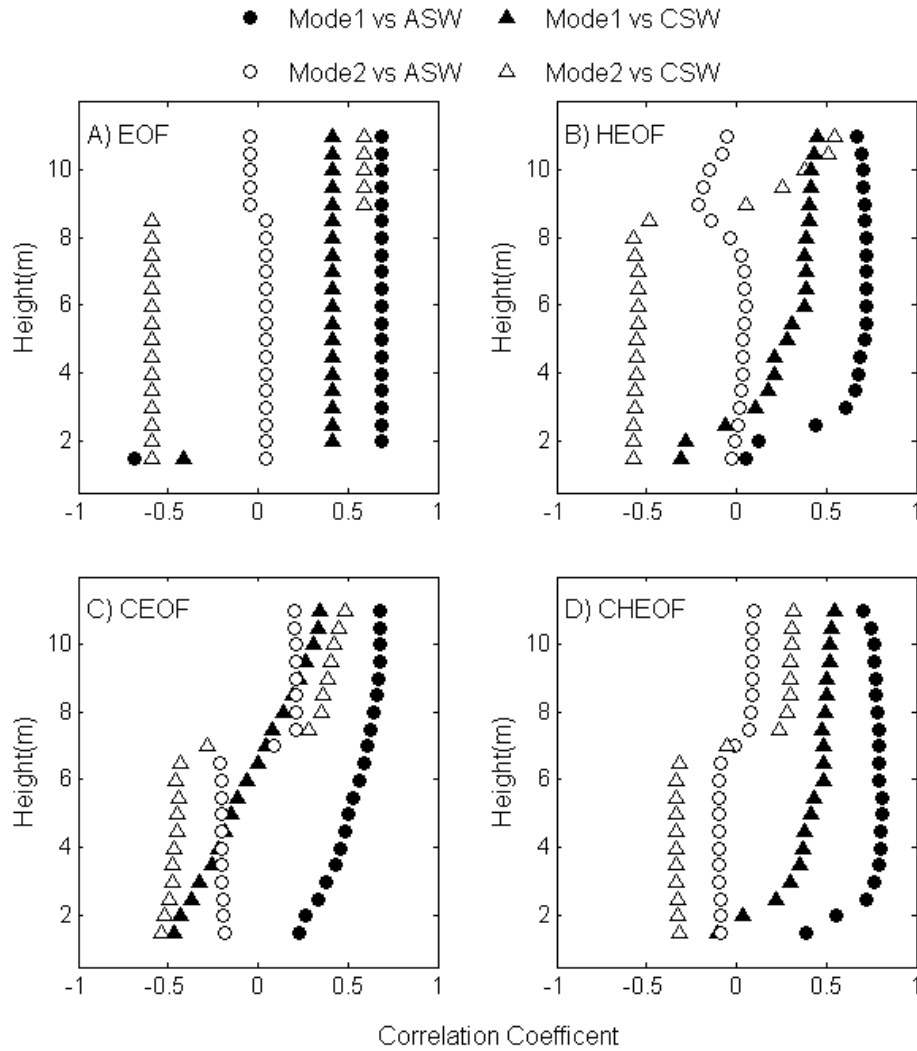


Figure 6-6. Comparison of correlation coefficient between EOF modes: A) EOF, B) HEOF, C) CEOF and D) CHEOF, and shelf aligned winds during Deployment 7-1. The solid symbols denote correlation coefficient of mode 1 and the shelf aligned winds: ASW and CSW, The empty symbols denote correlation coefficient of mode 2 and the shelf aligned winds.

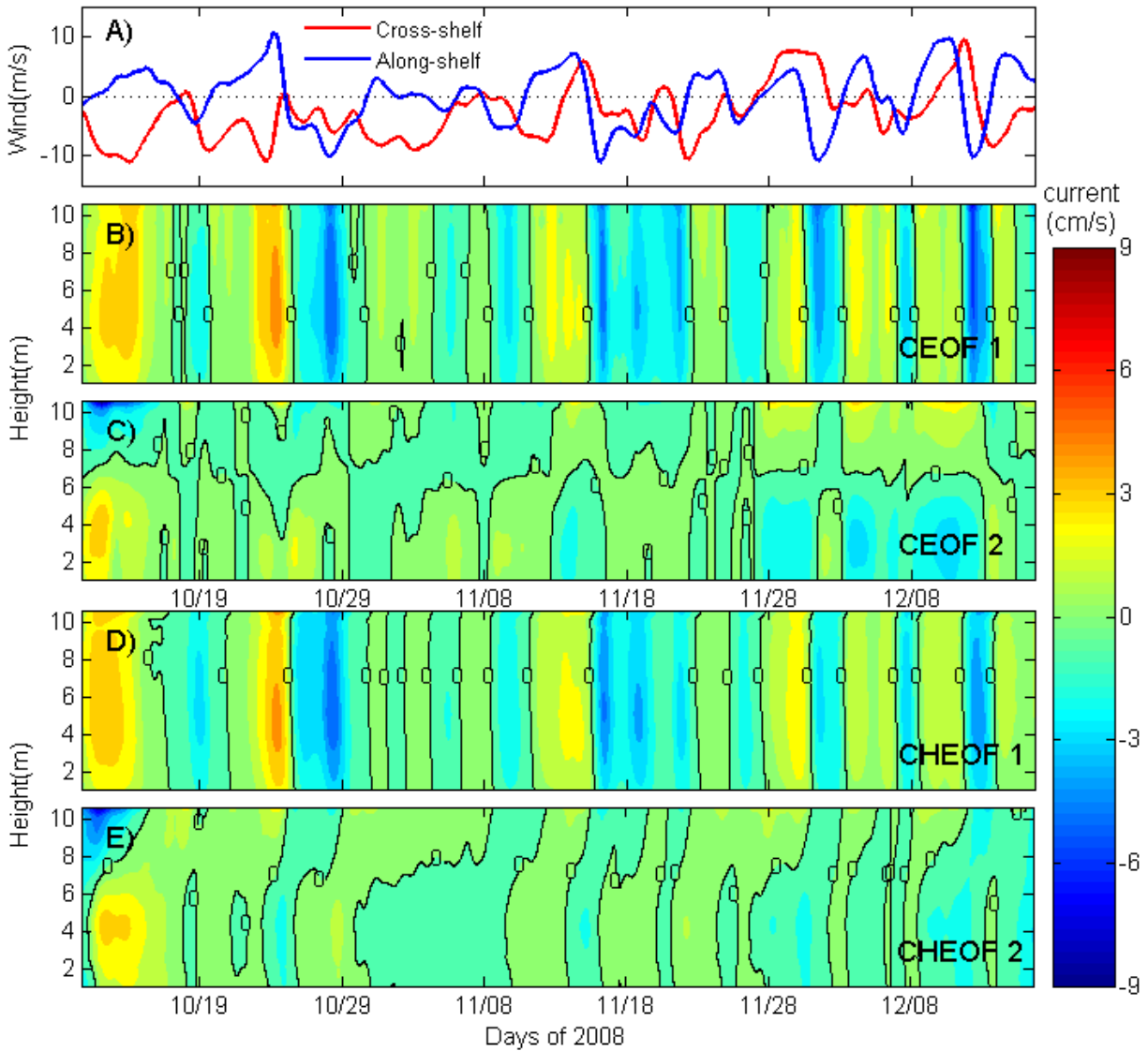


Figure 6-7. Comparison of CEOF and CHEOF analysis in the cross-shelf current during Deployment 8-1. The time series of A) the magnitude of cross- (red solid line) and along-shelf (blue solid line) wind speed. The reconstructed cross-shelf currents of B) the first and C) the second CEOF mode, and D) the first and E) the second CHEOF mode.

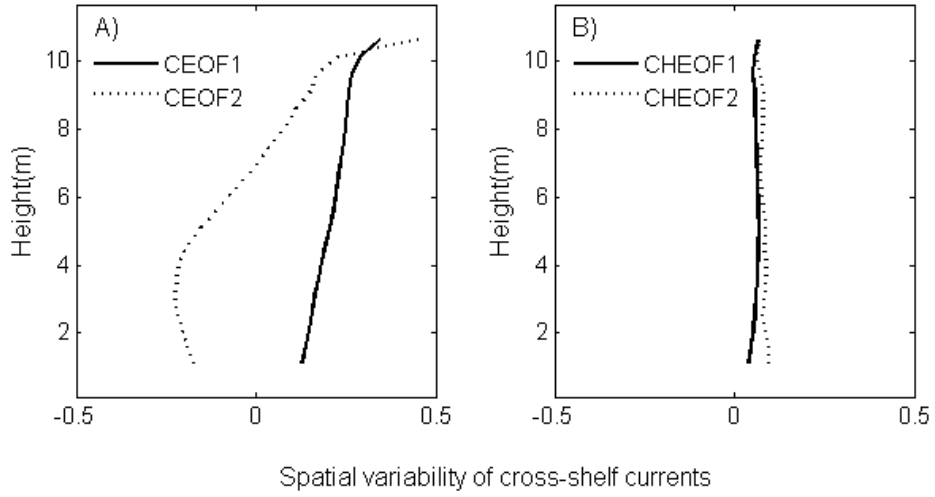


Figure 6-8. The first and second mode (eigenvectors) of cross-shelf currents using CEOF and CHEOF methods during Deployment 8-1.

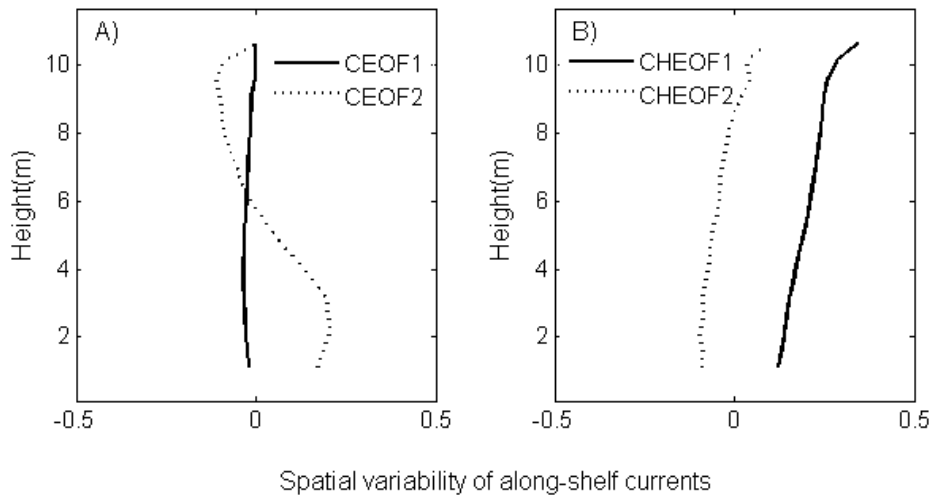


Figure 6-9. The first and second mode (eigenvectors) of along-shelf currents using CEOF and CHEOF methods during Deployment 8-1.

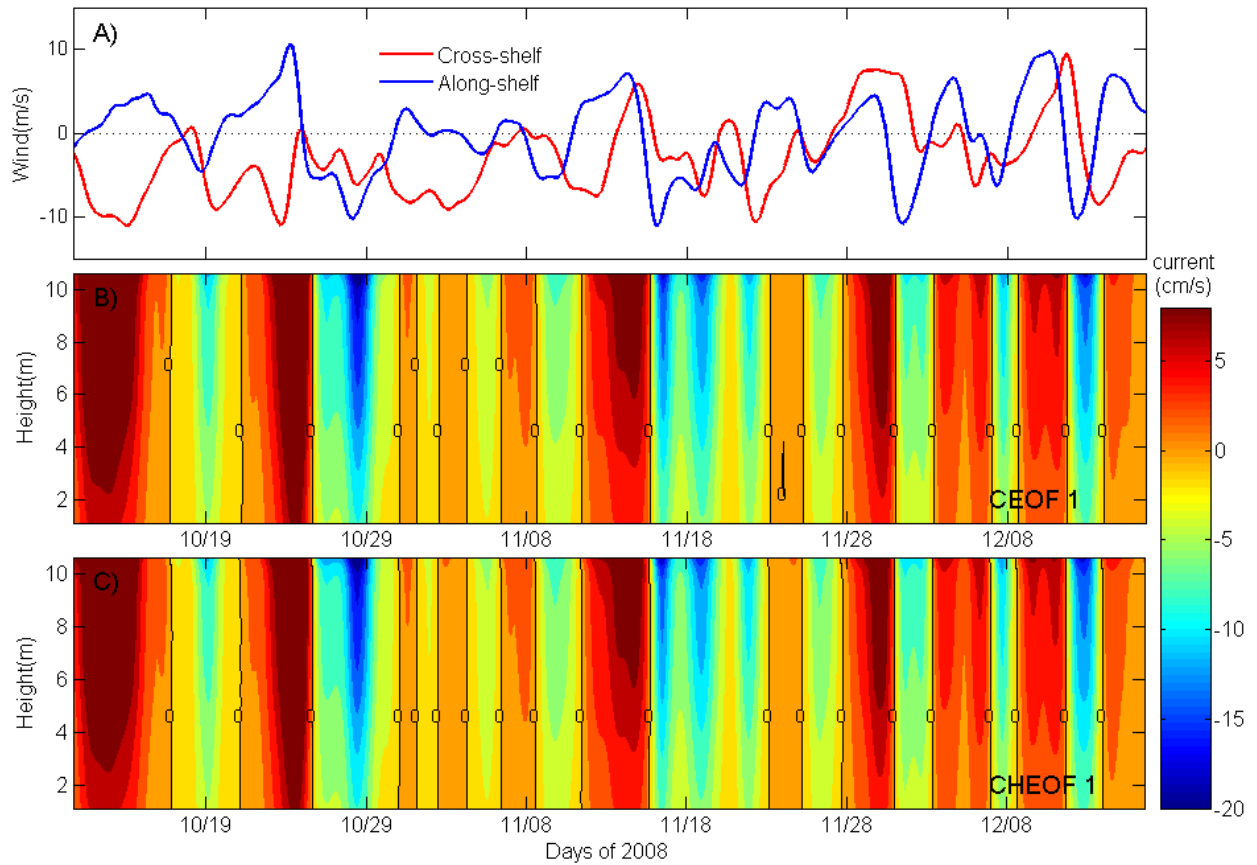


Figure 6-10. Comparison of CEOF and CHEOF analysis in the along-shelf current during Deployment 8-1. The time series of A) the magnitude of cross- (red solid line) and along-shelf (blue solid line) wind speed. The reconstructed along-shelf currents of the first mode of each method: B) CEOF and C) CHEOF.

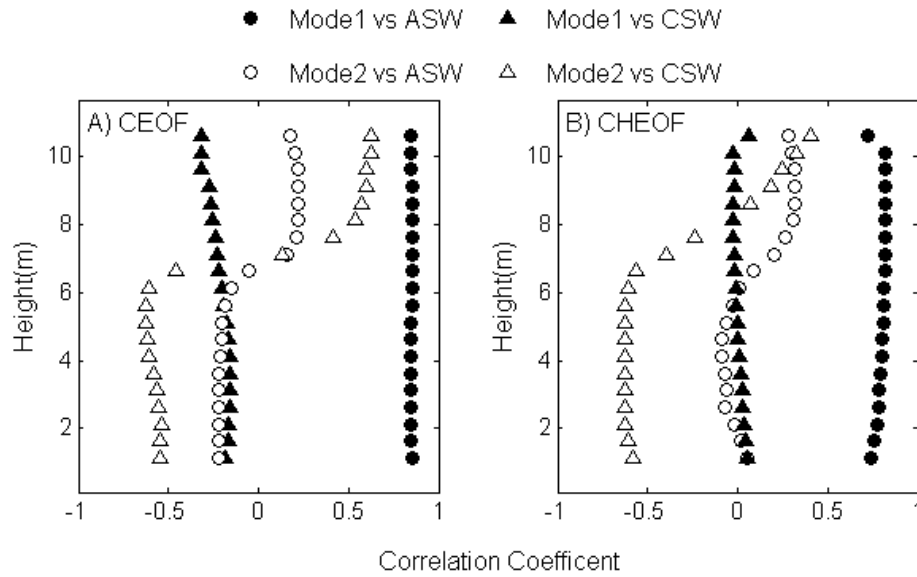


Figure 6-11. Comparison of correlation coefficient between EOF modes: A) CEOF and B) CHEOF, and shelf aligned winds during Deployment 8-1. The solid symbols denote correlation coefficient of mode 1 and the shelf aligned winds: ASW and CSW, The empty symbols denote correlation coefficient of mode 2 and the shelf aligned winds.

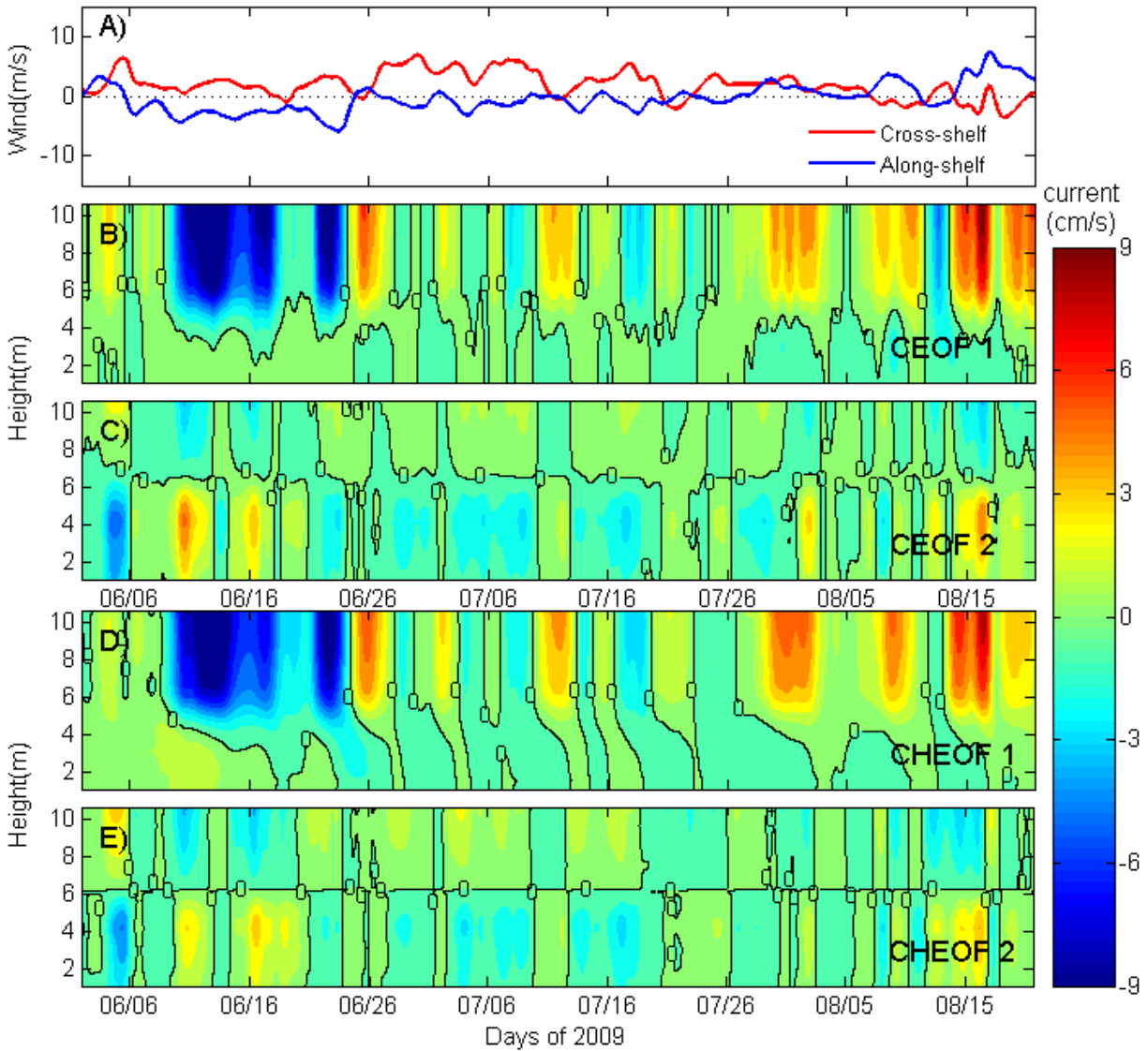


Figure 6-12. Comparison of CEOF and CHEOF analysis in the cross-shelf current during Deployment 9-1. The time series of A) the magnitude of cross- (red solid line) and along-shelf (blue solid line) wind speed. The reconstructed cross-shelf currents of B) the first and C) the second CEOF mode, and D) the first and E) the second CHEOF mode.

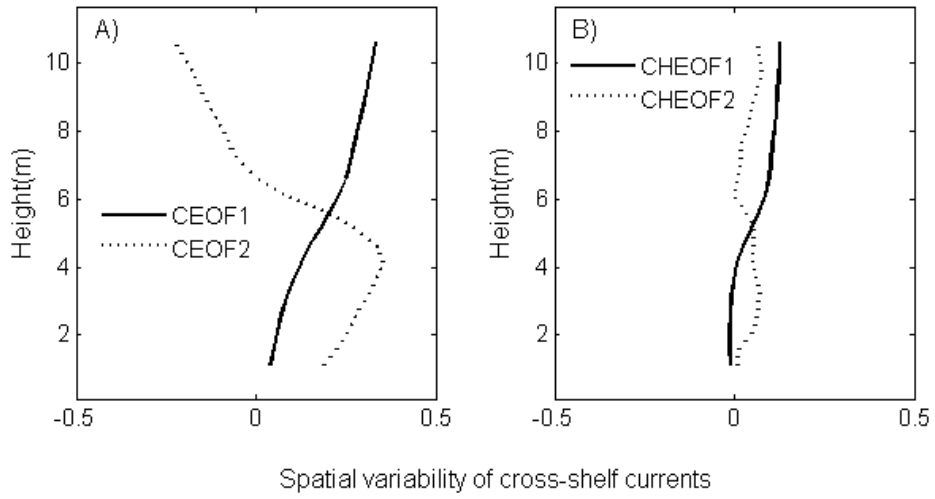


Figure 6-13. The first and second mode (eigenvectors) of cross-shelf currents using CEOF and CHEOF method during Deployment 9-1.

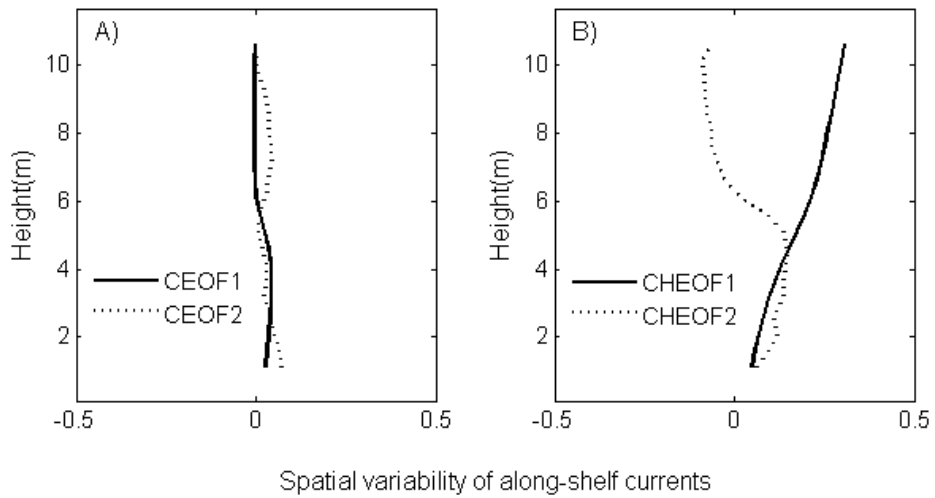


Figure 6-14. The first and second mode (eigenvectors) of along-shelf currents using CEOF and CHEOF method during Deployment 9-1.

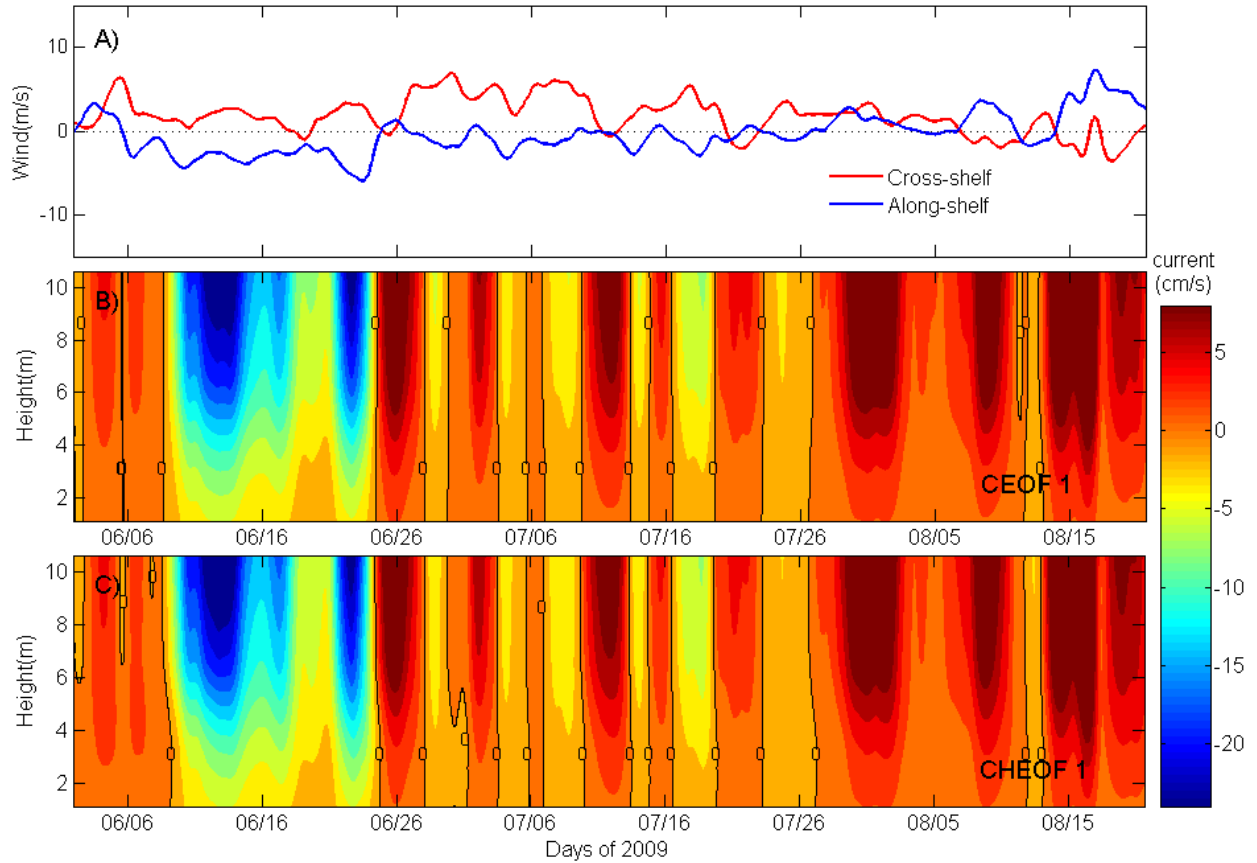


Figure 6-15. Comparison of CEOF and CHEOF analysis in the along-shelf current during Deployment 9-1. The time series of A) the magnitude of cross- (red solid line) and along-shelf (blue solid line) wind speed. The reconstructed along-shelf currents of the first mode of each method: B) CEOF and C) CHEOF.

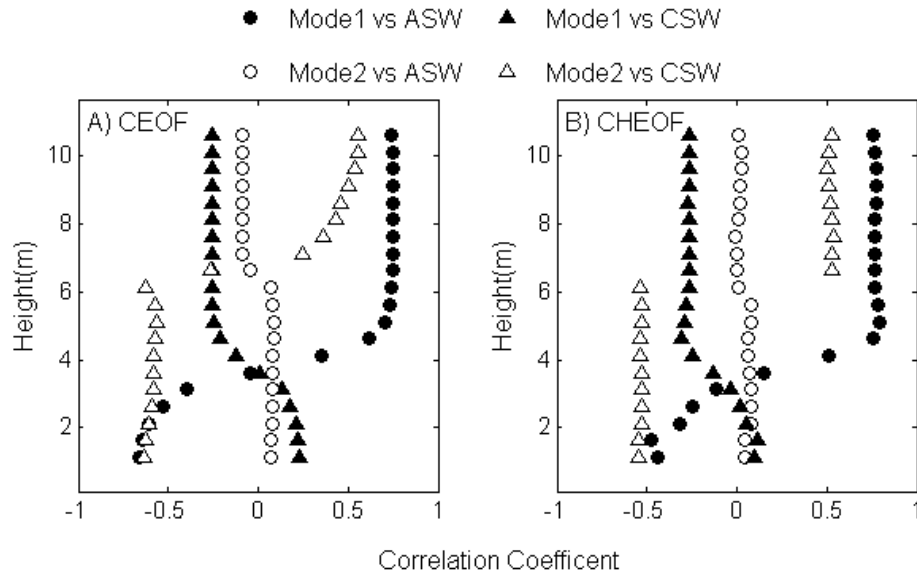


Figure 6-16. Comparison of correlation coefficient between EOF modes: A) CEOF and B) CHEOF, and shelf aligned winds during Deployment 9-1. The solid symbols denote correlation coefficient of mode 1 and the shelf aligned winds: ASW and CSW, The empty symbols denote correlation coefficient of mode 2 and the shelf aligned winds.

CHAPTER 7 DYNAMICS OF WIND-DRIVEN SHELF CIRCULATION

Coastal circulation in shallow water is driven by a combination of atmospheric forcing and buoyancy fluctuations (heat and freshwater fluxes), or from deep ocean forcing that is transmitted across the shelf break (Weisberg et al., 2005). The cross-shelf exchange is a key process in connecting the shore to the abyssal ocean by transporting pollutants, larvae, phytoplankton, nutrients and sediment (Lentz and Fewings, 2012). In recent decades, the studies of inner shelf region have been studied in large extent as depth-averaged flow, momentum balances, wind- or wave-driven motions, tides, and the associate dynamics.

The relation between currents and winds are analyzed to understand the dynamics of the West Florida Inner shelf. This study is motivated by the importance of cross-shelf exchange and aims to estimate the dominant processes that drive inner shelf circulation. Using the data and the methodologies mentioned in Chapter 4, the vertical structure of cross- and along-shore currents are provided to evaluate the physical processes affecting the circulation. The wind-driven upwelling and downwelling are evaluated by utilizing EOFs. Also, turbulent vertical mixing is investigated with the structure function method in order to measure the rate of turbulent dissipation.

7.1 Cross-Shelf Momentum Balance

It is widely accepted that a geostrophic balance between Coriolis acceleration and across-shelf pressure gradient dominates the depth-averaged cross-shelf momentum balance at the outer and mid shelf areas (Lentz et al., 1999; Liu and Weisberg, 2005; Fewings and Lentz, 2010). The depth-averaged cross-shelf momentum balance within the surfzone tends to be a wave setup balance between the

wave radiation stress divergence and the cross-shelf pressure gradient (Lentz and Raubenheimer, 1999). Both a geostrophic and wave setup balance can be substantial over the inner shelf (Lentz et al., 1999). The importance of the across-shelf wind stress on a mechanism for a coastal setup and set-down has also been shown over the inner shelf both observationally (Liu and Weisberg, 2005) and numerically (Tilburg, 2003). As depth decreases the cross-shelf wind stresses play an important role in the setup (setdown) due to the shallowness of the water, relative to the surface and bottom boundary layer thickness (Lentz et al., 1999).

The dynamics of the inner shelf are complicated because the cross-shelf pressure gradient can be balanced with the Coriolis acceleration, the wave radiation stress associated with shoaling waves, the surface and bottom stresses or a combination of those terms (Fewings and Lentz, 2010). In this section the depth-averaged cross-shelf momentum terms are estimated for Deployment 7-1, 8-1 and 9-1 to determine the dominant dynamical balances over the West Florida Inner Shelf. All the momentum budget terms are estimated with the low-pass filtered data to remove the tidal and other high-frequency oscillations. The coordinate system at each mooring is based on the shelf aligned coordinate system, with x positive onshore and y positive along-shelf northward described in section 4.1.

To estimate the dominance of each term in the fluctuating momentum budget, the standard deviation is calculated on subtidal time scales as shown in Table 7-1. Liu and Weisberg (2005) showed the dominance of Coriolis, pressure gradient and the cross-shelf wind stress over the West Florida Inner Shelf. In the cross-shelf budget, the dominant terms are the wind stress and Coriolis acceleration that are balanced by the

cross-shelf pressure gradient term. The other terms: the local acceleration and bottom stress are an order of magnitude smaller. The time-mean of each term is given in Table 7-1. The wind stress is largest, followed by Coriolis acceleration.

It is also shown in Figure 7-1, 7-2 and 7-3 that wind stress and Coriolis acceleration plays a key role in the dynamics over the inner shelf. All deployments showed the importance of the wind stress and Coriolis acceleration. While the magnitude of wind stress is largest during both Deployment 7-1 and 8-1, Coriolis acceleration surpassed wind stress during Deployment 9-1. This implies that the geostrophic balance has also an important role in the inner shelf dynamics. Hence the dynamics of the inner shelf area is a combination of geostrophic balance and the coastal setup and setdown balance driven by the cross-shelf wind stress.

7.2 Along-Shelf Momentum Balance

The along-shelf momentum balance over the inner shelf predominantly tends to be among three terms: along-shelf wind stress, bottom stress and pressure gradient (Lentz, 1994; Fewings and Lentz, 2010). Therefore, the along-shelf dynamics of the inner shelf may be simpler than the dynamics of the mid-shelf where Coriolis, wind stress, bottom stress, acceleration, and pressure gradient terms can play an important role (Fewings and Lentz, 2010). Also, it was showed that the pressure gradient is significantly correlated with the wind stress during summer at the deployment sites which had 12 m and 27 m depth. In this study, the wind stress, Coriolis, bottom stress and local acceleration are estimated as in section 3.3.

The largest standard deviation of the momentum budget is the wind stress as given in Table 7-2. The dominance of the wind stress is also shown in a previous study (Liu and Weisberg, 2005) over the West Florida Shelf. The Coriolis, bottom stress and

acceleration terms are not negligible; they all have the same order of magnitude except that bottom stress of Deployment 7-1 is an order of magnitude bigger. The standard deviation of bottom stress term is about half as large as the wind stress term during Deployment 7-1. The smallest term is the Coriolis term when the standard deviation of the wind stress is large during Deployment 7-1 and 8-1, compared to Deployment 9-1. The standard deviation of the Coriolis term becomes larger than that of the bottom stress and local acceleration during Deployment 9-1, as the wind stress decreases. This suggests that the transition region between the midshelf and inner shelf moves onshore of the mooring site.

The time series of fluctuating momentum budget is provided in Figure 7-4, 7-5 and 7-6. The wind stress term dominates the along-shore momentum budget for all three deployments. The importance of the wind stress, pressure gradient and bottom friction is shown in previous momentum budget studies over the inner shelf (Fewings and Lentz, 2010; Liu and Weisberg, 2005). These studies demonstrated that the pressure gradient is significantly correlated with the difference between the wind stress and bottom stress, but Coriolis and other acceleration terms are not negligible. As shown in Figure 7-4, the along-shelf momentum budget is dominated by the wind stress and bottom stress during Deployment 7-1. Figure 7-5 and 7-6 display the Coriolis and local acceleration play an important role in the along-shelf momentum balance as they have the same order of standard deviation magnitude with the bottom stress given in Table 7-2.

7.3 The Dissipation of Turbulent Kinetic Energy

To understand the vertical exchange of horizontal momentum associated with surface (wind) and bottom stresses, the dissipation of TKE was estimated using the

second order structure function method (Wiles et al., 2006). This method was described in section 3.5. The structure function was applied to ADCP data collected in winter of 2009 every second during nearly 2 weeks. The spectral density of water surface height is given in Figure 7-7. In Figure 7-7 A the first two peaks at low frequencies indicate the diurnal and semidiurnal harmonic constituents and the higher frequency peaks, between 0.08 and 0.3 Hz, suggest energy generated by wind-driven short waves. Figure 7-7 B shows the results of spectral density after the frequency band between 0.08 and 0.3 Hz was filtered out using a band-stop filter. The energy of wind-driven short waves is removed from the time series of along- and cross-shelf currents to delimit the boundary layer dynamics of wind-driven flows or internal wave dynamics through the stratification. This tends to reduce the dissipation rate of TKE that can be contaminated by wind-driven wave motions, especially at the water surface.

The wind vector plots and the shelf-aligned directions are shown in Figure 7-8 A during Deployment 9-1. The largest wind speed occurred November 22 reaching values of 19.2 m/s and the mean was recorded as 6.4 m/s. Figure 7-8 B shows a time series of water surface height (m) and contoured TKE dissipation rate (m^2/s^3). The turbulent fluxes in the middle of the water column oscillated with the water surface height. As shown in the figure, the strong dissipation rates are produced at the bottom, at the surface, and also at the interface between bottom and surface boundary layer interactions. As a consequence, mixing on the shelf is mainly controlled by friction near the bottom and surface and at the interface between bottom and surface boundary layers. It is mentioned by Mitchum and Sturges (1982) that the water column during the winter is nearly unstratified on the West Florida Shelf. Therefore, under the assumption

of no stratification in the inner-shelf, the turbulent fluxes in the middle of water column were likely associated with the two-layer flow mentioned in Chapter 6. Also the strong dissipation rates in the middle disappeared during the wind event on November 22. As shown in section 6.1 and 6.2 the cross- and along-shelf currents were mainly unidirectional when the wind stress was strong. Hence, current differences rarely exist between surface and bottom boundary layers. This can cause weak dissipation rates in the middle of the water column, or uniform dissipation throughout the water column. When wind stress is small (< 7 m/s) TKE is predominantly dissipated in the interface between the bottom and surface boundary layers because of the enhanced vertical shears associated with exchange flows (section 6.3). This is a finding that has not been reported over the inner shelf and therefore is a valuable contribution of this study.

Table 7-1. Statistics of terms in the cross-shelf momentum budgets during Deployment 7-1, 8-1 and 9-1. Units are 10^{-6} m/s^2 .

Term	Standard Deviation			Time-mean		
	Depl. 7-1	Depl. 8-1	Depl. 9-1	Depl. 7-1	Depl. 8-1	Depl. 9-1
Wind stress	3.83	4.83	1.34	-2.08	-2.83	0.88
Coriolis	2.23	1.96	2.11	-0.93	-1.11	-0.42
Bottom stress	0.39	0.46	0.24	-0.65	-0.18	0.21
Acceleration	0.25	0.27	0.23	-0.00	-0.00	0.00

Table 7-2. Statistics of terms in the along-shelf momentum budgets during Deployment 7-1, 8-1 and 9-1. Units are 10^{-6} m/s^2 .

Term	Standard Deviation			Time-mean		
	Depl. 7-1	Depl. 8-1	Depl. 9-1	Depl. 7-1	Depl. 8-1	Depl. 9-1
Wind stress	4.31	5.42	1.37	-0.34	-0.45	-0.18
Coriolis	0.40	0.64	0.73	-0.43	-0.19	-0.25
Bottom stress	2.26	0.98	0.59	-0.79	-0.66	-0.12
Acceleration	0.75	0.69	0.47	-0.02	-0.00	0.00

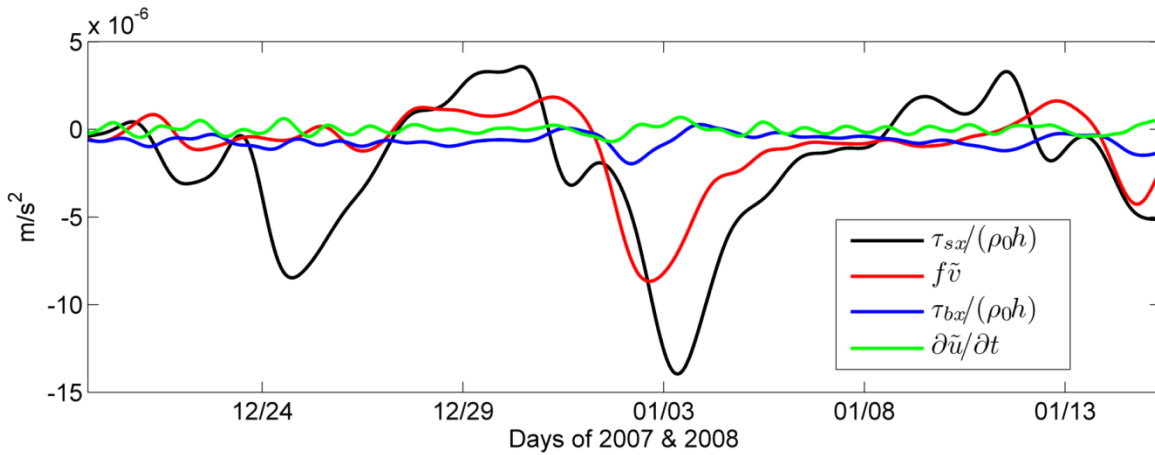


Figure 7-1. Time series of cross-shelf momentum terms: wind stress $\tau_{sx}/\rho_0 h$ (black line), Coriolis acceleration $f\tilde{v}$ (red line), bottom stress $\tau_{bx}/\rho_0 h$ and local acceleration $\partial\tilde{u}/\partial t$ during Deployment 7-1.

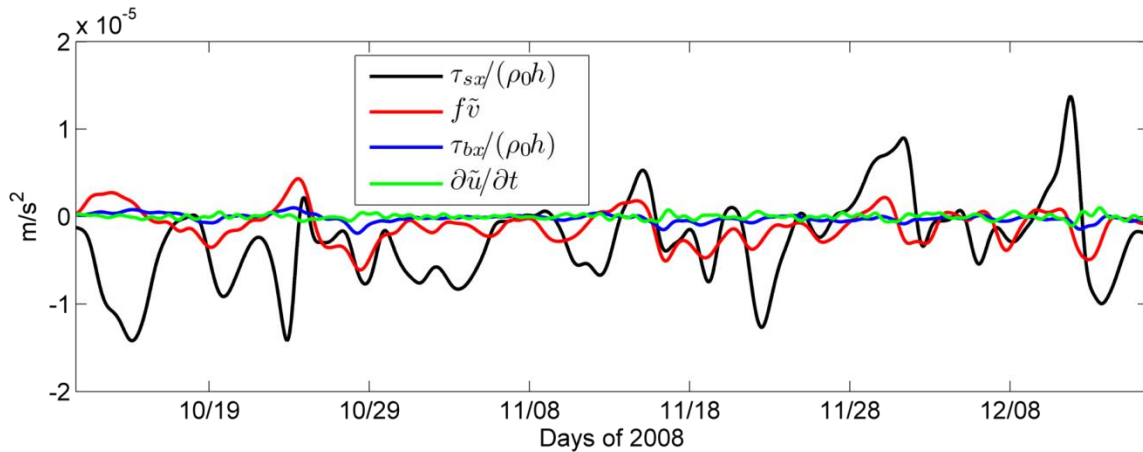


Figure 7-2. Time series of cross-shelf momentum terms: wind stress $\tau_{sx}/\rho_0 h$ (black line), Coriolis acceleration $f\tilde{v}$ (red line), bottom stress $\tau_{bx}/\rho_0 h$ and local acceleration $\partial\tilde{u}/\partial t$ during Deployment 8-1.

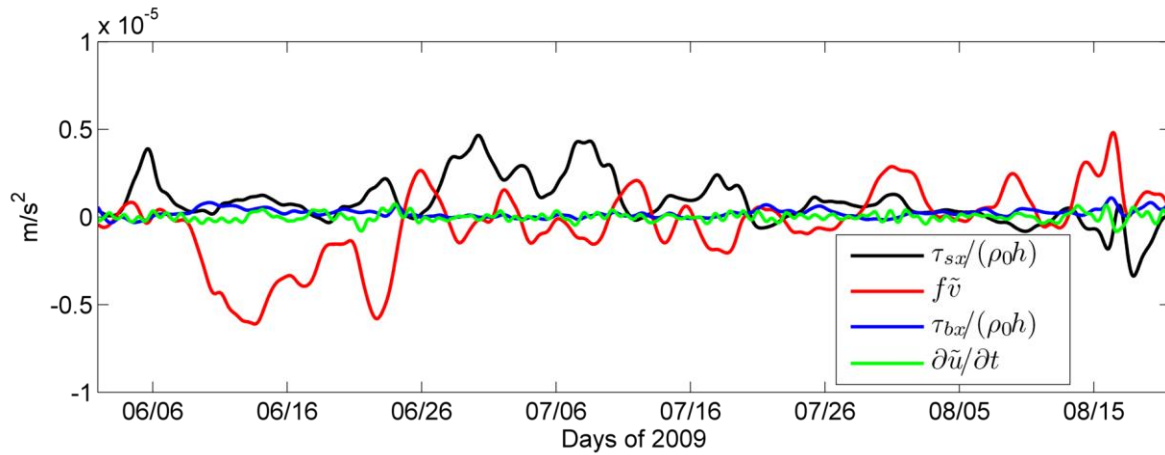


Figure 7-3. Time series of cross-shelf momentum terms: wind stress $\tau_{sx}/\rho_0 h$ (black line), Coriolis acceleration $f\tilde{v}$ (red line), bottom stress $\tau_{bx}/\rho_0 h$ and local acceleration $\partial\tilde{u}/\partial t$ during Deployment 9-1.

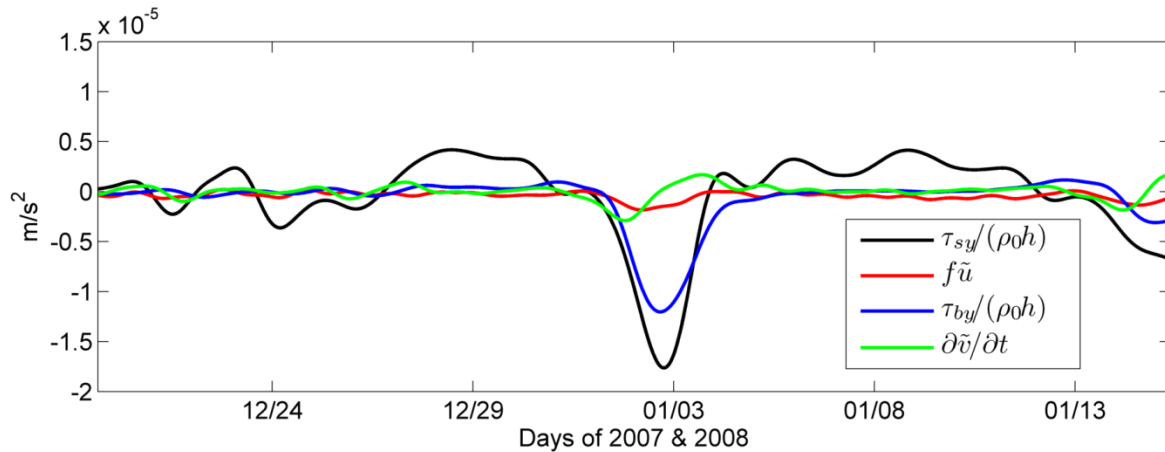


Figure 7-4. Time series of along-shelf momentum terms: wind stress $\tau_{sy}/\rho_0 h$ (black line), Coriolis acceleration $f\tilde{u}$ (red line), bottom stress $\tau_{by}/\rho_0 h$ and local acceleration $\partial\tilde{v}/\partial t$ during Deployment 7-1.

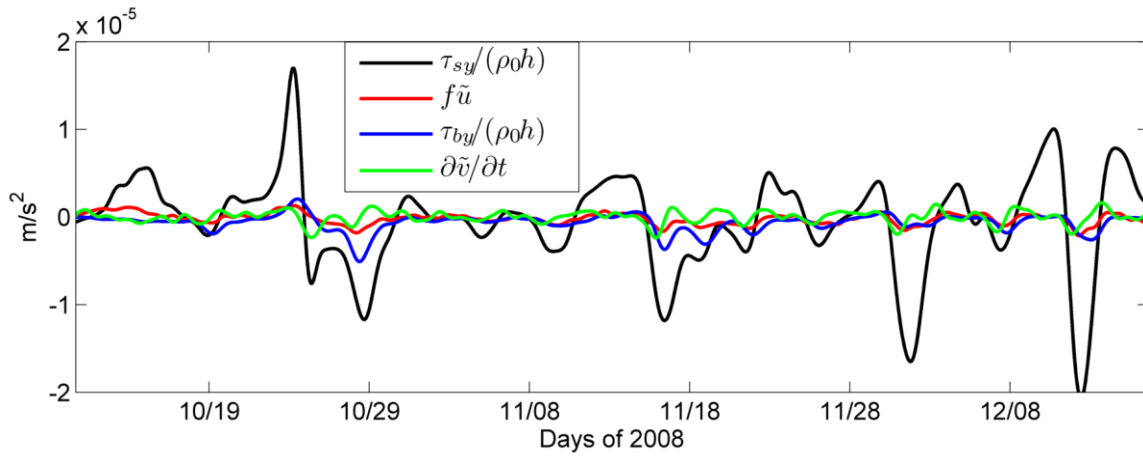


Figure 7-5. Time series of along-shelf momentum terms: wind stress $\tau_{sy}/\rho_0 h$ (black line), Coriolis acceleration $f\tilde{u}$ (red line), bottom stress $\tau_{by}/\rho_0 h$ and local acceleration $\partial\tilde{v}/\partial t$ during Deployment 8-1.

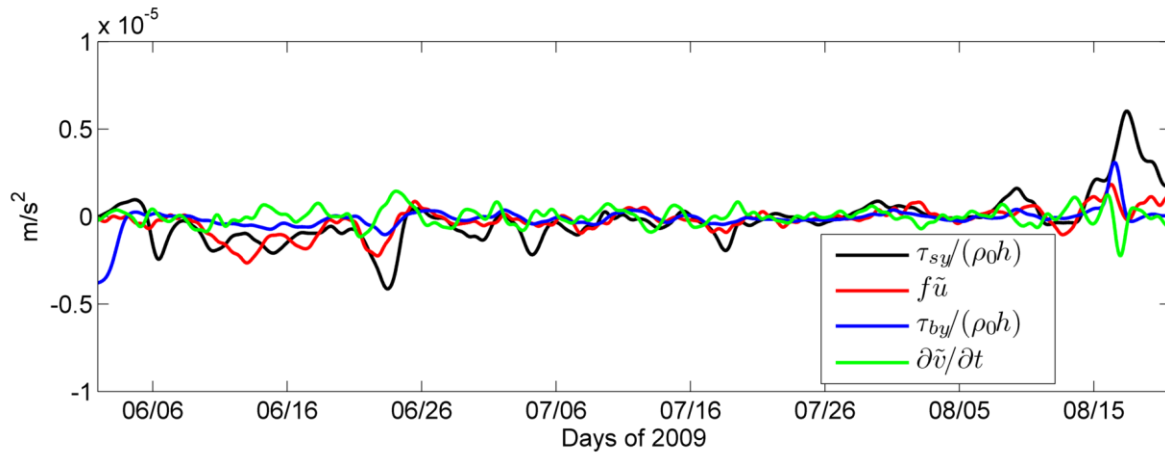


Figure 7-6. Time series of along-shelf momentum terms: wind stress $\tau_{sy}/\rho_0 h$ (black line), Coriolis acceleration $f\tilde{u}$ (red line), bottom stress $\tau_{by}/\rho_0 h$ and local acceleration $\partial\tilde{v}/\partial t$ during Deployment 9-1.

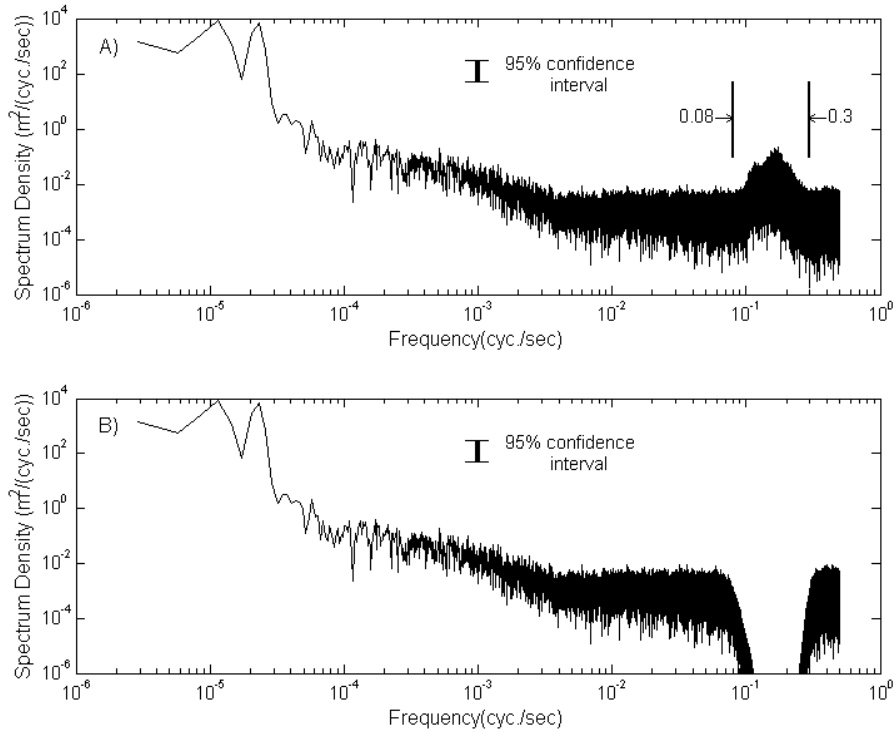


Figure 7-7. Spectrum density of water surface height (m) dealing A) without a band-stop filter B) with a band-stop filter.

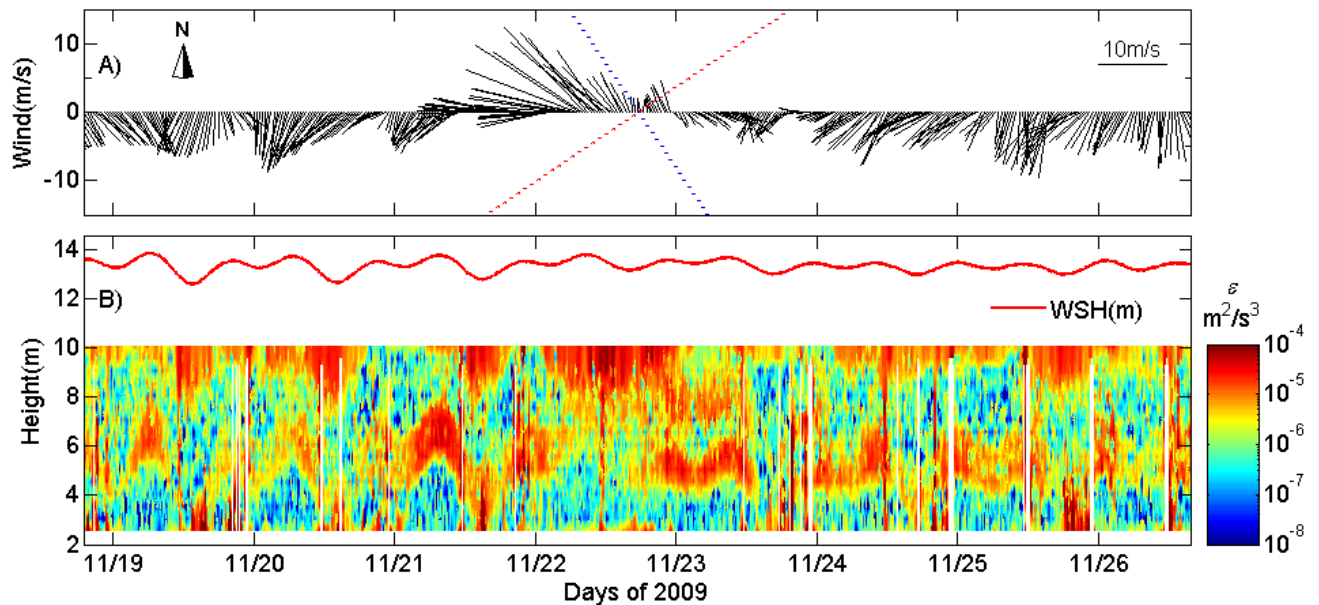


Figure 7-8. Time series of A) wind vector plots with the along- and cross-shelf direction denoted by blue and red dotted line, respectively and B) Turbulent Kinetic Energy Dissipation rate (ϵ , m^2/s^3) described by the contour and water surface height (m) described by red solid line during Deployment 9-5. The white gaps indicate unreliable estimates ($\epsilon > 2.0 \times 10^{-4}$).

CHAPTER 8 SUMMARY

Time series of current velocities taken in the shallow (<15m) nearshore region were used to study the dominant processes that drive inner shelf circulation over the West Florida Shelf. Spectral density analysis showed that tidal velocities at this study area were dominated by the M_2 harmonic and the diurnal harmonics. Semidiurnal tides of Deployment 7-1 and 9-1 indeed tended to be barotropic tides that are independent on depth. In contrast, diurnal vertical structure appeared to be influenced by the seasonally varying stratification. It was found the semidiurnal tides primarily propagate counter-clockwise by using Rotary Spectral Density.

Analysis of low-pass filtered data provides the interpretation of the shelf dynamics over the West Florida Inner Shelf. The subtidal currents were strongly polarized along-isobath. The vertical structure of along-shelf currents was primarily uniform with depth. The temporal variation of subtidal cross-shelf velocities over the inner shelf was relatively weak, compared to that of subtidal along-shelf velocities. Southerly and northerly winds tended to induce downwelling and upwelling, respectively. In case of weak mean low-pass filter winds (3.3 m/s during Deployment 9-1), currents in the surface and bottom layer were more directed to the right and left of wind direction, respectively. This agrees with theory that says that the thickness of the Ekman layer is mainly dependent on the strength of wind; Strictly speaking, the location of the inner shelf should vary in time because of changes in Ekman layer's depth.

Analyses of Empirical Orthogonal Functions (EOFs) were used to estimate the spatial and temporal variability of currents associated with winds. During Deployment 7-1 and 8-1 when the mean low-pass filtered wind speed was larger than 5.8 m/s, the first

modes of the cross-shelf currents reconstructed by EOF analyses primarily flowed in the same direction. In contrast, during Deployment 9-1, the first mode of the cross-shelf currents reconstructed by EOF analyses showed two-layer flows. There existed a net water transport to the right of the along-shelf wind direction in the upper layer and a return flow in the lower layer. The positive correlation coefficients (approximately 0.75 by CEOF and 0.77 by CHEOF) between mode 1 and along-shelf wind described the surface Ekman transport driven to the right of along-shelf wind. The negative correlation coefficients (approximately -0.6 by CEOF and -0.47 by CHEOF) between mode 1 and along-shelf wind were consistent with bottom Ekman transport driven to the left of along-shelf wind. The second modes of the cross-shelf currents reconstructed by EOF methods showed the exchange flows during Deployment 7-1, 8-1 and 9-1. The second modes of the cross-shelf currents reconstructed by EOF methods were best correlated with cross-shelf wind for all the deployments. The correlation coefficients in the upper layer and the lower layer were positive and negative, respectively. This shows that the second modes of cross-shelf currents had an element of downwind flow in the upper layer and upwind flow in the lower layer generated by cross-shelf wind.

Estimates of terms in the along-shelf and cross-shelf momentum balances give insight into the dynamics of subtidal currents over the inner shelf. In the cross-shelf budget, the dominant terms during Deployment 7-1 and 8-1 were the wind stress, followed by Coriolis acceleration. This implies that the wind-driven cross-shelf currents are a key component of shelf dynamics. However, the Coriolis acceleration during Deployment 9-1 was dominant, with the wind stress term playing a secondary role. The weak wind stress caused a net water transport to the right of the wind stress within a

thin surface Ekman layer and cross-shelf pressure gradient. The pressure gradient induced a bottom Ekman transport driven to the left of the geostrophic current because of the along-shelf bottom friction. As a result, the dominant terms in the cross-shelf budget are wind stress and Coriolis acceleration that are balanced by the cross-shelf pressure gradient term. The dominance of wind stress in the along-shelf momentum budget was shown in this study. The Coriolis, bottom stress and local acceleration have the same order of magnitude except for Deployment 7-1. The bottom stress of Deployment 7-1 was an order of magnitude bigger than the Coriolis and local acceleration.

Measurements of TKE dissipation rate in the ocean provide insights into understanding vertical exchange processes. Current velocity data from Deployment 9-5 were used to estimate the rate of dissipation. The turbulent fluxes in the middle of water column were likely associated with the two-layer flow. The unidirectional cross-shelf currents that were likely driven by strong winds (> 7 m/s) tended to break the turbulent fluxes. When wind stress was small (< 7 m/s), the intensified vertical shear associated with two-layer could generate small eddies that dissipated TKE in the interface between the bottom and surface boundary layer.

LIST OF REFERENCES

- Allen, J. S., 1980: Models of wind-driven currents on the continental shelf. *Annu. Rev. Fluid Mech.*, 12, 398-433.
- Barnett, T. P., 1983: Interaction of the monsoon and pacific trade wind system at interannual time scales. Part I: The equatorial case. *Mon. Wea. Rev.*, 111, 756-773.
- Brown, W. S., N. R. Pettigrew, and J. D. Irish, 1985: The Nantucket shoals flux experiment (NSFE79). Part II: The structure and variability of across-shelf pressure gradients, *J. Phys. Oceanogr.*, 15, 749-771.
- Brown, W. S., J. D. Irish, and C. D. Winant, 1987: A description of subtidal pressure field observations on the northern California continental shelf during the Coastal Ocean Dynamics Experiment, *J. Geophys. Res.*, 92, 1605-1636.
- Burchard, H., O. Petersen, and T. P. Rippeth, 1998: Comparing the performance of the Mellor-Yamada and the $k-\epsilon$ two-equation turbulence models, *J. Geophys. Res.*, 103, 10453-10554.
- Csanady, G. T., 1967: On the "Resistance Law" of a turbulent Ekman layer. *J. Atmos. Sci.*, 24, 467-471.
- Denbo, D. W., and J. S. Allen, 1984: Rotary empirical orthogonal function analysis of currents near the Oregon coast. *J. Phys. Oceanogr.*, 14, 35-46.
- Dever, E. P., 1997: Wind-forced cross-shelf circulation on the Northern California Shelf. *J. Phys. Oceanogr.*, 27, 1566-1580.
- Dudas, S. E., B. A. Grantham, A. R. Kirincich, B. A. Menge, J. Lubchenco, and J. A. Barth, 2009: Current reversals as determinants of intertidal recruitment on the central Oregon coast. *ICES. J. Mar. Sci.*, 66, 396-407.
- Edward, C. R., and H. E. Semi, 2008: Complex EOF analysis as a method to separate barotropic and baroclinic velocity structure in shallow water. *J. Atmos. Oceanic Technol.* 25, 808-821.
- Ekman, V. W., 1905: On the influence of the Earth's rotation on ocean-currents. *Arkiv Matematik, Astron. Fysik.*, 2, 1-53.
- Epifanio C. E., and R. W. Garvine, 2001: Larval transport on the Atlantic continental shelf of North America. A review. *Estuar. Coast. Shelf Sci.*, 52, 51-77.
- Falkowski, P. G., R.T. Barber, and V. Smetacek, 1998: Biogeochemical controls and feedbacks on ocean primary production. *Sci.*, 281, 200-206.

- Fewings, M. R., and S. J. Lentz, 2010: Momentum balances on the inner continental shelf at Martha's Vineyard Coastal Observatory. *J. Geophys. Res.* 115, C12023.
- Fukuoka, A., 1951: A study of 10-day Forecast (A synthetic Report), Vol. XXII. *The Geophysical Magazine: Tokyo.* 177-218.
- Gargett, A. E., 1999: Velcro measurement of turbulence kinetic energy dissipation rate epsilon, *J. Atmos. Oceanic Technol.*, 16(12), 1973-1993.
- Garland, E. D., C. A. Zimmer, and S. J. Lentz, 2002: Larval distributions in inner-shelf waters: the roles of wind-driven cross-shelf currents and diel vertical migrations. *Limnol. Oceanogr.*, 47, 803-817.
- Gilbes, F., C. Tomas, J. J. Walsh, and F. E. Muller-Karger, 1996: An episodic chlorophyll plume on the West Florida Shelf. *Cont. Shelf Res.*, 16 (9), 1201-1224.
- Gill, A. E., 1968: Similarity theory and geostrophic adjustment. *Quart. J. Roy. Meteor. Soc.*, 94, 581-585.
- Grantham, B. A., F. Chan, K. J. Nielsen, D. S. Fox, J. A., and J. A. Barth, 2004: Upwelling-driven nearshore hypoxia signals ecosystem and oceanographic changes in the northeast Pacific. *Nature*, 429, 749-754.
- Hannachi, A., I. T. Jolliffe, and D. B. Stephenson, 2007: Empirical orthogonal functions and related techniques in atmospheric science: A review. *Int. J. Climatol.* 27, 1119-1152.
- Hardy D. M., and J. J. Walton, 1978: Principal components analysis of vector wind measurements. *J. Appl. Meteor.*, 17, 1153-1162.
- He, R., and R. H. Weisberg, 2002: West Florida shelf circulation and temperature budget for the 1999 spring transition. *Cont. Shelf Res.*, 22, 719-748.
- He, R., and R. H. Weisberg, 2003: A Loop Current intrusion case study on the West Florida shelf. *J. Phys. Oceanogr.*, 33(2), 465-477.
- He, R., Y. Liu, and R. H. Weisberg, 2004: Coastal ocean wind fields gauged against the performance of an ocean circulation model. *Geophys. Res. Lett.*, 31, L14303.
- Horel, J. D., 1981: A rotated principal component analysis of the interannual variability of the Northern Hemisphere 500mb height field. *Mon. Wea. Rev.*, 109, 2080-2092.
- Huh, O. K., W. J. Wiseman, and L. J. Rouse, 1981: Intrusion of loop current waters onto the West Florida continental shelf. *J. Geophys. Res.*, 86(C5), 4186-4192.

- Kaihatu, J. M., R. A. Handler, G. O. Marmorino, and L. K. Shay, 1998: Empirical orthogonal function analysis of ocean surface currents using complex and real-vector method. *J. Atmos. Oceanic Technol.* 15, 927-941.
- Kajiura, K., 1958: Effect of Coriolis force on edge waves. (II) Specific examples of free and forced waves. *J. Mar. Res.*, 16, 145-157.
- Kirincich, A. R., and S. J. Lentz, 2009: Wave-driven inner-shelf motions on the Oregon Coast. *J. Phys. Oceanogr.*, 39, 2942-2956.
- Klinck, J. M., 1985: EOF analysis of central Drake Passage currents from DRAKE 79. *J. Phys. Oceanogr.* 15, 288-298.
- Koblinsky, C. J., 1981: The M_2 tide on the West Florida Shelf. *Deepsea Res.*, 28A, 1517-1532.
- Kundu, P. K., and J. S. Allen, 1976: Some three-dimensional characteristics of low-frequency current fluctuations near the Oregon coast. *J. Phys. Oceanogr.*, 6, 181-199.
- Kutzbach, J. E., 1967: Empirical eigenvectors of sea-level pressure, surface temperature and precipitation complexes over North America. *J. Appl. Meteor.*, 6, 791-802.
- Lee, T. N., W. J. Ho, V. Kourafalou, and J. D. Wang, 1984: Circulation on the continental shelf of the southeastern United States. Part I: subtidal response to wind and Gulf Stream forcing during winter. *J. Phys. Oceanogr.*, 14, 1001-1012.
- Lee, T. N., E. Williams, R. E. J. Wang, and L. Atkinson, 1989: Response of South Carolina continental shelf waters to wind and Gulf Stream forcing during winter of 1986. *J. Geophys. Res.*, 94, 10715-10754.
- Legler, D. M., 1983: Empirical orthogonal function analysis of wind vectors over the tropical Pacific region. *Bull. Amer. Meteor. Soc.*, 64, 234-241.
- Lentz, S. J., 1994: Current dynamics over the Northern California inner shelf. *J. Phys. Oceanogr.*, 24, 2461-2478.
- Lentz, S. J., 1995: Sensitivity of the inner-shelf circulation to the form of the eddy-viscosity profile. *J. Phys. Oceanogr.*, 25, 19-28.
- Lentz, S. J., and C. D. Winant, 1986: Subinertial currents on the southern California shelf. *J. Phys. Oceanogr.*, 16, 1737-1750.
- Lentz, S. J., R. T. Guza, S. Elgar, F. Feddersen, and T. H. C. Herbers, 1999: Momentum balances on the North Carolina inner shelf. *J. Geophys. Res.*, 104, 18205-18226.

- Lentz, S. J., 2001: The influence of stratification on the wind-driven cross-shelf circulation over the North Carolina shelf. *J. Phys. Oceanogr.*, 31, 2749-2760.
- Lentz, S. J., and M. R. Fewings, 2012: The wind- and wave-driven inner-shelf circulation. *Annu. Rev. Mar. Sci.*, 4, 317-343.
- Lhermitte, R., 1968: Turbulent air motion as observed by Doppler radar, paper presented at 13th Radar Meteorological Conference, Am. Meteorol. Soc., Montreal, Que., Canada. 498-503.
- Li, Z., and R. H. Weisberg, 1999a: West Florida Shelf response to upwelling favorable wind forcing: Kinematics. *J. Geophys. Res.*, 104, 13507-13527.
- Li, Z., and R. H. Weisberg, 1999b: West Florida Shelf response to upwelling favorable wind forcing 2. Dynamics. *J. Geophys. Res.*, 104, 23427-23442.
- Liu Y., and R. H. Weisberg, 2005: Momentum balance diagnoses for the West Florida Shelf. *Cont. Shelf Res.*, 25, 2054-2074.
- Liu Y., and R. H. Weisberg, 2012: Seasonal variability on the West Florida Shelf. *Progress in Oceanog.*, 104, 80-98.
- Lorenz, E. N., 1956: Empirical Orthogonal Functions and Statistical Weather Prediction. Technical report, Statistical Forecast Project Report 1, Dep. Of Meteor., MIT: 49.
- MacKinnon, J. A., and M. C. Gregg, 2003: Mixing on the late-summer New England shelf-solibores, shear, and stratification, *J. Phys. Oceanogr.*, 33, 1476-1492.
- Marmorino, G. O., 1983: Variability of current, temperature, and bottom pressure across the West Florida continental shelf, winter 1981-1982. *J. Geophys. Res.*, 88(C7), 4439-4457.
- Merrifield, M. A., and R. T. Guza, 1990: Detecting propagating signals with complex empirical orthogonal functions: a cautionary note. *J. Phys. Oceanogr.* 20 1628-1633.
- Mitchum, G. T., and W. Sturges, 1982: Wind-driven currents on the West Florida Shelf. *J. Phys. Oceanogr.* 12, 1310-1317.
- Molinari, R. L., S. Baig, D. W. Behringer, G. A. Maul, and R. Legeckis, 1977: Winter intrusions of the loop current. *Science*, 198, 505-506.
- Morey, S. L., P. J. Martin, J. J. O'Brien, A. A. Wallcraft, and J. Zavala-Hidalgo, 2003: Export pathways for river discharged fresh water in the northern Gulf of Mexico, *J. Geophys. Res.*, 108, 3303.
- Ng, B., 1993: The prediction of nearshore wind-induced surface currents from wind velocities measured at nearby land stations. *J. Phys. Oceanogr.*, 23, 1609-1617.

- Nittrouer C. A., and L. D. Wright, 1994: Transport of particles across continental shelves. *Rev. Geophys.*, 32, 85-113.
- Obukhov, A. M. 1947: Statistically homogeneous fields on a sphere. *Uspethi Matematicheskikh Nauk.* 2, 196-198.
- Pettigrew, N. R., 1981: The dynamics and kinematics of the coastal boundary layer off Long Island, Ph. D. thesis, Woods Hole Oceanographic Institution, Woods Hole, Massachusetts, 262 pp.
- Poon, Y. K., and O. S. Madsen, 1991: A two-layer wind-driven coastal circulation model. *J. Geophys. Res.*, 96, 2535-2548.
- Pope, S. B., 2000: *Turbulent flows*. Cambridge University Press, 771 pp.
- Prandle, D., and J. Matthews, 1990: The dynamics of nearshore surface currents generated by tides, wind and horizontal density currents. *Contin. Shelf Res.*, 10, 665-681.
- Preisendorfer R. W., 1988: *Principal component analysis in meteorology and oceanography*. Elsevier: Amsterdam.
- Reid, R. O., and R. E. Whitaker, 1981: Numerical model for astronomical tides in the Gulf of Mexico. Texas A&M Rep. for U.S. Army Engineers Waterway Experiment Station, 115 pp.
- Richman, M. B., 1986: Rotation of principal components. *J. Climatol.*, 6, 293-335.
- Sauvageot, H., 1992: *Radar Meteorology*. Artech House, Norwood, Mass. 384 pp.
- Sharples, J., C. M. Moore, and E. R. Abraham, 2001: Internal tide dissipation, mixing, and vertical nitrate flux at the shelf edge of NE New Zealand, *J. Geophys. Res.*, 106(C7), 14069-14081.
- Simpson, J. H., W. R. Crawford, T. P. Rippeth, A. R. Campbell, and J. V. S. Cheok, 1996: The vertical structure of turbulent dissipation in shelf seas, *J. Phys. Oceanogr.*, 26, 1579-1590.
- Thompson, K. R., and D. T. Pugh, 1986: The subtidal behavior of the Celtic Sea—II Currents. *Contin. Shelf Res.*, 5, 321-346.
- Tilburg, C. E. 2003: Across-shelf transport on a continental shelf: Do across-shelf winds matter? *J. Phys. Oceanogr.*, 33, 2675-2688.
- von Storch, H., and F. W. Zwiers, 2003: *Statistical analysis in climate research*. Cambridge University Press. 484pp.

- Wallace, J. M., 1972: Empirical orthogonal representation of time series in the frequency domain. Part II: Application to the study of tropical wave disturbances. *J. Appl. Meteor.*, 11, 893-900.
- Weisberg, R. H., B. D. Black, and H. Yang, 1996: Seasonal modulation of the West Florida continental shelf circulation. *Geophys. Res. Lett.*, 23, 2247-2250.
- Weisberg, R. H., Z. Li, and F. E. Muller-Karger, 2001: West Florida shelf response to local wind forcing: April 1998. *J. Geophys. Res.*, 106, 31239-31262.
- Weisberg, R. H., R. He, Y. Liu, and J. I. Virmani, 2005: West Florida Shelf Circulation on Synoptic, Seasonal, and Interannual Time Scales. *Geophys. Monograph Series*. 161, 325-347.
- Wiles, P. J., T. P. Rippeth, J. H. Simpson, and P. J. Hendicks, 2006: A novel technique for measuring the rate of turbulent dissipation in the marine environment. *Geophys. Res. Lett.*, 33, L21608.

BIOGRAPHICAL SKETCH

Sangdon So was born and raised in Jeonbuk, South Korea, with views of Baekdudaegan. He received his B.A. in civil engineering from Chonbuk National University in 2001. He married Jin Kim in January 2003, whom he has always loved. The couple has one daughter, River; and one son, Jungseob. He decided to take up graduate study and obtained M.S. in the Department of Civil and Coastal Engineering at the University of Florida in 2009. The pursuit of knowledge made him continue PhD study. In August 2013, Sangdon was honored to receive his doctorate degree from the Department of Civil and Coastal Engineering at the University of Florida.